Techniques for Strength Measurement at High Pressures and Strain-Rates Using Transverse Waves

Thesis by

Victoria Stolyar Richmond

In Partial Fulfillment of the Requirements

for the Degree of

Doctor of Philosophy

California Institute of Technology

Pasadena, California

2014

(Defended December 9, 2013)

"To the discovery of the universe and the inspiration to never stop searching for the answers."

Acknowledgments

First off, thank you to all of the funding resources that I have received throughout the last few years. My graduate fellowship from the Keck Institute for Space Studies that I received my first year at Caltech is sincerely appreciated as it allowed me to pursue my Masters degree. For my remaining years at Caltech, the Predictive Science Academic Alliance Program through the Department of Energy National Nuclear Security Administration gave me the opportunity to pursue this research.

I must express my gratitude to my advisor, Professor Guruswami Ravichandran. Thank you for your support to not only myself, but to many of the students on campus. Your words of encouragement and mentorship have been much appreciated and I thank you for providing a community for our group members to feel a part of.

To my thesis committee, thank you all so much for taking the time out of your busy schedules to attend my candidacy exam, as well as this defense. Professor Meiron, thank you for such a great Fluids class my first year, I appreciate all of the notes you provided for our class, it definitely helped me understand and organize all of the information we learned our first year. Professor Bhattacharya, thank you for all of your advice and wisdom during group meetings and for the opportunity to TA Solid Mechanics for you. Professor Kochmann, I very much enjoyed Continuum Mechanics, thank you for presenting the information in such a clear and accessible manner.

To my lab group, thank you to all group members past and present. Specifically, Kristen John, thank you for all of the supportive conversations, and for being such a great friend throughout the years. Mike, I am indebted to you for all of your help with experiments, I sincerely appreciate it. I must give thanks to Cheryl Gause for not only helping me order things for the lab, but mostly thank you for being a true friend and for always being so kind.

To all of the GALCIT people, thank you for all that you have done, especially Dimity Nelson and Christine Ramirez. Without your hard work, our department would not function. Thank you to the Aero Shop: Joe Haggerty, Brad St. John, and Ali Kiani. You have always been very kind and have helped even at short notice, I really value that.

To my first year Aero group, words cannot express how lucky I feel to have had such a great community of people to overcome such a challenging year. Kristen John, Andy Galvin, Stephanie Coronel, Jomela Meng, Siddhartha Verma, Jocelyn Escourrou, Ignacio Maqueda, Landry Fokoua Djodom, Adrian Sanchez Menguaiano, Philipp Oettershagen, Namiko Saito, Juan Pedro Mendez Ganado, Brad Lyon, and Xin Ning. You all are an inspirational and talented group of people that I feel privileged to have worked with.

To all of the people at Sandia National Laboratories who made my internship possible, I thank you immeasurably for giving me this incredible opportunity. Thank you especially to Dawn Flicker for making me feel welcome in your group. Thank you to Scott Alexander for being an incredible mentor both during my internship and throughout the remainder of my research. Your expertise has been greatly appreciated. Thank you to Seth Root for mentoring me as well and taking the time to discuss novel concepts with me. To all of the amazing people I had the opportunity to work with, I give a huge thanks - Dan Dolan, Justin Brown, Tom Ao, Nicole Cofer, Aaron Bowers, Randy Hickman, Andy Shay, Jesse Lynch, Gordon Leifeste, Tom Thornhill, Bill Reinhart, John Martinez, Keith Hodge, Rocky Palomino, Heidi Anderson, and Laveryn Apodaca. You all incorporated me into your group and went out of your way to help my experiments come to life. Thank you also to Trish St. John, for organizing the intern program and for your friendship in a new place.

To everyone who has taken the time to discuss my research with me and help me get through some of the roadblocks, thank you so much. Especially thank you to Dr. Rodney Clifton and Dr. Lalit Chhabildas. I am so honored to have worked with two of the leading experts in the field. Thank you also to Dr. Andy Richards and Dr. Mike Mello for your conversations and advice.

To the Caltech community, thank you for all of the exciting adventures these last few years. Thank you to Felicia Hunt for your support and guidance and to the Graduate Student Council for giving me the opportunity to work in such a great community. To the Caltech Health Center, especially Alice Sogomonian, Divina Bautista, and Linda Schutz, thank you for having hearts of gold. Through all of the stressful times at Caltech, you provide such care for all of the community and have been absolutely wonderful and kind to me. I am so touched that you take the time to remember everyone's name and really get to know the students.

To all of my friends both at Caltech and elsewhere, thank you for all of the words of advice, the reassurances, and the great times these last few years. Dominic Rizzo, Melissa Tanner, Elan Borenstein, Melda Buyukozturk, Kristen John, Sara Drakeley, and Anya Shafiro; you have all been there for me in one way or another, and I thank you for that. To anyone I may have missed, please

know that your support and friendship has been very much appreciated as well.

To my family, I cant begin to thank you for all of your support and sacrifices throughout the years. Mom and Dad, you have been incredible and loving parents. Thank you for always encouraging me to do my best and for believing in me. Zoya, thank you for being the best sister anyone could ask for. You are truly one of the kindest people that I know. Uncle Semion, thank you for advising me to pursue my Ph.D. Rob and Carol, I could not have asked for better in-laws. Thank you for welcoming me in Albuquerque and for your support. Finally, thank you to my husband John Richmond for supporting me in all aspects of life. You challenge me to never give up and to never stop dreaming. For that I am beyond thankful.

Abstract

The study of the strength of a material is relevant to a variety of applications including automobile collisions, armor penetration and inertial confinement fusion. Although dynamic behavior of materials at high pressures and strain-rates has been studied extensively using plate impact experiments, the results provide measurements in one direction only. Material behavior that is dependent on strength is unaccounted for. The research in this study proposes two novel configurations to mitigate this problem.

The first configuration introduced is the oblique wedge experiment, which is comprised of a driver material, an angled target of interest and a backing material used to measure in-situ velocities. Upon impact, a shock wave is generated in the driver material. As the shock encounters the angled target, it is reflected back into the driver and transmitted into the target. Due to the angle of obliquity of the incident wave, a transverse wave is generated that allows the target to be subjected to shear while being compressed by the initial longitudinal shock such that the material does not slip. Using numerical simulations, this study shows that a variety of oblique wedge configurations can be used to study the shear response of materials and this can be extended to strength measurement as well. Experiments were performed on an oblique wedge setup with a copper impactor, polymethylmethacrylate driver, aluminum 6061-t6 target, and a lithium fluoride window. Particle velocities were measured using laser interferometry and results agree well with the simulations.

The second novel configuration is the y-cut quartz sandwich design, which uses the anisotropic properties of y-cut quartz to generate a shear wave that is transmitted into a thin sample. By using an anvil material to back the thin sample, particle velocities measured at the rear surface of the backing plate can be implemented to calculate the shear stress in the material and subsequently the strength. Numerical simulations were conducted to show that this configuration has the ability to measure the strength for a variety of materials.

Table of Contents

List of Figures

List of Tables

Chapter 1

Introduction

The dynamic behavior of materials at high pressures and strain-rates has been studied for many years using wave propagation techniques through solids [49], [25], [71], [69]. Although results for the planar compression of materials are prevalent, the full material response needs further investigation as the methods involved to obtain these measurements can be quite complicated.

1.1 Motivation

One method to estimate the three dimensional response of a material is to assume a constitutive relation for it and fit the data in an iterative manner [43]. By assuming a model from normal impact data, however, only the longitudinal response is really seen [19], which is insufficient for material behavior that depends on the strength after the material yields. For this reason, testing must be performed to characterize the two extra dimensions and accurately account for the strength of the material.

The strength of a material is its response to deviatoric stresses [3]. In high-speed machining, a variety of techniques are used to shape materials; some of these methods, such as metal cutting, result in the material withstanding strain-rates of up to 10^5/s [44] and thus it is important to determine how the material will behave and how much it can withstand before it fails. Similarly, in automobile collisions, materials can experience strain-rates of up to 10^3/s [27]. Understanding how the material responds in this scenario is crucial to vehicle safety. Strength analysis at high strain-rates is important in the battlefield as well in the penetration of different types of armor materials where the study of material response can also be used to save lives [76]. At even higher strain-rates, inertial confinement fusion can also benefit from this analysis. Here, a fuel target containing a mixture of deuterium and tritium is heated and compressed by a laser with the desired

result of creating vast amounts of energy. Presently, ripples form due to inhomogeneities in the targets that are thought to be related to strength. Understanding this behavior would shed light on this experimental technique, the results of which could benefit society [38]. Finally, in the case of planetary impact, experiments probing strength response can be used to understand how these large bodies behave in such extreme conditions. The results of these analyses could be used to understand this dynamic event and would elucidate events such as the formation of Earth's moon and other such collisions.

1.2 Previous Methods

A variety of systems have been implemented to study high strain-rate ($> 10^2$)/s effects of materials. One such experiment is the Kolsky bar, which tests specimens with compression, torsion, or tension at strain-rates on the order of $10^2 - 10^3$/s. The specimen is placed between two long bars that remain elastic throughout the experiment and one of the bars is impacted to transmit a pulse, which is reverberated in the sample. Upon reflection, part of the wave travels back into the bar that was hit, and the rest is transmitted into the second bar. Strain gauges measure the response in both bars to the incident, reflected, and transmitted waves from which the response of the specimen can be calculated [65], [4]. Another method of studying high strain-rate phenomenon is the Taylor impact test, which looks at strain-rates of $10^3 - 10^4$/s. This experiment consists of impacting a large target with a cylindrical rod flyer and measuring how the shape of the target is changed in order to find the dynamic yield stress of the material [33], [72]. A technique used for higher strain-rates of order $10^4 - 10^7$/s is the oblique gun. This setup uses inclined plates to generate shear and is particularly effective in studying higher strain-rate phenomenon, the focus of this study. Figure 1.1 shows the various methods discussed to study strength and the applications that the results are used to understand.

The basic premise of the oblique gun is that two plates are set parallel to one another, but at an angle with respect to the horizontal. Upon impact, one dimensional plane longitudinal and shear waves form due to the impact velocity vector being oriented at an angle with respect to the target. If no slip occurs between the target and impactor, particle velocity at the impact face is independent of the position along it and one-dimensional wave theory can be used to describe the state of the material since motion is only dependent on the distance normal to the impact face and time [2], [21], [53], [76]. With the generation of both types of waves, the material is compressed and hence slip is prevented such that shear can be transmitted into it. A schematic of this experimental setup

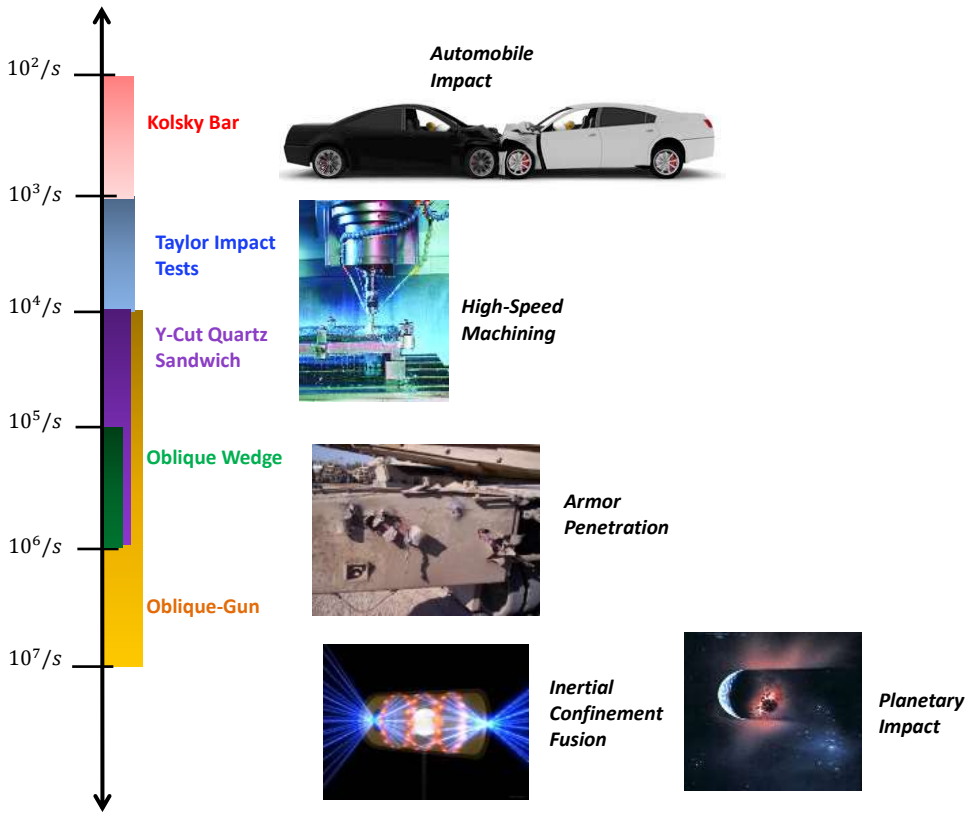

Figure 1.1: Techniques used to study shear response of materials at high strain-rates with applications that the results are used to understand.

is shown with a detailed description in Section 4.2.

A clever method that uses a normal impact experimental setup implements the anisotropic nature of y-cut quartz. Upon impact, y-cut quartz generates two types of waves (described in Chapter 4) that each contain longitudinal and shear components of velocity [48], [47], [1], [18]. These waves can be used in a manner analogous to the oblique gun to subject a target to a simultaneous pressure and shear environment and was studied by Chhabildas and Swegle in a variety of publications [75], [19], [16]. It was found that a specimen could be bonded to the y-cut quartz by using an epoxy-particulate mixture that allowed for the transmittance of shear to the specimen. In these studies, the maximum shear transmitted was observed to be 0.35 GPa and the experiment was limited in either the shear strength of the epoxy or the slippage of the target from the y-cut quartz.

Measuring transverse velocities poses complexities that are not present in normal impact experiments. To measure the velocities, laser interferometry techniques are used. These are described in detail in Section 5.2, but the basic premise is that laser light is shined onto a moving target and the reflected light is collected and combined with itself after it is Doppler shifted due to the movement

of the target. The combined light creates a beat frequency that is related to the velocity of the target. To implement this method for transverse velocities, fiber optic probes must be placed at an angle with respect to the normal at the back of the target and secured in place to collect light reflected off of the moving surface, see Section 5.2.1.2. To actually be able to collect light in these probes, the surface must be treated in a way that diffracts light shined onto it. Multiple studies have placed these techniques into practice where they have used either a diffraction grating that was deposited using photoresist techniques or a mirror surface that was scratched slightly to create a similar effect. The light that was diffracted off of this surface was collected by a variety of methods as well. One technique implemented a three probe configuration where a central probe was used to send light to the target that was then collected by the same probe and two side probes [52], [17], [32]. A similar approach has previously been taken with measurements using a window [31], [34], but these methods are relatively new and are even more complicated to use. This dissertation will describe the implementation of both methods to measure transverse velocities.

1.3 Thesis Outline

The premise of this research is to implement the normal impact gun setup, a system that is more readily available, with a variety of targets to measure the response of materials to shear at high strain-rates. The first configuration proposed utilizes oblique targets to generate shear waves while the second setup uses y-cut quartz to transmit shear, much like the work by Chhabildas and Swegle described above, but with a sandwich configuration where the target is a thin sample placed between two high-strength materials. This method is adapted from the oblique gun experiments described above and uses a thin sample in order to sustain a high strain-rate for a longer period of time than that experienced by a sample that is bonded to the y-cut quartz with no backing material. Two configurations using the y-cut quartz as a generator are described and by using the thin sample sandwiched between other materials, this study aims to expand upon the work done by Chhabildas and Swegle. Furthermore, although both the oblique wedge and y-cut quartz sandwich techniques currently reach the 10^6/s strain-rate range, there are possiblities to extend to higher strain-rates.

The first main chapter, Chapter 2, introduces the theories behind elastic wave propagation in solids and discusses the governing equations of plane waves that result from the conservation equations and the definitions of tractions, displacements, and strains. A progression is made into the equations describing the incidence of an oblique wave at an interface. Here, the incident angle and change in particle velocity across the wave can be used along with continuity of tractions

and velocities at the interface to describe the change in stresses and velocities across each set of longitudinal and shear waves that reflect from and transmit across the interface. The simple case of 1D wave propagation is discussed, which would result from a normal impact, where the 1D strain assumption can be used. The transition between elasticity to plasticity is analyzed and the yield stress is defined. As the velocity of the incident wave increases during an impact with increasing pressure, a shock front forms for which the Rankine-Hugoniot jump relations of mass, momentum and energy are given. The shock Hugoniot is also described — this is a set of states that the material can reach after it is shocked. Impedance matching is discussed to allow for the determination of particle velocity after the impact of two materials using their shock velocity vs. particle velocity Hugoniot. This analysis is used in shock polar analysis, which studies the incidence of an oblique shock wave on an interface and is used to determine the properties of the transmitted oblique wave in the material of interest.

Chapter 3 discusses the oblique wedge configuration, the first novel technique described. This configuration consists of a driver material and an oblique target of interest with a window at the rear surface and uses the theories in shock polar analysis to find the properties across the transmitted shock wave in the target. A variety of parameters in this experimental setup are studied in order to find the relationship between longitudinal stress in the target, the angle of obliquity of the incident wave, the transmitted shear wave angle, and the transmitted shock wave angle. Next, the target design is discussed to determine the dimensions of the entire target needed to measure the shear response. An elastic analysis is used along with a more refined hydrocode numerical simulation to predict the response of the setup. The latter simulations are used to analyze the nature of the shear wave in the target, to observe the strain-rate, and to calculate the shear stress based on the particle velocities that would be measured at the rear surface of the specimen in a given experiment. Comparisons are made between the calculated stresses, the stresses found in the simulation, and the yield stress of the material and calculations are performed using the Von Mises yield criteria to determine if the material is yielding. The path of the shear stress in a two dimensional yield surface is also analyzed to determine the mechanism of yielding and to investigate the viability of this technique in finding the yield strength of a material. The constraint of the impact velocity is discussed along with using a window to make in-situ measurements. The alternative use of an anvil in place of the window is then deliberated.

Chapter 4 introduces the y-cut quartz sandwich configuration, a novel technique that makes use of the anisotropy of y-cut quartz to generate shear waves. The oblique gun (or slotted barrel gun)

is discussed in further detail and the governing equations, used to find the longitudinal and shear stresses as well as the strain-rate, are given. The first of the sandwich configurations is introduced, where the y-cut quartz is used to drive a transverse and longitudinal wave into a high-strength material that is followed by a thin sample and a subsequent anvil backing material. Simulations are performed using a one-dimensional numerical analysis program and the results of these are used to find the dimensions of materials needed to measure the longest shear response possible within a given set of constraints. The assumption of a 1D strain with a superimposed shear is then checked using the stress tensor found in the simulation and analyses are made to ensure that the first driver and backing materials remain elastic, an integral part of the experiment, as will be described. The stress path is shown for this configuration to prove its ability to measure strength of a material, which is found using the rear surface velocity measurement. The measurement of strain-rate is discussed as well. The next configuration explored is the one driver y-cut quartz sandwich design, where the y-cut quartz is used as the elastic driver and the second high-strength material is eliminated, leaving the y-cut quartz followed by the sample and the anvil backing. Once again, simulations are performed to find appropriate measurements for the target setup and an analysis is conducted to make sure that the elastic assumption in the driver and backing as well as the 1D strain and superimposed shear are maintained throughout the experiment. The stress path is then discussed along with the shear stress and strength calculations. The strain-rate is also analyzed. Finally, the limitations of these two techniques are debated.

The loading systems and diagnostics used in the experiments for this dissertation are explored in Chapter 5. Powder guns at Caltech as well as Sandia National Laboratories are introduced along with the gas gun at the latter facility. The interferometry techniques used to measure the velocities are considered next. Here, the basic theories of the VISAR system are investigated and the angled measurements needed for the transverse velocities are explained. Another diagnostic called the PDV that is similar in purpose to the VISAR is also discussed. Some preliminary analysis is then made in the techniques needed to diffract light off the rear surface of the target.

In Chapter 6, two types of experiments are examined. The first is the y-cut quartz validation experiment conducted at Sandia National Laboratories using y-cut quartz and a lithium fluoride window. This experiment was used to validate the ability to measure transverse particle velocities through a window by comparing the results of the experiment with well-known simulations that implement the analysis of the anisotropic quartz material described by Johnson [47]. In this section, the crucial alignment of the off-axis probes and the measurement of their angles is inspected. Once

the technique is shown to work, it is implemented on a set of oblique wedge experiments, the results of which are compared to two dimensional simulations using a numerical code that accounts for strength. The complicated target setup for the oblique wedge is examined as well.

The final chapter summarizes the results found throughout this study. It then proposes future work that must still be performed and discusses the variety of directions this research can take.

Chapter 2

Theoretical Background

2.1 Elastic Wave Theory

2.1.1 Governing Equations

In order to understand what occurs in the oblique wedge and y-cut quartz sandwich experiments, it is important to study the propagation of waves through soild materials. Upon impact for both types of configurations, waves are generated and their travel through the specimens subjects these materials to different loading conditions. To begin analyzing waves, one must define the two types of reference frames. The first frame, called the "Lagrangian" or "Material" frame, follows a particular particle through a given flow while the second frame, called the "Eulerian" or "Spatial" frame, follows the total flow through a specific region. [63]. Figure 2.1 illustrates this concept. In this figure, ϕ is some property of the flow dependent on position, x, and time, t. To relate the two frames, the material derivative can be used, written as

$$\left(\frac{D\phi}{Dt}\right)_L = \left(\frac{\partial\phi}{\partial t}\right)_E + \underline{u}\cdot\nabla\phi = \frac{\partial\phi}{\partial t} + u_1\frac{\partial\phi}{\partial x} + u_2\frac{\partial\phi}{\partial y} + u_3\frac{\partial\phi}{\partial z}. \tag{2.1.1}$$

In this equation, the term on the left hand side represents the derivative of the flow property with respect to the Lagrangian frame, which is written on the right hand side in terms of the Eulerian derivative and the terms relying on the position in space of the particle.

For small deformations, the balance laws can be defined using the small strain formulation, which indicates that the description of the flow of material in both frames is approximately the same. This approximation allows for the determination of the governing equations for plane waves propagating in a material. Assume for a given body B, with some displacement field $\underline{u}\,(\underline{x},t)$, contact force, $\underline{t}\,(\underline{\hat{n}},\underline{x},t)$, and body force, $\underline{f}\,(\underline{x},t)$, for any point of B, linear momentum must be conserved [41]:

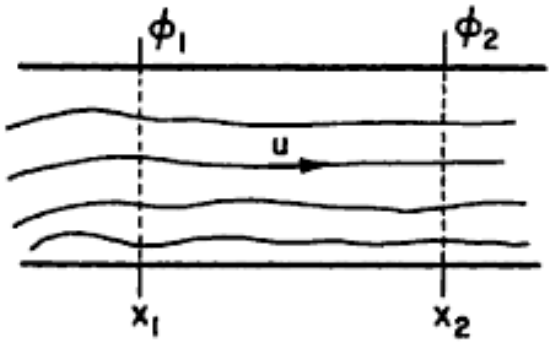

Figure 2.1: Definition of Eulerian and Lagrangian referentials (Courtesy Marc A. Meyers, [63])

$$\frac{d}{dt}\int_B \rho \underline{\dot{u}} dV = \int_{\delta B} \underline{t} dS + \int_B \underline{f} dV, \tag{2.1.2}$$

where an underlined variable represents a vector. The contact force in the above equation can be defined in terms of the Cauchy stress tensor — represented in bold — multiplied by the surface normal unit vector, denoted with a hat over it:

$$\underline{t}\left(\hat{\underline{n}}, \underline{x}, t\right) = \boldsymbol{\sigma}\left(\underline{x}, t\right) \hat{\underline{n}}. \tag{2.1.3}$$

Plugging this definition of traction into 2.1.2 above results in

$$\frac{d}{dt}\int_B \rho \underline{\dot{u}} dV = \int_{\delta B} \boldsymbol{\sigma}\left(\underline{x}, t\right) \hat{\underline{n}} dS + \int_B \underline{f} dV. \tag{2.1.4}$$

To simplify this equation, the first term needs to be examined using the Reynold's Transport Theorem [57]. This theorem reduces the first term on the left hand side to

$$\frac{d}{dt}\int_B \rho \underline{\dot{u}} dV = \int_B \frac{\partial}{\partial t}\left(\rho \underline{\dot{u}}\right) dV + \int_{\delta B} \rho \underline{\dot{u}}\left(\underline{\dot{u}} \cdot \hat{\underline{n}}\right) dS. \tag{2.1.5}$$

Applying the Divergence Theorem to the right hand side of Equation 2.1.5 results in

$$\frac{d}{dt}\int_B \rho \underline{\dot{u}} dV = \int_B \left(\dot{\rho} \underline{\dot{u}} + \rho \underline{\ddot{u}} + \rho \underline{\dot{u}} \mathrm{div}\left(\underline{\dot{u}}\right)\right) dV. \tag{2.1.6}$$

The right hand side of Equation 2.1.6 can be reduced using mass conservation, which states that

$$\frac{d}{dt}\int_B \rho dV = 0. \tag{2.1.7}$$

Equation 2.1.7 can also be re-written using the Reynold's Transport Theorem as

$$\frac{d}{dt}\int_B \rho dV = \int_B \left(\frac{\partial \rho}{\partial t} + \rho \text{div}\left(\underline{\dot{u}}\right)\right) dV = 0. \tag{2.1.8}$$

From Equation 2.1.8, it can be concluded that

$$\dot{\rho} = -\rho \text{div}\left(\underline{\dot{u}}\right). \tag{2.1.9}$$

This result can then be used to eliminate two of the terms in the right hand side of Equation 2.1.6, reducing the conservation of linear momentum equation, 2.1.4, to

$$\int_B \rho \underline{\ddot{u}} dV = \int_B \text{div}\left(\boldsymbol{\sigma}\right) dV + \int_B \underline{f} dV. \tag{2.1.10}$$

Reducing Equation 2.1.10, the local form of the conservation of momentum becomes

$$\rho \underline{\ddot{u}} = \text{div}\left(\boldsymbol{\sigma}\right) + \underline{f}. \tag{2.1.11}$$

The local form of the conservation of momentum equation can further be simplified by relating the Cauchy stress to strain such that eventually the expression obtained can be used to understand the displacements seen in plane wave propagation. For this simplification, the material is assumed to be linear elastic with the constitutive relation

$$\sigma_{ij} = C_{ijkl}\epsilon_{kl}, \tag{2.1.12a}$$

which can also be written as

$$\epsilon_{ij} = S_{ijkl}\sigma_{kl}, \tag{2.1.12b}$$

where ϵ_{kl} is the infinitesimal strain tensor, C_{ijkl} is the stiffness coefficient matrix, and S_{ijkl} is the compliance matrix. Here the stress tensor is now introduced using indicial notation. Compatibility between the strains and displacements states that

$$\epsilon_{kl} = \frac{1}{2}\left(u_{k,l} + u_{l,k}\right). \tag{2.1.13}$$

Substituting this into Equation 2.1.12a results in

$$\sigma_{ij} = \frac{1}{2} C_{ijkl}\left(u_{k,l} + u_{l,k}\right). \tag{2.1.14}$$

Assuming there is no body force, Equation 2.1.11 becomes the general equations of motion

$$\rho \frac{\partial^2 u_i}{\partial t^2} = \sigma_{ij,j}. \tag{2.1.15}$$

Substituting 2.1.14 into 2.1.15 results in the displacement formulation

$$\sigma_{ij,j} = \frac{1}{2} C_{ijkl} \left(u_{k,lj} + u_{l,kj} \right) = \rho u_{i,tt}. \tag{2.1.16}$$

The displacements can be defined in terms of velocities, where

$$u_{i,t} = v_i. \tag{2.1.17}$$

Then, substituting this expression into 2.1.16, results in the particle velocity formulation [22]:

$$\rho u_{i,tt} = \frac{1}{2} C_{ijkl} \left(u_{k,lj} + u_{l,kj} \right) = \rho v_{i,t} = \sigma_{ij,j}. \tag{2.1.18}$$

Equation 2.1.12b can also be written in terms of the stress and particle velocity formulation by first differentiating Equation 2.1.13, substituting indices i and j for k and l, and utilizing Equation 2.1.17 to get:

$$\epsilon_{ij,t} = \frac{1}{2} \left(v_{i,j} + v_{j,i} \right). \tag{2.1.19}$$

Then, differentiating Equation 2.1.12b and using the result of Equation 2.1.19:

$$S_{ijkl} \sigma_{kl,t} = \frac{1}{2} \left(v_{i,j} + v_{j,i} \right). \tag{2.1.20}$$

The matrix notation of the Cauchy stress and strain tensors in Equations 2.1.18 and 2.1.20 can be expressed as a first order system by first simplifying these tensors in terms of vector components using the Voigt notation. This substitution will make further analysis simpler.

$$\boldsymbol{\sigma} = \begin{bmatrix} \sigma_1 & \sigma_6 & \sigma_5 \\ \sigma_6 & \sigma_2 & \sigma_4 \\ \sigma_5 & \sigma_4 & \sigma_3 \end{bmatrix} \rightarrow \underline{\sigma} = \begin{bmatrix} \sigma_1 \\ \sigma_2 \\ \sigma_3 \\ \sigma_4 \\ \sigma_5 \\ \sigma_6 \end{bmatrix} \tag{2.1.21a}$$

$$\boldsymbol{\epsilon} = \begin{bmatrix} \epsilon_1 & \frac{1}{2}\epsilon_6 & \frac{1}{2}\epsilon_5 \\ \frac{1}{2}\epsilon_6 & \epsilon_2 & \frac{1}{2}\epsilon_4 \\ \frac{1}{2}\epsilon_5 & \frac{1}{2}\epsilon_4 & \epsilon_3 \end{bmatrix} \rightarrow \underline{\epsilon} = \begin{bmatrix} \epsilon_1 \\ \epsilon_2 \\ \epsilon_3 \\ \epsilon_4 \\ \epsilon_5 \\ \epsilon_6 \end{bmatrix}. \tag{2.1.21b}$$

Now with these vectors, Equations 2.1.18 and 2.1.20 can be written as 1st order systems

$$\rho \underline{v_t} + \mathbf{B_1}\underline{\sigma_{x1}} + \mathbf{B_2}\underline{\sigma_{x2}} + \mathbf{B_3}\underline{\sigma_{x3}} = 0 \tag{2.1.22a}$$

and

$$\mathbf{S}\underline{\sigma_t} + \mathbf{B_1^T}\underline{v_{x1}} + \mathbf{B_2^T}\underline{v_{x2}} + \mathbf{B_3^T}\underline{v_{x3}} = 0, \tag{2.1.22b}$$

where

$$\mathbf{B_1} = \begin{bmatrix} -1 & 0 & 0 & 0 & 0 & 0 \\ 0 & 0 & 0 & 0 & 0 & -1 \\ 0 & 0 & 0 & 0 & -1 & 0 \end{bmatrix}, \mathbf{B_2} = \begin{bmatrix} 0 & 0 & 0 & 0 & 0 & -1 \\ 0 & -1 & 0 & 0 & 0 & 0 \\ 0 & 0 & 0 & -1 & 0 & 0 \end{bmatrix}, \mathbf{B_3} = \begin{bmatrix} 0 & 0 & 0 & 0 & -1 & 0 \\ 0 & 0 & 0 & -1 & 0 & 0 \\ 0 & 0 & -1 & 0 & 0 & 0 \end{bmatrix}, \tag{2.1.23}$$

and the subscripts on the vectors in 2.1.22a and 2.1.22b denote differentiation with respect to the variable in the subscript. Another way to write these two equations is

$$\mathbf{A^t}\underline{\omega_t} + \mathbf{A^1}\underline{\omega_{x1}} + \mathbf{A^2}\underline{\omega_{x2}} + \mathbf{A^3}\underline{\omega_{x3}} = 0 \quad \text{or} \quad L(\underline{\omega}) = \mathbf{A^t}\underline{\omega_t} + \mathbf{A^i}\underline{\omega_{xi}} = 0, \tag{2.1.24}$$

where

$$\underline{\omega} = \begin{bmatrix} \underline{v} \\ \cdots \\ \underline{\sigma} \end{bmatrix}, \qquad \mathbf{A^t} = \begin{bmatrix} \rho\mathbf{I} & \vdots & \mathbf{0} \\ \cdots & \vdots & \cdots \\ \mathbf{0} & \vdots & \mathbf{S} \end{bmatrix}, \qquad \mathbf{A^i} = \begin{bmatrix} \mathbf{0} & \vdots & \mathbf{B_i} \\ \cdots & \vdots & \cdots \\ \mathbf{B_i^T} & \vdots & \mathbf{0} \end{bmatrix}. \tag{2.1.25}$$

To use this concept, an acceleration wave is introduced. This is also known as a characteristic surface along which $\phi(t, \underline{x})$ is constant and across which $\underline{\omega}$ is continuous, but derivatives of this vector can

be discontinuous. Figure 2.2 depicts this set of waves.

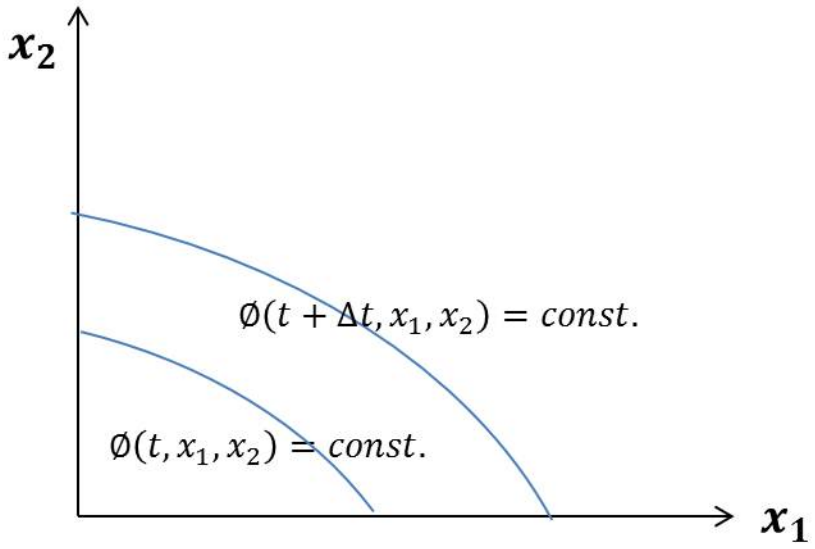

Figure 2.2: Acceleration waves along which ϕ is constant.

Let ξ_i, where $i = 1, 2, 3$, be the interior coordinates on the surface $\phi(t, \underline{x}) = constant$. Now take $\underline{\omega}$ to be a function of ϕ and ξ_i such that $\underline{\omega} = \underline{\omega}(\phi, \xi_1, \xi_2, \xi_3)$, then

$$\underline{\omega_t} = \underline{\omega_\phi}\phi_t + \underline{\omega_{\xi_i}}(\xi_i)_t \qquad \text{and} \qquad \underline{\omega_{x_i}} = \underline{\omega_\phi}\phi_{x_i} + \underline{\omega_{\xi_j}}(\xi_j)_{xi}. \tag{2.1.26}$$

Substituting this result into the expression $L(\underline{\omega}) = \underline{0}$ in Equation 2.1.24 results in

$$\left(\mathbf{A^t}\phi_t + \mathbf{A^i}\phi_{xi}\right)\underline{\omega_\phi} = -\left(\mathbf{A^t}(\xi_i)_t + \mathbf{A^i}(\xi_j)_{xi}\right)\underline{\omega_{\xi_j}}. \tag{2.1.27}$$

Since $\underline{\omega}$ must be continuous across a characteristic surface but its derivatives can be discontinuous, a surface $\phi(t, \underline{x}) = constant$, for which

$$\left(\mathbf{A^t}\phi_t + \mathbf{A^i}\phi_{xi}\right)\left\|\underline{\omega_\phi}\right\| = \underline{0}, \tag{2.1.28}$$

has non-trivial solutions that are only possible for

$$\left|\mathbf{A^t}\phi_t + \mathbf{A^i}\phi_{xi}\right| = 0, \tag{2.1.29}$$

where $\|*\|$ indicates the change of quantity $*$ from the upstream to the downstream state of the wave, or $*^+ - *^-$, respectively, and $|*|$ indicates the determinant of $*$. By substituting in the definitions of $\mathbf{A^t}$, $\mathbf{A^i}$ and $\underline{\omega_\phi}$, Equation 2.1.28 is simplified to

$$\rho \left\| \underline{v_\phi} \right\| \phi_t + \mathbf{B_i} \phi_{xi} \left\| \underline{\sigma_\phi} \right\| = \underline{0} \tag{2.1.30}$$

and

$$\mathbf{S} \left\| \underline{\sigma_\phi} \right\| \phi_t + \mathbf{B_i^T} \phi_{xi} \left\| \underline{v_\phi} \right\| = \underline{0}. \tag{2.1.31}$$

Combining these two equations, the jump in the stress tensor derivative is eliminated and a characteristic equation is obtained:

$$\left(-\rho \phi_t^2 \mathbf{I} + \mathbf{B_j S^{-1} B_i^T} \phi_{xj} \phi_{xi} \right) \left\| \underline{v_\phi} \right\| = \underline{0} \tag{2.1.32a}$$

for which

$$\left| -\rho \phi_t^2 \mathbf{I} + \mathbf{B_j S^{-1} B_i^T} \phi_{xj} \phi_{xi} \right| = 0, \tag{2.1.32b}$$

which is a 1st order, nonlinear PDE for ϕ. Let,

$$\frac{dx_i}{dt} = \frac{c\phi_{xi}}{\sqrt{\phi_{xj}\phi_{xj}}}. \tag{2.1.33}$$

Note that c is just the wavespeed and $\frac{\phi_{xi}}{\sqrt{\phi_{xj}\phi_{xj}}}$ is the normalized gradient of the characteristic surface – or the normal vector to the surface – which gives the direction the wave is propagating. Since ϕ is constant, it can be said that

$$\phi_t dt + \phi_{xi} dx_i = 0. \tag{2.1.34}$$

Therefore, rearranging Equation 2.1.34 and substituting in Equation 2.1.33 it is found that

$$\phi_t + \frac{c\phi_{xi}\phi_{xi}}{\sqrt{\phi_{xj}\phi_{xj}}} = 0 \qquad \text{or} \qquad c = -\frac{\phi_t}{\sqrt{\phi_{xj}\phi_{xj}}}. \tag{2.1.35}$$

Defining the normal to the characteristic surface as $n_i = \frac{\phi_{xi}}{\sqrt{\phi_{xj}\phi_{xj}}}$, Equation 2.1.32b reduces to

$$\left| -\rho c^2 \mathbf{I} + n_i n_j \mathbf{B_j S^{-1} B_i^T} \right| = \left| -\rho c^2 \mathbf{I} + \mathbf{B S^{-1} B^T} \right| = 0, \tag{2.1.36}$$

where $\mathbf{B} = n_j \mathbf{B_j}$

Here it should be noted that $\mathbf{BS^{-1}B^T}$ is the acoustic tensor and Equation 2.1.36 is a cubic equation for c^2. The roots of this determinant are the velocities of the acceleration wave. This

equation can now be defined in terms of the polarization vectors, which will allow for the closer study of the unique properties of the different types of waves. Allow $\left\|\underline{v_\phi}\right\| = \beta \underline{p}$, where $\underline{p}$ is the polarization vector for the velocity and describes the direction the displacement behind a wave takes place, and β is a constant. Then, Equation 2.1.32a, with the substitution of 2.1.35, becomes

$$\left(-\rho c^2 \mathbf{I} + \mathbf{B}\mathbf{S}^{-1}\mathbf{B}^{\mathbf{T}}\right) \underline{p_l} = \underline{0}, \qquad l = 1, 2, 3 \qquad \text{and} \qquad \underline{p_i} \cdot \underline{p_j} = \delta_{ij}. \tag{2.1.37}$$

For an isotropic, linear elastic solid, the inverse of the compliance matrix, $\mathbf{S}$, is the stiffness tensor, $\mathbf{C}$:

$$\mathbf{S}^{-1} = \mathbf{C} = \begin{bmatrix} \lambda + 2\mu & \lambda & \lambda & 0 & 0 & 0 \\ \lambda & \lambda + 2\mu & \lambda & 0 & 0 & 0 \\ \lambda & \lambda & \lambda + 2\mu & 0 & 0 & 0 \\ 0 & 0 & 0 & \mu & 0 & 0 \\ 0 & 0 & 0 & 0 & \mu & 0 \\ 0 & 0 & 0 & 0 & 0 & \mu \end{bmatrix}, \tag{2.1.38}$$

where λ is the first Lamé constant and μ is the shear modulus. From Equation 2.1.36, $\left|-\rho c^2 \mathbf{I} + \mathbf{B}\mathbf{S}^{-1}\mathbf{B}^{\mathbf{T}}\right| = 0$. Using the definition of $\mathbf{S}^{-1}$, it is found that

$$\mathbf{B}\mathbf{S}^{-1}\mathbf{B}^{\mathbf{T}} = \begin{bmatrix} (\lambda + 2\mu) n_1^2 + \mu\left(n_2^2 + n_3^2\right) & (\lambda + \mu) n_1 n_2 & (\lambda + \mu) n_1 n_3 \\ (\lambda + \mu) n_1 n_2 & (\lambda + 2\mu) n_2^2 + \mu\left(n_1^2 + n_3^2\right) & (\lambda + \mu) n_2 n_3 \\ (\lambda + \mu) n_1 n_3 & (\lambda + \mu) n_2 n_3 & (\lambda + 2\mu) n_3^2 + \mu\left(n_1^2 + n_2^2\right) \end{bmatrix}. \tag{2.1.39}$$

And taking the determinant of $-\rho c^2 \mathbf{I} + \mathbf{B}\mathbf{S}^{-1}\mathbf{B}^{\mathbf{T}}$ and setting it to zero results in the equation

$$\left(\mu - \rho c^2\right)\left(\mu - \rho c^2\right)\left(\lambda + 2\mu - \rho c^2\right) = 0. \tag{2.1.40}$$

This equation is satisfied if $c_1^2 = \frac{\lambda + 2\mu}{\rho}$ and $c_2^2 = c_3^2 = \frac{\mu}{\rho}$ which is independent of the normal vector to the characteristic surface. The direction of displacement can be found for a wave with each given velocity by analyzing the polarization vector associated with each case. For the first case, the relation from Equation 2.1.37, $\left(-\rho c^2 \mathbf{I} + \mathbf{B}\mathbf{S}^{-1}\mathbf{B}^{\mathbf{T}}\right) \underline{p_j^1} = \underline{0}$, where the polarization vector has a "1" superscript to denote this being the first case with corresponding velocity $c_1 = \sqrt{\frac{\lambda + 2\mu}{\rho}}$. Equation 2.1.39 can be expressed as $\mathbf{B}\mathbf{S}^{-1}\mathbf{B}^{\mathbf{T}} = \Gamma_{ij} = \mu\delta_{ij} + (\lambda + \mu) n_i n_j$. Combining 2.1.37 and 2.1.39 gives

$$\left(\left(\mu - \rho c_1^2\right)\delta_{ij} + (\lambda+\mu)n_i n_j\right)\underline{p_j^1} = \underline{0}. \tag{2.1.41}$$

Using the result for c_1, this becomes

$$\left((\mu - \lambda - 2\mu)\,\delta_{ij} + (\lambda+\mu)n_i n_j\right)\underline{p_j^1} = 0 \rightarrow \left(n_i n_j - \delta_{ij}\right)\underline{p_j^1} = 0. \tag{2.1.42}$$

Or in symbolic notation,

$$\left(\underline{n}\cdot\underline{p}^1\right)\underline{n} - \underline{p}^1 = 0 \rightarrow \underline{p}^1 = \left(\underline{n}\cdot\underline{p}^1\right)\underline{n}. \tag{2.1.43}$$

Physically, this result means that the acceleration wave with wavespeed c_1 has a displacement which is parallel to its propagation direction. This type of wave is a longitudinal wave and is shown in Figure 2.3a. Similarly, for wavespeed c_2,

$$\begin{aligned} \left(-\rho c_2^2\delta_{ij} + \Gamma_{ij}\right)\underline{p_j^2} &= \underline{0} \\ = \left(\left(\mu - \rho c_2^2\right)\delta_{ij} + (\lambda+\mu)n_i n_j\right)\underline{p_j^2} \\ = \left((\mu-\mu)\,\delta_{ij} + (\lambda+\mu)\,n_i n_j\right)\underline{p_j^2} \\ = (n_i nj)\,\underline{p_j^2}. \end{aligned} \tag{2.1.44}$$

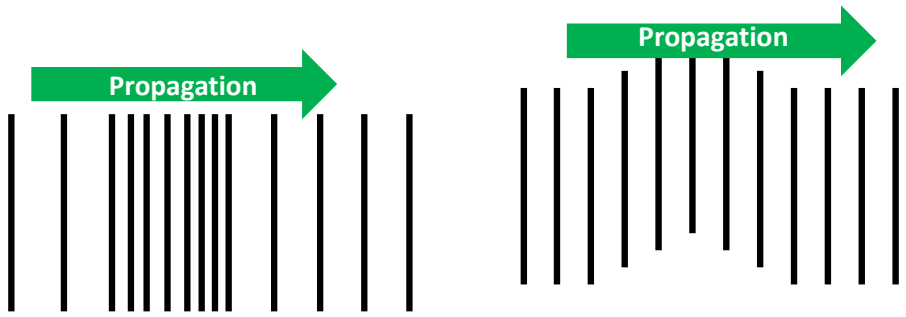

(a) Longitudinal Wave **(b)** Transverse Wave

Figure 2.3: Propagation direction vs. displacement for Longitudinal and Transverse plane waves.

In symbolic notation this is

$$\left(\underline{n}\cdot\underline{p}^2\right)\underline{n} = 0. \tag{2.1.45}$$

Thus, the waves here have a displacement that is perpendicular to the direction of motion. These

types of waves are transverse and are shown in Figure 2.3b.

Now that the velocity and direction of displacement corresponding to each type of wave are known, the change in properties across each type of wave can be found. This will be important when considering waves propagating through solid materials in the variety of targets in this study. From Equation 2.1.31, it can be shown that

$$\left\|\underline{\sigma_\phi}\right\| = \left(-\frac{1}{\phi_t}\right)\mathbf{S^{-1}B_i^T}\phi_{xi}\left\|\underline{v_\phi}\right\|. \tag{2.1.46}$$

The terms ϕ_{xi} and ϕ_t can be expressed as $\sqrt{\phi_{xj}\phi_{xj}}n_i$ and $-c\sqrt{\phi_{xj}\phi_{xj}}$, respectively, from Equation 2.1.35. Then, using these results, it is found that

$$\left\|\underline{\sigma_\phi}\right\| = \left(\frac{1}{c}\right)\mathbf{S^{-1}B_i^T}n_i\left\|\underline{v_\phi}\right\|, \tag{2.1.47}$$

where the stress polarization vector can be expressed as

$$\underline{\Sigma} = \left(\frac{1}{c}\right)\mathbf{S^{-1}B_i^T}n_i\underline{p} = \left(\frac{1}{c}\right)\mathbf{S^{-1}B^T}\underline{p} \tag{2.1.48}$$

2.1.2 Oblique Wave Incident on Interface

For a plane wave that encounters an inclined surface, Equation 2.1.48 can be used to determine the properties that change across the wave. Assume that some wave is traveling in a semi-infinite, elastic medium and that it encounters an interface which is oriented at an angle β with respect to the wave. Figure 2.4 illustrates this scenario. In this figure, $\underline{n_i^j}$ denotes the normal to a given wave, where i indicates the type of wave — L for a longitudinal wave or S for a shear wave – and j indicates the material the wave is in. Note that $j = A0$ is just the incident wave in material A. For the incident wave, $\underline{n_L^{A0}} = cos\beta\hat{i} + sin\beta\hat{j}$, which is equal to the polarization vector $\underline{p_L^{A0}}$, while for one of the transverse waves, $\underline{p_i^j}$ is perpendicular to the normal and can be found by rotating the normal by 90 degrees. For instance, the reflected transverse wave has normal vector $\underline{n_T^A} = -cos\beta_2\hat{i} + sin\beta_2\hat{j}$, with polarization vector $\underline{p_T^A} = -sin\beta_2\hat{i} - cos\beta_2\hat{j}$. The normal and polarization vectors can similarly be found for the remainder of the waves. Continuity of velocities and tractions at the interface can then be used to solve for the remainder of the parameters. The jump in particle velocities can be expressed in terms of the polarization vector as

$$\|\underline{v}\| = \alpha\underline{p}, \tag{2.1.49}$$

with α denoting the magnitude of the velocity.

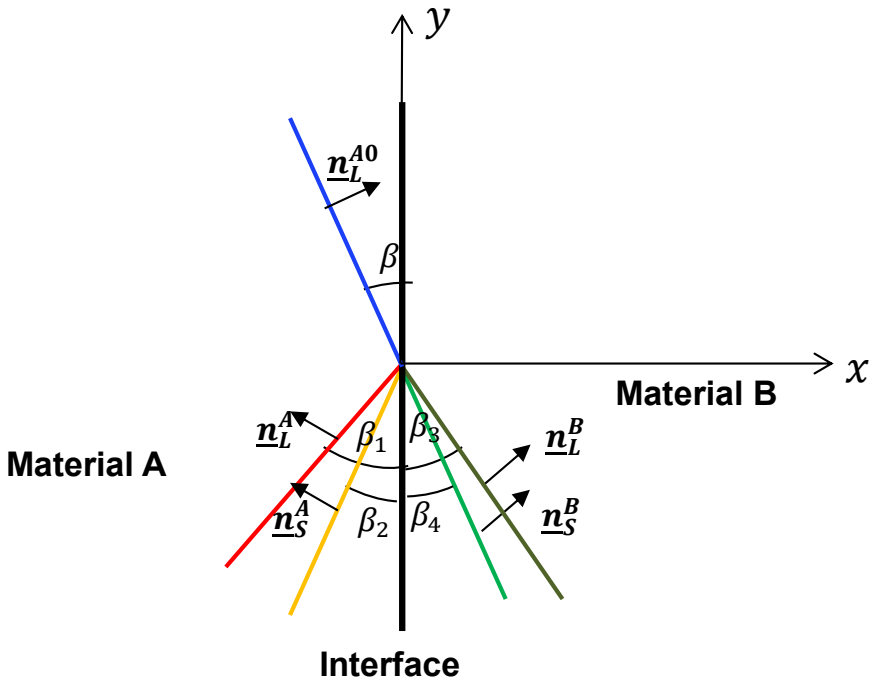

Figure 2.4: Oblique plane wave incident at an interface in a semi-infinite, elastic solid. β is the angle of the incident wave with respect to the interface, and the remaining angles, β_i, are the angles of the reflected longitudinal and shear waves, on the left of the interface, and the transmitted longitudinal and shear waves, on the right of the interface, respectively. The vectors $\underline{n}$ are normal to their respective waves and the subscripts L and S refer to longitudinal and shear waves, respectively.

For velocities to be continuous at the interface, Equation 2.1.49 can be used to give the following condition

$$\alpha_{AL}^0 \underline{p_L^{A0}} + \alpha_{AL} \underline{p_L^A} + \alpha_{AS} \underline{p_S^A} = \alpha_{BL} \underline{p_L^B} + \alpha_{BS} \underline{p_S^B}. \tag{2.1.50}$$

Similarly, the jump in stress can be expressed in terms of the polarization vector. Using Equation 2.1.48 this results in

$$\|\underline{\sigma}\| = \left(\frac{1}{c}\right) \mathbf{S^{-1}B^T} \alpha \underline{p}. \tag{2.1.51}$$

For tractions to be continuous at the interface in the x direction [22], it can be shown that

$$\|\underline{t}\,(\underline{n})\| = -\mathbf{B}\,(\underline{n})\,\underline{\sigma}. \tag{2.1.52}$$

Thus, Equation 2.1.51 can be applied in conjunction with 2.1.52 at the interface to get

$$\left(\frac{1}{c_1^A}\mathbf{B_1C^AB^T_{AL0}}\right)\alpha^0_{AL}\underline{p_L^{A0}} + \left(\frac{1}{c_1^A}\mathbf{B_1C^AB^T_{AL}}\right)\alpha_{AL}\underline{p_L^A} + \left(\frac{1}{c_2^A}\mathbf{B_1C^AB^T_{AS}}\right)\alpha_{AS}\underline{p_S^A} = \left(\frac{1}{c_1^B}\mathbf{B_1C^BB^T_{BL}}\right)\alpha_{BL}\underline{p_L^B} + \left(\frac{1}{c_2^B}\mathbf{B_1C^BB^T_{BS}}\right)\alpha_{BS}\underline{p_S^B}, \tag{2.1.53}$$

where $\mathbf{C^i}$ is the stiffness matrix for either materials A or B, and $\mathbf{B^T_{jk}}$ is the matrix $\mathbf{B}$ for material $j = A$ or B, wave $k = L$ or S, and the superscript T just means transposed. The final constraint here is to determine the angles of the reflected and transmitted waves. These can be found by using slowness surfaces. This concept is outside the scope of this thesis, but suffice it to say that the results indicate that the angle of the wave can be related to the elastic wavespeed by

$$\frac{sin\beta}{c_1^A} = \frac{sin\beta_1}{c_1^A} = \frac{sin\beta_2}{c_2^A} = \frac{sin\beta_3}{c_1^B} = \frac{sin\beta_4}{c_2^B}. \tag{2.1.54}$$

With this result, Equations 2.1.50 and 2.1.53 can be combined to form a system of four equations and the four amplitudes α_{jk}, which are unknown. Solving these equations allows one to find the jump in velocities and tractions across each wave.

2.1.3 One Dimensional Wave Propagation

Now suppose that a plane wave is traveling in a semi-infinite, elastic material and that it is parallel to the interface. This is the more common scenario encountered in experiments. Applying 2.1.22a results in

$$\rho\begin{bmatrix} v_{1,t} \\ v_{2,t} \\ v_{3,t} \end{bmatrix} = \begin{bmatrix} \sigma_{1,1} \\ \sigma_{6,1} \\ \sigma_{5,1} \end{bmatrix} + \begin{bmatrix} \sigma_{6,2} \\ \sigma_{2,2} \\ \sigma_{4,2} \end{bmatrix} + \begin{bmatrix} \sigma_{5,3} \\ \sigma_{4,3} \\ \sigma_{3,3} \end{bmatrix}. \tag{2.1.55}$$

For a longitudinal wave, the only change in displacement is in the propagation direction. If the wave propagates in the "1" direction, and it is assumed that properties only change in this direction, then

$$\rho v_{1,t} = \sigma_{1,1}. \tag{2.1.56}$$

Using equation 2.1.17, it is found that

$$\rho \frac{\partial^2 u_1}{\partial t^2} = \frac{\partial \sigma_1}{\partial x_1}. \tag{2.1.57}$$

Finally, using Equation 2.1.18 and assuming the stiffness matrix C is for an isotropic material,

$$\rho \frac{\partial^2 u_1}{\partial t^2} = (\lambda + 2\mu) \frac{\partial^2 u_1}{\partial x_1^2} \qquad \text{or} \qquad \frac{\partial^2 u_1}{\partial t^2} = c_1^2 \frac{\partial^2 u_1}{\partial x_1^2}. \tag{2.1.58}$$

A similar result can be calculated for a shear wave in which case the displacement occurs perpendicular to the direction of motion. Here it is also assumed that properties change in the x_1 direction and it is found that

$$\frac{\partial^2 u_2}{\partial t^2} = c_2^2 \frac{\partial^2 u_2}{\partial x_1^2}. \tag{2.1.59}$$

These results are known as the wave equations for longitudinal and shear waves and are well known differential equations [42], the solutions to which are

$$\sigma \pm (\rho c_1)\, v_1 = constant \qquad \text{along characteristic} \qquad \frac{dx_1}{dt} = \mp c_1 \tag{2.1.60a}$$

and

$$\tau \pm (\rho c_2)\, v_2 = constant \qquad \text{along characteristic} \qquad \frac{dx_1}{dt} = \mp c_2. \tag{2.1.60b}$$

Here, x_1 is the position, σ_1 has been replaced with σ, the longitudinal stress, σ_6 with τ, the shear stress, and v_i is the particle velocity for each wave.

2.1.3.1 One Dimensional Stress

One dimensional tension tests determine the point at which a material yields, which is the strength of the material. The stress in this case is shown in Figure 2.5 for a unit element. Assuming linear elasticity and that the material is isotropic, the constitutive relation in Equation 2.1.12b can written as

$$\epsilon_{ij} = \frac{1}{E} \left[(1 + \nu)\, \sigma_{ij} - \nu \sigma_{kk} \delta_{ij} \right], \tag{2.1.61}$$

where E is the Young's modulus and ν is Poisson's ratio. For this case, the Cauchy stress tensor is

$$\rho \begin{bmatrix} \sigma & 0 & 0 \\ 0 & 0 & 0 \\ 0 & 0 & 0 \end{bmatrix}. \tag{2.1.62}$$

Using the relation in Equation 2.1.61, the stress in the elastic region can be written as

$$\sigma = E\epsilon, \tag{2.1.63}$$

where E is Young's modulus.

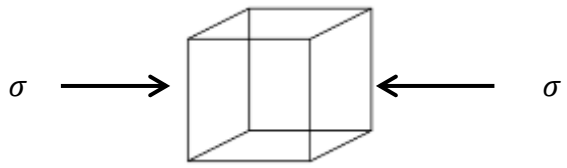

Figure 2.5: One dimensional stress on unit element.

2.1.3.2 One Dimensional Strain

For normal impact experiments, the strain can be assumed to be uniaxial [35]. This condition implies that the Cauchy stress tensor can be expressed as

$$\rho \begin{bmatrix} \sigma & 0 & 0 \\ 0 & \sigma_t & 0 \\ 0 & 0 & \sigma_t \end{bmatrix}, \tag{2.1.64}$$

where, for a unit element, the stress state is shown in Figure 2.6. In this case, the lateral stress can be expressed in terms of the longitudinal stress as such:

$$\sigma_t = \frac{\nu}{1-\nu}\sigma. \tag{2.1.65}$$

For this elastic region, the stress can be related to strain with Equation 2.1.61:

$$\sigma^e = \frac{(1-\nu)}{(1+\nu)(1-2\nu)}E\epsilon \tag{2.1.66}$$

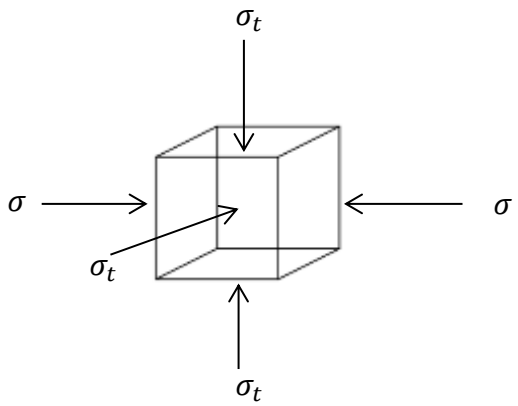

Figure 2.6: Resulting stresses from one dimensional strain assumption.

2.1.3.3 Plasticity

As the material continues to be deformed, the change can become permanent when the material yields and can be determined by defining the yield surface which bounds the region of elasticity [67]. Two such criteria are commonly used to describe this surface. The first, Tresca yield criteria, defines the yield surface under multi-axial loading conditions as

$$\frac{\sigma_{max} - \sigma_{min}}{2} = \tau_{max} = \frac{\sigma_Y^0}{2}, \tag{2.1.67}$$

where σ_{max} and σ_{min} are the maximum and minimum eigenvalues of the Cauchy stress tensor, τ_{max} is the yield stress in simple shear and σ_Y^0 is the yield stress in simple tension — this is the plastic component of stress, σ^p, for the one dimensional stress assumption in Section 2.1.3.1. The second criteria – Von Mises yield criteria – describes the yield surface as

$$\frac{1}{2} S_{ij} S_{ij} = \frac{{\sigma_Y^0}^2}{3}, \tag{2.1.68}$$

where S_{ij} is the deviatoric stress tensor and is defined in terms of the Cauchy stress tensor as

$$S_{ij} = \sigma_{ij} - \frac{1}{3}\sigma_{kk}\delta_{ij}. \tag{2.1.69}$$

In most cases, experimental results agree more closely with the Von Mises criteria. One can use these results to relate the yield stress in uniaxial strain to the yield stress in simple tension, a result which is a known material property for many materials and is readily found in simple one dimensional tension tests. Applying the Tresca criteria on the Cauchy stress tensor for one dimensional strain, it is found that

$$\sigma - \sigma_t = \sigma_Y^0. \tag{2.1.70}$$

Substituting Equation 2.1.65 into this result, and denoting the stress, σ, as the maximum stress until a material yields under uniaxial strain, σ_{HEL}, the relationship between this value and the yield stress in simple tension, σ_Y^0, is found to be

$$\sigma_{HEL} = \frac{1-\nu}{1-2\nu}\sigma_Y^0. \tag{2.1.71}$$

This result is known as the Hugoniot Elastic Limit (HEL) and it describes the transition between a purely elastic state into the plastic regime for the one dimensional strain assumption. Once the material reaches the yield stress, plasticity sets in and permanent deformation occurs. In this regime, strain can be decomposed into elastic and plastic components:

$$\epsilon = \epsilon^e + \epsilon^p \tag{2.1.72a}$$

and

$$\epsilon_t = \epsilon_t^e + \epsilon_t^p, \tag{2.1.72b}$$

where ϵ and ϵ_t are the longitudinal and tangential strains, respectively. Since this is the uniaxial strain assumption, $\epsilon_t = 0$.

It has been observed from experiments that hydrostatic pressure does not affect the yield surface and thus the plastic strains depend on the stress deviator, given by Equation 2.1.69. For this reason, plastic deformation does not affect volume change which indicates that the trace of the small strain tensor is zero

$$\epsilon_{kk}^p = \epsilon^p + 2\epsilon_t^p = 0. \tag{2.1.73}$$

Using results from Equations 2.1.72b, and substituting into Equation 2.1.73 and subsequently into Equation 2.1.72a leads to the result

$$\epsilon = \epsilon^e + 2\epsilon_t^e. \tag{2.1.74}$$

In terms of stresses, this equation can be expressed by using Equation 2.1.61 and the fact that

$\sigma - \sigma_Y^0 = \sigma_t$ from 2.1.70 to get

$$\sigma^p = \frac{E\epsilon}{3\left(1-2\nu\right)} + \frac{2}{3}\sigma_Y^0 = K\left(P\right)\epsilon + \frac{2}{3}\sigma_Y^0, \tag{2.1.75}$$

where σ has been replaced with σ^p denoting that the stress is in the plastic region, and the fact that the bulk modulus $K = \frac{E}{3(1-2\nu)}$ has been used, which is a function of pressure. This is a very interesting result since it describes the behavior of the longitudinal stress after yield. What this equation indicates is that the longitudinal stress after yield differs from hydrostatic stress — denoted by $K\left(P\right)\epsilon$ — for an equivalent strain by a factor of $\frac{2}{3}\sigma_Y^0$, where the hydrostatic assumption states that the pressure in a compressed solid is isotropic, as in the case of a gas or liquid, when pressure is large in comparison to material strength. The stress on a unit element for the hydrostatic assumption is shown in Figure 2.7. To show that the hydrostatic stress is given by $K\left(P\right)\epsilon$, Equations 2.1.74 and 2.1.61 can be used to find the total stress for the strain equivalent to the strain observed in the 1D strain assumption. Using these equations, it can be shown that $\sigma = P = \frac{E\epsilon}{3(1-2\nu)}$ which is in fact equal to $K\left(P\right)\epsilon$.

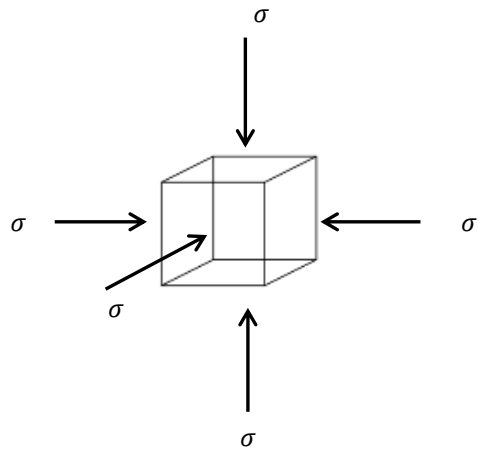

Figure 2.7: Stress on a unit element for the hydrostatic assumption.

In reality, material behavior is affected by strength and this difference is shown in Figure 2.8. In this figure, the hydrostat is compared to the one dimensional stress and one dimensional strain assumptions. From Equation 2.1.63, the one dimensional stress assumption is governed by the fact that stress is a linear function of strain and is proportional to the Young's modulus E at which point the material yields and the stress is equal to σ_Y^0. Stress for the one dimensional strain assumption is a linear function of strain, but governed by Equation 2.1.66. At the point of yield, the HEL is

reached, given by 2.1.71, and the material becomes plastic, where stress is related to strain by 2.1.75.

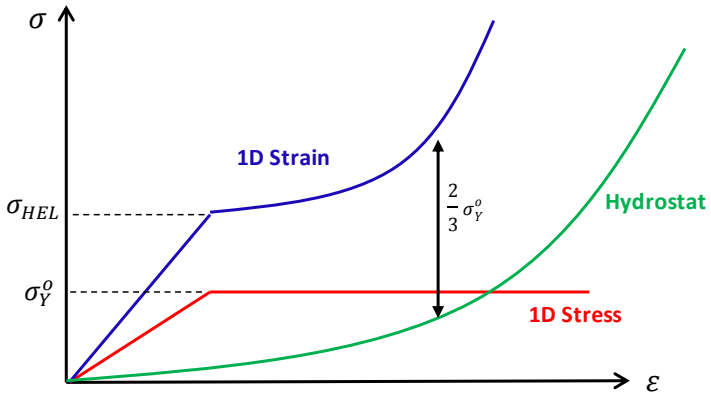

Figure 2.8: Comparison of 1D strain,1D stress and the Hydrostat.

At higher strain it must be understood how the velocity of a wave changes with deformation. From Equation 2.1.57 it was found that $\rho\frac{\partial^2 u}{\partial t^2} = \frac{\partial \sigma}{\partial x}$, the right hand side of which can be expressed as $\frac{\partial \sigma}{\partial \epsilon}\frac{\partial \epsilon}{\partial x}$, which from Equation 2.1.13 becomes $\frac{\partial \sigma}{\partial \epsilon}\frac{\partial^2 u}{\partial x^2}$ and thus results in

$$\frac{\partial^2 u}{\partial t^2} = \frac{1}{\rho}\frac{\partial \sigma}{\partial \epsilon}\frac{\partial^2 u}{\partial x^2}. \tag{2.1.76}$$

Comparing this equation to 2.1.58 indicates that the wave speed is simply a function of the density and the derivative of stress with respect to strain

$$c = \sqrt{\frac{1}{\rho}\frac{\partial \sigma}{\partial \epsilon}}. \tag{2.1.77}$$

This physically means that, as deformation increases with increased strain, the slope of the derivative of stress with respect to strain increases after the Hugoniot Elastic Limit is reached in the 1D strain curve. Thus, the velocity initially stays constant at the longitudinal elastic wavespeed when the HEL is reached at which point it increases until it reaches a steady state where a shock wave or discontinuity emerges.

2.2 Shock Wave Theory

2.2.1 Lagrangian Conservation Equations

In order to study shock waves, the first step is to analyze the impact of parallel and plane surfaces which generate the plane longitudinal waves that have been discussed. This concept is known as the plate impact experiment. The properties of the resulting waves are governed by the Lagrangian Conservation Equations. In Section 2.1, the linearized form of the conservation of momentum and mass were discussed. The other conservation equation that will be needed here is energy. These equations will now be discussed in the Lagrangian Frame.

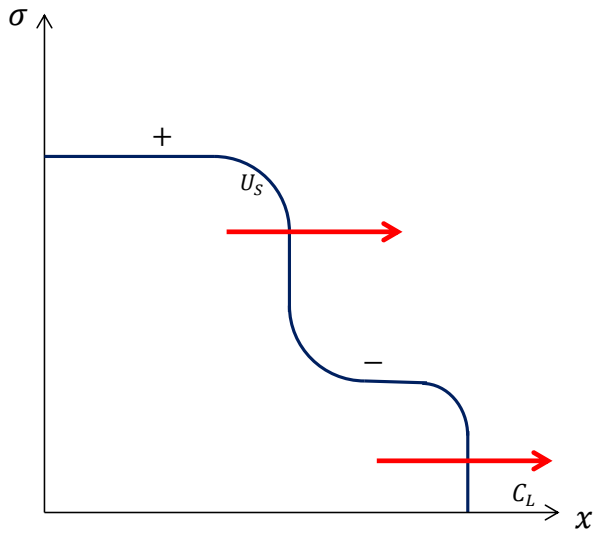

Figure 2.9: Progression of an elastic longitudinal wave into a steady shock wave.

In Figure 2.9, a basic schematic of a two-wave system that occurs in plate impact experiments is shown. Here there is an elastic wave traveling at a constant wavespeed that progresses into a steady shock wave. Upstream of the shock, the properties are denoted by a "-" sign and downstream of the shock the properties are denoted by a "+" sign. It can be shown that the local conservations of mass, momentum and energy that govern the jump from the upstream to the downstream conditions can be expressed as [24]

$$u^+ - u^- = -\rho_0 U_S \left(V^+ - V^-\right), \tag{2.2.1}$$

which is the conservation of mass,

$$\sigma_{11}^{+} - \sigma_{11}^{-} = \rho_0 U_S \left(u^{+} - u^{-}\right), \tag{2.2.2}$$

the conservation of momentum, and

$$\sigma_{11}^{+} u^{+} - \sigma_{11}^{-} u^{-} + Q^{+} - Q^{-} = \rho_0 U_S \left(E^{+} - E^{-} + \frac{1}{2}\left(u^{+^2} - u^{-^2}\right)\right), \tag{2.2.3}$$

the conservation of energy. Here, u is the particle velocity in the direction of shock wave propagation, not to be confused with the displacement u discussed in the elastic wave theory in Section 2.1. The reason for the change in nomenclature for the particle velocity is to stay consistent with the equations in literature. For the remaining variables, ρ_0 is the initial density, V is the specific volume, U_S is the shock wave speed, σ_{11} is the Cauchy stress in the wave propagation direction, Q is the heat flux, and E is the specific internal energy. The jump in these properties across the wave can be expressed in a similar manner. If the upstream components of density, stress, specific energy, velocity and specific volume are denoted as ρ_0, σ_0, E_0, u_{p0}, and V_0, respectively, and the downstream density, stress, velocity, specific energy, and specific volume are defined as ρ, σ, u_p, E, and V, respectively, where it has been assumed the transition between the unshocked and shocked state is adiabatic, the following relations for the conservation of mass, momentum and energy are obtained:

$$\rho_0 U_S \left\|V\right\| = \left\|u_p\right\| \tag{2.2.4}$$

$$\rho_0 U_S \left\|u_p\right\| = \left\|\sigma\right\| \tag{2.2.5}$$

and

$$\left\|E\right\| = \frac{1}{2}\left(\sigma + \sigma_0\right)\left\|V\right\|, \tag{2.2.6}$$

respectively. These equations are collectively known as the Rankine-Hugoniot jump relations. At this point there are three equations and 5 unknowns. One of these unknowns can be eliminated with a constitutive relation between the particle velocity and shock velocity, which is a linear relationship for many materials [50],

$$U_S = C_0 + S u_p. \tag{2.2.7}$$

Here, C_0 is the bulk sound speed at zero stress and S is an empirical constant. In an experiment, one of the variables is generally measured and thus three equations and three unknowns are left. Note that, Equation 2.2.5 can also be obtained from the wave characteristics discussed in Section 2.1.3. In Equation 2.1.60a, for a positive moving wave (or positive characteristic), $\sigma - (\rho c_1)\, u_1 = constant$. So, replacing c_1 with U_S leads to $\sigma^+ - (\rho_0 U_S)\, u^+ = \sigma^- - (\rho_0 U_S)\, u^-$, which rearranges to Equation 2.2.5. This same analysis can be applied to Equation 2.1.60b to obtain the jump relation for a shear wave, which is given as

$$\rho_0 C_S \left\| v_p \right\| = \left\| \tau \right\|, \tag{2.2.8}$$

where v_p is the particle velocity perpendicular to the motion of the shear wave.

2.2.2 Hugoniot

An important concept in shock physics is the Hugoniot, which is a collection of points that describe the shocked state for a given material. This state can be given by a combination of two variables [68]. For one such example, the stress vs. volume Hugoniot, the jump between two points can be described by the Rayleigh line. This jump is found by combining Equations 2.2.4 and 2.2.5 to get

$$\frac{\left\| \sigma \right\|}{\left\| V \right\|} = \rho_0^2 U_S^2. \tag{2.2.9}$$

This line is useful when performing experiments as it relates the upstream and downstream quantities across a shock. With each experiment, the points on the Hugoniot can be filled in to describe the entire behavior of a material in the shocked state. Figure 2.10 illustrates this concept.

2.2.3 Impedance Matching

Upon impact, two waves are generated, one traveling into the target and the other back into the impactor. One can use the jump equations to graphically determine what occurs in such an impact. This is known as impedance matching [51]. Figure 2.11 shows the scenario for a plane impact situation. It is assumed here that once the impactor hits the target, a no slip condition is formed at the interface between the two materials. For this reason, stress and particle velocities must be equal, thus the stress vs. particle velocity Hugoniot for the two materials can be plotted to find where they intersect in order to solve the problem. This analysis is shown in Figure 2.12.

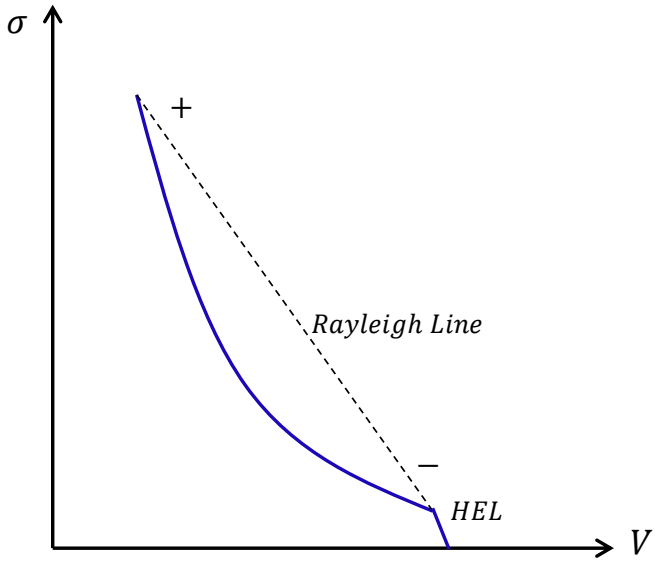

Figure 2.10: Stress vs. volume Hugoniot with Rayleigh line connecting upstream and downstream states of a shock wave.

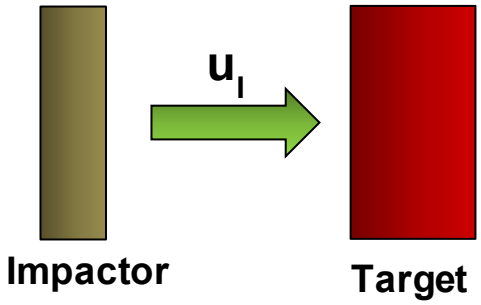

Figure 2.11: Normal Impact.

Using Equation 2.2.5, it is found that

$$\sigma_I = -\rho_{0I} U_{SI} \left(u_p - u_I\right) = \rho_{0T} U_{ST} u_p, \tag{2.2.10}$$

where it should be noted that the velocity for the shock traveling into the impactor is negative. At this point, one can use the known $U_S - u_p$ Hugoniot for each material and the measured impact velocity to solve for the in-situ particle velocity. Conversely, if the $U_S - u_p$ relationship is unknown for one of the materials, the particle velocity and impact velocity can be measured and used to solve for the shock velocity.

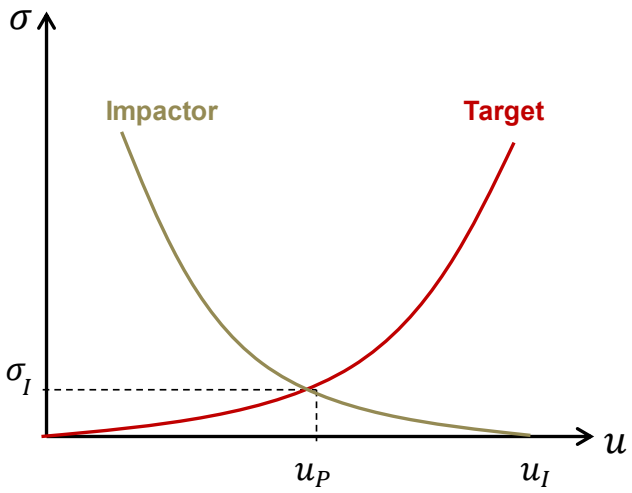

Figure 2.12: Impedance matching for normal impact experiments.

2.2.4 Shock Polar Analysis

Although calculating the change in various properties across a normal shock wave is relatively straightforward, this process becomes more complicated for the case of oblique shock waves. Much like the oblique elastic waves incident on an interface, shock waves that approach another material at an angle also generate pressure and shear waves in both materials. Generally speaking, the shear wave will still remain elastic, but the reflected and transmitted waves will form a shock. To study the effects of the shock waves, shock polar analysis [13], [14] can be implemented. This technique will only briefly be mentioned here, but it is discussed in detail by Justin Brown in his thesis [13]. Essentially, one can borrow concepts from oblique wave studies in fluid dynamics by analyzing the flow of material across a shock wave in the Eulerian frame, or the frame of the shock. In Figure 2.13a, the shock velocity and particle velocity are shown in the Lagrangian or laboratory frame. This same situation can be expressed in the Eulerian frame, which is the frame of the stationary shock, as in Figure 2.13b

In the Eulerian frame, the equations for mass and momentum conservation can be expressed as

$$\rho_1 u_1 = \rho_2 u_2 \tag{2.2.11}$$

and

$$P_1 + \rho_1 u_1^2 = P_2 + \rho_2 u_2^2, \tag{2.2.12}$$

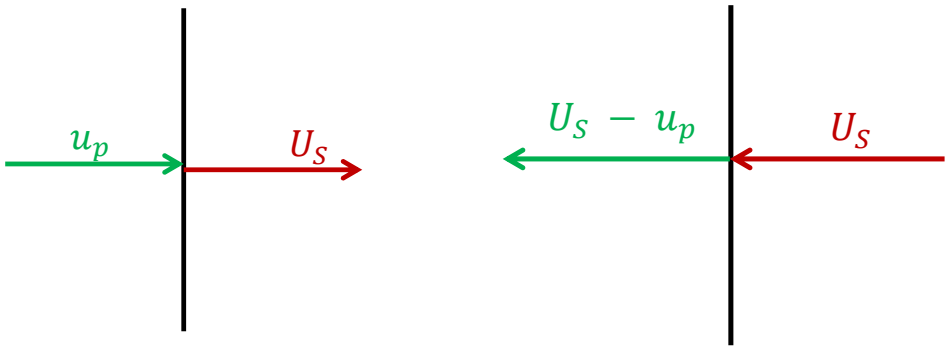

(a) Lagrangian Frame **(b)** Eulerian Frame

Figure 2.13: Shock and particle velocities across a moving shock wave.

where state "1" refers to the upstream state of the shock, "2" refers to the downstream state, u is the flow velocity, ρ is the density and P is the pressure. For high velocity impacts, the hydrodynamic assumption can be used for the primary shock wave prior to the shear wave arrival – since the pressure greatly exceeds the strength of the material. This allows for the angle of the transmitted longitudinal shock wave to be determined, which is essential for the oblique wedge target design, to be discussed later. For an oblique shock wave, the situation is illustrated in Figure 2.14.

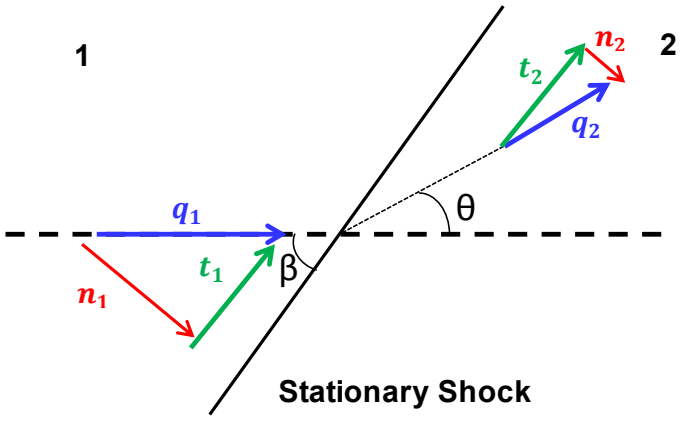

Figure 2.14: Flow across an oblique shock wave incident on an interface in the frame of the shock. β is the angle of obliquity of the shock, q is the flow velocity, n is the normal component of the flow velocity, t is the tangential component of the flow velocity, and θ is the deflection angle of the flow across the shock. The subscripts 1 and 2 denote the upstream and downstream states across the shock, respectively.

Here the shock is described as "stationary", which refers to the fact that the flow is observed in the frame of the shock. β is the angle of obliquity of the shock wave, θ is the deflection angle of the flow downstream of the shock, q is the flow velocity, n is the component of velocity normal to the flow, and t is the component of velocity tangential to the flow. Since there is no pressure change along the shock, applying the conservation of momentum for the Eulerian frame in Equation 2.2.12 results in

$$\rho_1 n_1 t_1 = \rho_2 n_2 t_2 \tag{2.2.13}$$

and substituting in the conservation of mass implies the important result

$$t_1 = t_2, \tag{2.2.14}$$

which indicates that the tangential component of velocity remains constant across a longitudinal shock wave. Thus, only the change in the normal components across the wave front need to be examined. Analyzing Figure 2.14, it is found that

$$q_1 sin\beta = n_1 \tag{2.2.15}$$

$$tan\beta = \frac{n_1}{t_1} \tag{2.2.16}$$

and

$$tan\,(\beta - \theta) = \frac{n_2}{t_2}. \tag{2.2.17}$$

From Figure 2.13b, $n_1 = U_S$ and $n_2 = U_S - u_p$, which can be substituted into Equations 2.2.15 – 2.2.17 to find

$$sin\beta = \frac{U_S}{q_1} \tag{2.2.18}$$

$$tan\beta = \frac{U_S}{t_1} \tag{2.2.19}$$

and

$$tan\,(\beta-\theta)=\frac{U_s-u_p}{t_2}. \tag{2.2.20}$$

Applying the trigonometric equation

$$tan\,(\beta-\theta)=\frac{tan\beta-tan\theta}{1+tan\beta tan\theta} \tag{2.2.21}$$

to Equation 2.2.20 and then using the Pythagorean theorem for right triangles, which leads to the relation $U_S^2+t_1^2=q_1^2$, the important relationship between shock velocity, particle velocity and deflection angle is obtained

$$tan\theta=u_p\frac{\sqrt{q_1^2-U_S^2}}{q_1^2-u_pU_S}. \tag{2.2.22}$$

In order to relate the pressure to the flow angle downstream of the shock wave, the mass and momentum conservation equations can once again be used to find the relation between pressure, density, shock wave velocity and particle velocity, where it has been assumed that the upstream pressure and particle velocity are zero. This gives

$$P_2=\rho_1U_Su_p. \tag{2.2.23}$$

Equation 2.2.23 is then used in conjunction with the linear U_S-u_p relation in 2.2.7 to relate the shock and particle velocities to the pressure, density and known empirical constants in the linear U_S-u_p relation resulting in the following equations

$$u_p=\frac{C_0}{2S}\left[\sqrt{1+\frac{4SP}{\rho_0C_0^2}}-1\right] \tag{2.2.24}$$

and

$$U_S=\frac{C_0}{2}\left[\sqrt{1+\frac{4SP}{\rho_0C_0^2}}+1\right]. \tag{2.2.25}$$

These relations can then be substituted into Equation 2.2.22 to give the resulting pressure versus deflection angle equations that are used in shock polar analysis.

Two situations, which must also be mentioned for completeness, that occur for oblique waves incident on an interface are reflected shock waves or reflected expansion waves. In the former situation, one must look at the re-shock Hugnoniot for pressure vs. volume, as shown in Figure

2.15. Here the material reaches some state "+" after the primary incident shock at which point the reflected shock wave changes the material to some state along the re-shock Hugoniot [64]. This final state is found using the energy Equation 2.2.6 from the Rankine Hugoniot relations to relate the energy states at the shock and re-shock states to the reference state as such

$$E^{H2}(V) = E^{+} + \frac{1}{2}\left(P^{H2}(V) + P^{+}\right)\left(V^{+} - V\right) \tag{2.2.26a}$$

$$E^{H2}(V) = E_0 + \frac{1}{2}P^{H2}(V)\left(V_0 - V\right) \tag{2.2.26b}$$

and

$$E^{+} = E_0 + \frac{1}{2}P^{+}\left(V_0 - V^{+}\right), \tag{2.2.26c}$$

where 2.2.26a relates the re-shock energy E^{H2} to the energy, pressure and volume after the first shock, denoted by the "+" sign, and the pressure and volume at the re-shocked state P^{H2} and V. These energies at the re-shock and shocked states are then related to the reference state, 0, in 2.2.26b and 2.2.26c. The three equations can then be substituted into the Mie-Grüneisen equation of state which is a thermodynamic equation of state that describes processes off of the Hugoniot curve. This model is given by

$$P^{H2}(V) - P^{H}(V) = \frac{\gamma(V)}{V}\left[E^{H2}(V) - E^{H}\right], \tag{2.2.27}$$

where P^H and E^H are any state along the principal Hugoniot and γ is the Grüneisen coefficient. Finally, one can eliminate the energy terms in 2.2.27 using the relations in 2.2.26a – 2.2.26c to get

$$P^{H2}(V) = \frac{P^{H}(V)\left[1 - \frac{\gamma(V)}{2V}\left(V^{0} - V\right)\right] + \frac{\gamma(V)}{2V}P^{+}\left(V^{0} - V\right)}{1 - \frac{\gamma(V)}{2V}\left(V^{+} - V\right)}. \tag{2.2.28}$$

Once again, momentum and mass conservation equations can be used to relate pressure to particle and shock velocities and then to the deflection angle, much like the analysis done for the incident shock wave.

Graphically, this analysis is shown in Figures 2.16 and 2.17. In Figure 2.16 , the flow across each of the shock waves is shown. In both materials 1 and 2, the pressure and flow angle starts at zero where the flow velocity, q_1 is equal for both. At this point the flow is deflected across the incident wave into material 1 and the transmitted wave in material 2. Next, the flow is deflected across the

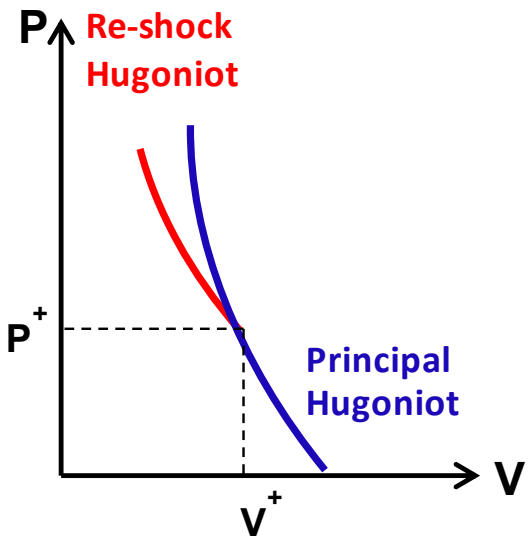

Figure 2.15: Reshock Hugoniot for a reflected shock wave.

reflected shock wave at which point the no slip condition must be applied at the interface. Here it is assumed that the pressure and deflection angle are equal for both the flow after the reflected shock and the flow after the transmitted shock since it is along the same interface. The method to find the pressure and deflection angles after each wave is shown in Figure 2.17. Here the pressure vs. deflection angle shock polar is drawn for each of the states 1, 2, 3 and 4 and the intersections are shown where these quantities are equal. Implementing such an analysis with the equations discussed above yields results for the pressure and deflection angles which can then be used to find the remaining properties in the flow from the above equations, specifically the angle of obliquity of the transmitted shock which is given by 2.2.22, shown as β_4 in Figure 2.16, where

$$tan\beta_4 = \frac{u_{pt}\sqrt{q_1^2 - U_{S3}^2}}{q_1^2 - u_{pt}U_{S3}}. \tag{2.2.29}$$

In this equation, u_{pt} is the particle velocity and U_{S3} is the shock velocity of the transmitted shock-wave. Note that here, the reason that the deflection angle is used to find the angle of obliquity of the transmitted shock is that the angle with respect to the original position of the interface is sought, which is given by the deflection angle of the flow. For the case of the reflected expansion wave, one can refer to Section 2.2.3.2 in [13].

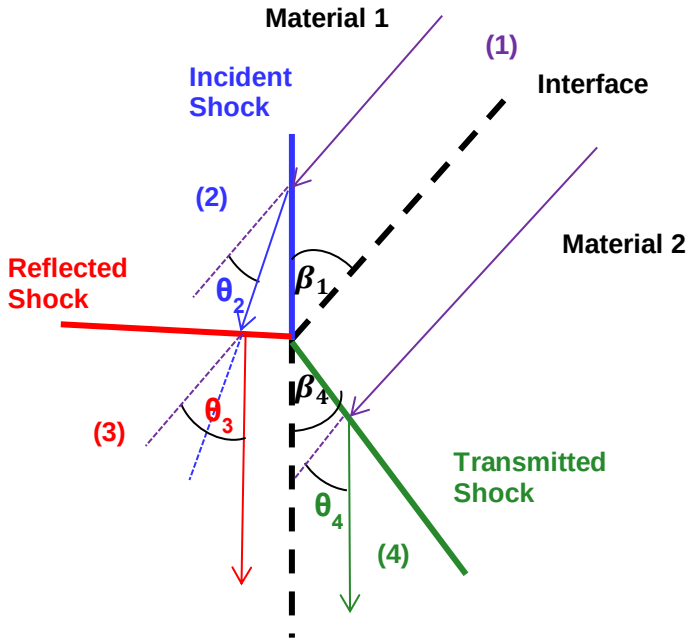

Figure 2.16: Flow in two materials with an incident, reflected and transmitted shock wave.

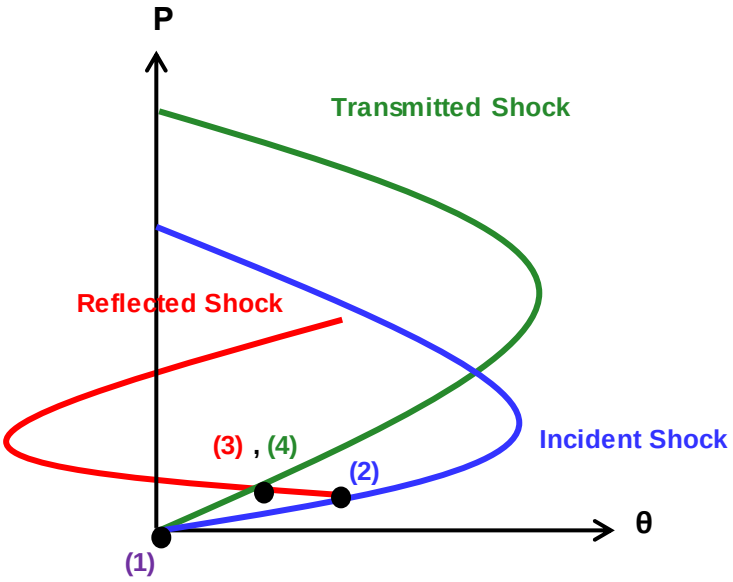

Figure 2.17: Shock polar analysis relating pressure to deflection angle of flow in two materials with an incident, reflected and transmitted shock wave.

Chapter 3

Oblique Wedge Configuration

3.1 Introduction

The oblique wedge configuration is a novel technique to test the effects of shear on a material. In this experiment, a plane wave is generated upon impact in the driver material. As it propagates through the driver, it encounters the inclined interface of the target where it is reflected back into the driver and transmitted into the target as an oblique shock wave, followed by a shear wave. By using shock polar analysis, described in Section 2.2.4, the angle of the transmitted shock wave in the target is predicted, allowing the rear surface of the target to be machined parallel to the angle of obliquity of this wave. This technique mitigates any angled reflections of the waves at the target-window interface allowing for the shear response of the transverse wave to be measured.

Figure 3.1 shows the wave state in the composite target. Although shock polar analysis can be used to determine the hydrodynamic state, the primary focus here is to measure the deviatoric response from the shear wave that follows the transmitted shock wave, which results due to the angle of obliquity of the incident shock with respect to the target. To study this response, particle velocities can be measured at the rear surface of the target using interferometery discussed in detail in Section 5.2. From these velocities, longitudinal and shear stresses can be calculated at the target-window interface using Equations 2.2.5 and 2.2.8. Since the transmitted shock travels into a quiescent material, and the shear wave travels into a material that has no shear velocity present, the resulting equations for the two stresses are

$$\sigma = \rho_0 U_S u_p \tag{3.1.1}$$

and

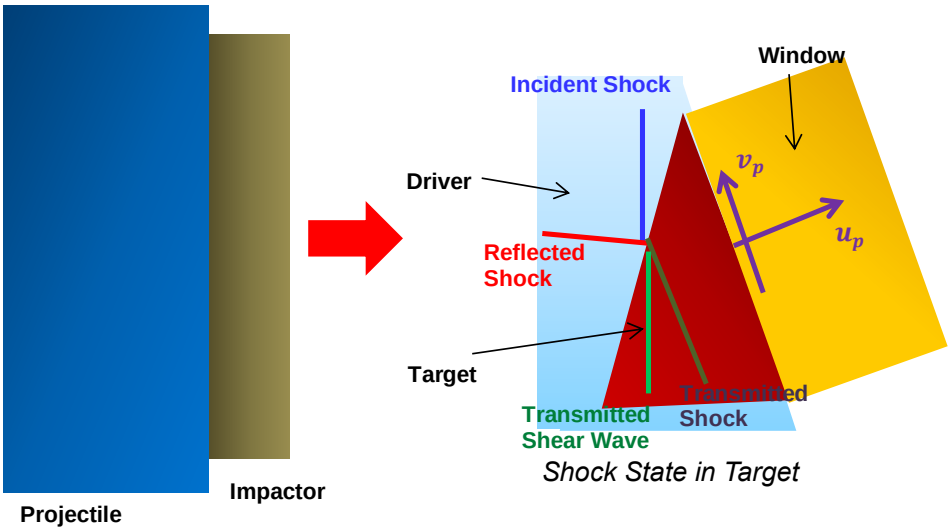

Figure 3.1: Schematic of the oblique wedge impact experiment. Upon impact, a longitudinal shock wave is generated in the driver and is reflected and transmitted at the driver-target interface where it is followed by a shear wave.

$$\tau = \rho_0 C_S v_p. \tag{3.1.2}$$

3.2 Predicting the Shear Wave Angle

Similar to the case of an elastic wave approaching an interface at an angle, with a shock wave, there are both longitudinal and shear waves present that are not parallel to one another. To find the angle of the transmitted shear wave, Equation 2.1.54 can be used. For this case, it is found that

$$\frac{sin\beta}{U_S} = \frac{sin\delta}{C_S}, \tag{3.2.1}$$

where δ is the angle of the shear wave with respect to the interface. This angle is shown in Figure 3.2

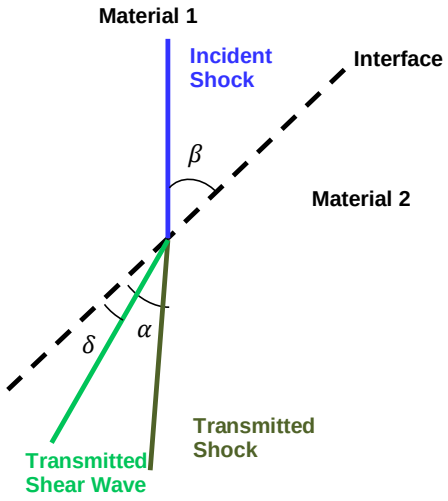

Figure 3.2: Incident and transmitted shocks with transmitted shear wave.

3.3 Analysis of Target Parameters

3.3.1 Longitudinal Stress vs. Angle of Obliquity

The oblique wedge configuration can be modified in a variety of ways ranging from the driver and target materials, to the angle of obliquity of the target and the material of the impactor and its impact velocity. In order to analyze how these modifications will affect the wave state in the target, a variety of parameters were studied. The first of these was the longitudinal stress obtained as a function of angle of obliquity. These parameters are especially important in studying the shear response at different pressures. In order to find the longitudinal stress, shock polar analysis was used to find the pressure – which estimates the longitudinal stress in these plots – for a variety of different angles of obliquity. This analysis was conducted for a copper impactor at 1.0 km/s and 1.2 km/s impact velocity and aluminum 6061-t6 and tantalum targets. The driver materials used were polymethylmethacrylate (PMMA), copper (Cu), molybdenum (Mo), and tantalum (Ta).

In both Figures 3.3a and 3.3b, it can be seen that with an increase of impact velocity, the longitudinal stress observed also increases. For both the aluminum and tantalum targets, the PMMA driver continues to increase the stress with increasing angle of obliquity. The tantalum and copper drivers both decrease in stress initially and then again increase for the aluminum target, and molybdenum continues to decrease in stress with increasing angle of obliquity. For the tantalum target, the aluminum driver stays fairly constant in stress, whereas the molybdenum and copper drivers cause a continued decrease in stress in the target. In this analysis, the angle of obliquity was cut off

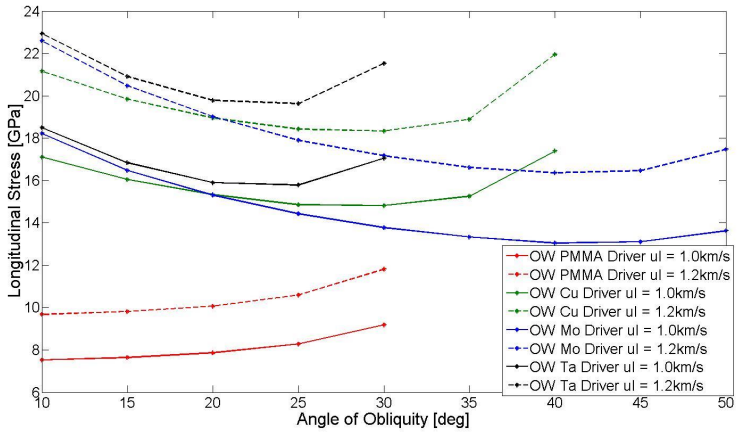

(a) Aluminum 6061-t6 target and a copper impactor.

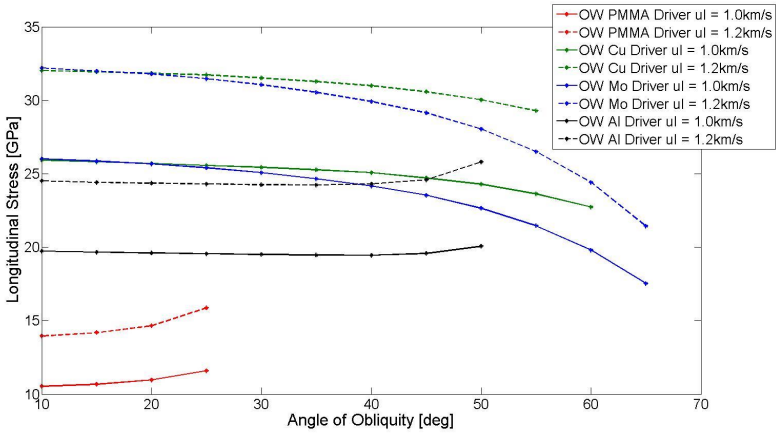

(b) Tantalum target and a copper impactor.

Figure 3.3: Longitudinal Stress vs. Angle of Obliquity for polymethylmethacrylate (PMMA), copper (Cu), molybdenum (Mo), tantalum (Ta) and aluminum (Al) drivers with two different targets and a copper impactor. In the legend, OW stands for oblique wedge, and uI is the impact velocity.

Material	Density (g/cm^3)	Longitudinal Wavespeed (km/s)	Impedance ($kg/m^2/s$)x10^6
Aluminum 6061-T6	2.703	6.4	17.3
Tantalum	16.656	4.16	69.29
PMMA	1.186	2.72	3.23
Copper	8.924	4.76	39.48
Molybdenum	10.208	6.44	65.74

Table 3.1: Density, longitudinal wavespeed and longitudinal impedance for 6061-t6 aluminum, tantalum, polymethylmethacrylate (PMMA), copper and molybdenum [60]

at the point where the reflected shock (or expansion wave) separated from the interface, which is marked by no intersection in the shock polars. Overall, it appears that an increase in impact velocity results in a higher longitudinal stress state, but the effect of the material of the driver depends on the material used. This latter observation can be elucidated by studying the impedance mismatch in the driver and target.

In Table 3.1, it can be seen that the only material that has a lower impedance than aluminum is PMMA, which is the only material that results in an increased stress in the target with increasing angle of obliquity. For the tantalum target, it is interesting to note that all of the drivers have a lower impedance, but the PMMA still causes the same trend in this target as it does in the aluminum. The aluminum driver also causes a slight increase in stress with increased obliquity, while the other drivers cause a decrease. This result could be due to the large difference in impedance between the PMMA and aluminum drivers with the tantalum target, whereas the other impedances are not quite as different. From these observations, it is not very clear if the impedance mismatch directly correlates with the behavior of the longitudinal stress with increased angle of obliquity, however, in general the higher the impedance of the driver, the larger the resulting longitudinal stress in the target for lower angles of obliquity. At higher angles, this trend seems to change.

3.3.2 Transmitted Shear Wave Angle vs. Transmitted Shock Wave Angle

Another parameter that can be analyzed is the transmitted shear wave angle as a function of the transmitted shock wave angle. For this calculation, shock polar analysis was used to find the transmitted shock wave angle for a variety of combinations of targets. To find the shear wave angle, Equation 3.2.1 was used, where the shear wave velocity for a target was taken to be the elastic shear wave speed [60] and the shock velocity was found by using impedance matching. The results of this study are shown in Figures 3.4a and 3.4b.

From these figures, it can be seen that there is a linear relationship between the shear wave

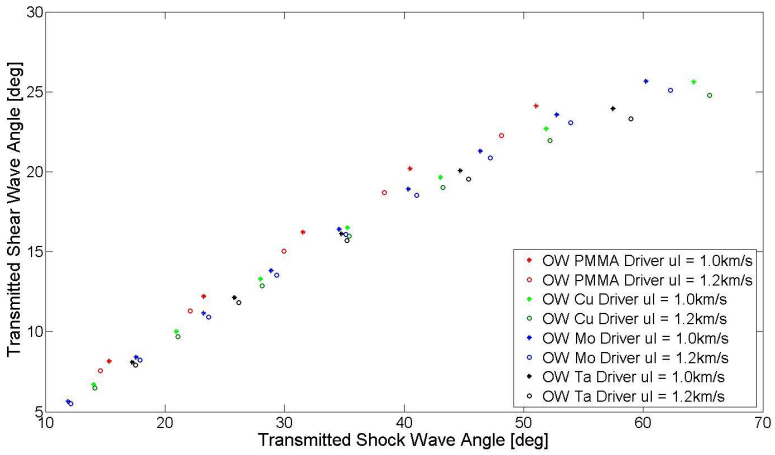

(a) Aluminum 6061-t6 target and a copper impactor.

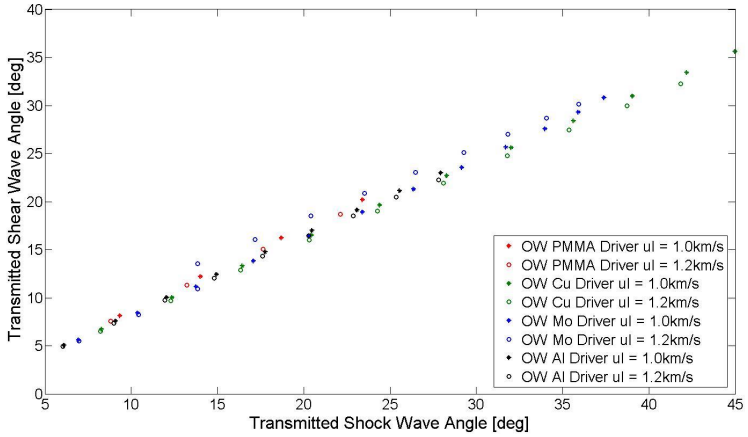

(b) Tantalum target and a copper impactor.

Figure 3.4: Shear Wave Angle vs. Transmitted Shock Wave Angle for polymethylmethacrylate (PMMA), copper (Cu), molybdenum (Mo), tantalum (Ta) and aluminum 6061-t6 (Al) drivers with two different targets and a copper impactor. In the legend, OW stands for oblique wedge, and uI is the impact velocity.

angle and shock wave angle and that, as the transmitted shock wave angle increases, so does the transmitted shear wave angle. This is the case for a variety of drivers and increasing impact velocity.

3.3.3 Transmitted Shear Wave Angle vs. Angle of Obliquity

The final relationship of interest is the shear wave angle as a function of the angle of obliquity. Once again, the shear wave angle was found using Equation 3.2.1 and the angle of obliquity was varied independently. The impact velocities examined were also 1.0 km/s and 1.2 km/s. Figures 3.5a and 3.5b show the results. In these two figures, it can be seen that the shear wave angle increases with increasing angle of obliquity for all of the drivers. For both the aluminum and the tantalum targets, the shear wave angle is larger for a smaller impact velocity. Furthermore, depending on the given driver, the shear wave angle is also larger for a given angle of obliquity.

The three types of analyses described above can be used as a guide to determine the response of the experiment for parameters the experimentor can control — angle of obliquity, impact velocity, and the driver, target, and impactor materials. For instance, if an experimentor would like to determine the shear response of the target with increasing longitudinal stress, they can increase the impact velocity or, in some cases, increase the impedance of the driver.

3.4 Target Design

In order to design the composite target (driver and target) shown in Figure 3.1, the diameter of the target as well as the thicknesses of each of the materials were considered. Initially, the target was designed to be studied at the Caltech powder gun facility in the Mechanics of Materials Group. The gun used, described in Section 5.1.1, utilizes an impactor that is 34 mm in diameter. For this reason, the target was designed to be slightly smaller than this diameter – at 30 mm – in order to avoid any edge effects that could occur upon impact. Although these experiments were eventually conducted at Sandia National Laboratories, where the gun is much larger, as illustrated in Section 5.1.2, the targets originally machined for the Caltech gun were still used. Another design consideration was the actual wedged target sample, designed to have a controlled angle of obliquity out front, as well as a rear surface angle that was parallel to the transmitted longitudinal wave previously discussed. This study considered designing the rear surface to be either parallel to the shear wave or at 45 degrees with respect to the principal stresses, but it was determined that machining parallel to the shock wave would be the best approach. Initially, it was thought that at 45 degrees with respect to

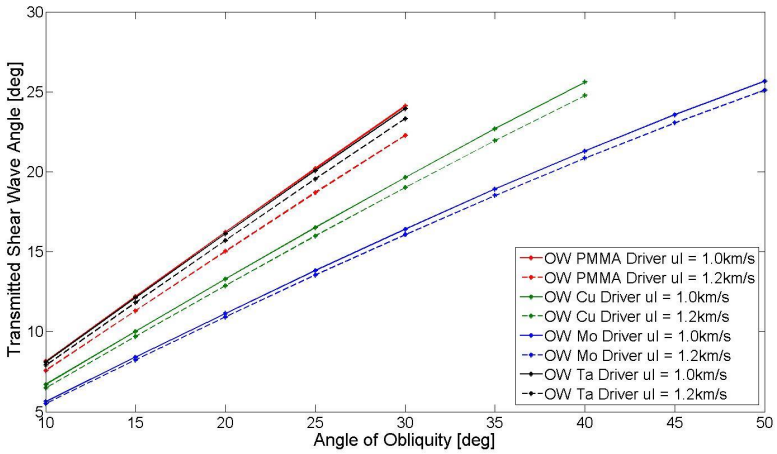

(a) Aluminum 6061-t6 target and a copper impactor,

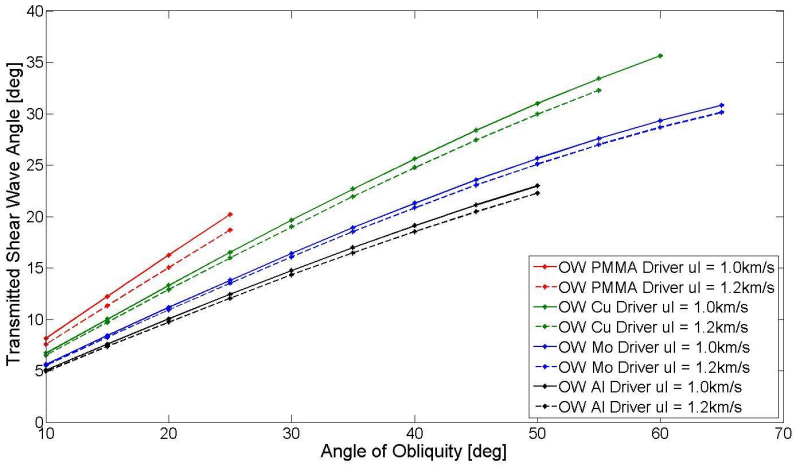

(b) Tantalum target and a copper impactor.

Figure 3.5: Shear Wave Angle vs. Angle of Obliquity for polymethylmethacrylate (PMMA), copper (Cu), molybdenum (Mo), tantalum (Ta) and aluminum 6061-t6 (Al) drivers with two different targets and a copper impactor. In the legend, OW stands for oblique wedge, and uI is the impact velocity .

the principal stresses, a maximum shear stress would be seen, but this only led to both the shear and longitudinal waves being reflected at different angles at the rear surface at which point it was difficult to determine the material response. Machining parallel to the shear wave was also thought to mitigate reflections of the shear wave, nevertheless, since the longitudinal wave has a significant effect on the longitudinal velocity component in the target, and its angled reflection produces a shear response separate from the shear wave in question, its angled reflection at the rear surface was also a problem. Simulations were conducted with this configuration and it was found that shear tractions calculated from the transverse particle velocity deviated from the shear stress given by the stress tensor. It was thus decided to design the rear surface of the wedge to be parallel to the shock. Upon making this decision, the following considerations were made for the thicknesses of the composite target, impactor and window.

3.4.1 Edge Wave Analysis

To study the full wave state behind the shock and subsequent shear wave, the material response behind these waves prior to the arrival of the edge waves at the measurement surface must be seen. The first step is to calculate the time for the shock wave to travel from the impactor-driver interface to the closest point on the driver-target interface. This distance, labeled d_1, is shown in Figure 3.6.

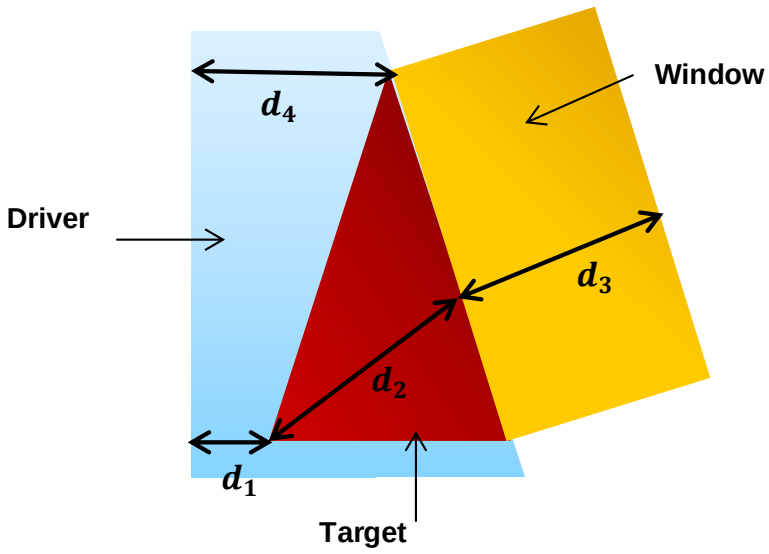

Figure 3.6: Distances waves must travel in each of the materials in the composite target.

The time it takes the incident wave to travel distance d_1 is

$$t_1 = \frac{d_1}{U_S^D}, \tag{3.4.1}$$

where U_S^D is the shock wave velocity of the incident wave, found by using impedance matching, see Section 2.2.3, upon impact. The time for the transmitted shock to travel in the target is given by

$$t_2 = \frac{d_2}{U_S^T}, \tag{3.4.2}$$

where d_2 is perpendicular to the transmitted shock wave front and U_S^T is the transmitted shock velocity, found by using shock polar analysis 2.2.4. It should be noted here that time $t_1 + t_2$ is equal to the time it takes the incident wave to travel to the top of the target, or

$$t_4 = \frac{d_4}{U_S^D} = t_1 + t_2. \tag{3.4.3}$$

Since the shear wave following the shock in the target propagates at a different angle with respect to the rear surface, it can be estimated that an additional microsecond is needed to see the response following it. A similar approach can be followed with the timing of the shear wave arrival as that of the shock, however, the estimated angle of the shear wave only applies when the shear wave is purely elastic. Nevertheless, since the shear modulus behind the shock changes, the calculated shear wave velocity, given by $c_2^2 = \frac{\mu}{\rho}$, may be different. This is of course only an estimate and thus to check that the full shear response is observed, numerical simulations, discussed in Section 3.6, can be implemented. With this estimate, the edge waves should come in no sooner than time $t_4 + 1$ μsec. A common estimate for edge wave arrival is to assume that edge waves travel radially inward from the point of impact, as shown in Figure 3.7.

As can be seen in Figure 3.7, upon impact the initial waves are shown to travel radially into the driver material. However, since the target itself is a wedge, it can be assumed that the front most point of the material is where the edge waves begin to propagate in the wedge. It has been estimated that the edge waves propagate at the same velocities as the shock waves in the materials, as a worst case estimate. The distance that these waves must propagate are denoted as S_1 and S_2, where S_1 measures the distance from the corner of the driver to the closest corner of the target and S_2 is the distance between the latter corner and the center of the rear surface of the window. Note that here it is assumed that the target and window are well matched and thus the edge wave continues to travel into the window at the same velocity as in the target. With these estimates, one must then

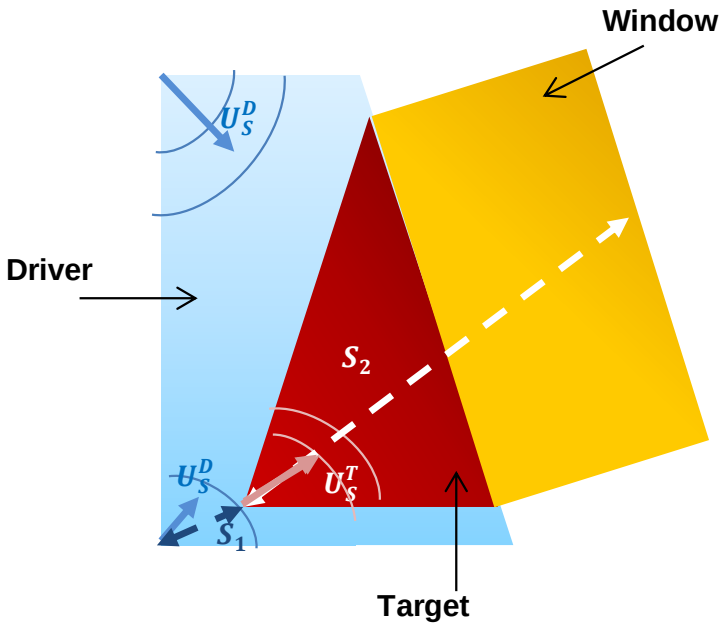

Figure 3.7: Edge waves propagating into the composite oblique wedge target after impact.

make sure that the time it takes for the edge waves to travel these distances, given by

$$\frac{S_1}{U_S^D} + \frac{S_2}{U_S^T}, \tag{3.4.4}$$

is greater than or equal to the time for the transmitted shear wave to arrive at the target-window interface, defined in Equation 3.4.3, plus the estimated extra microsecond for the shear wave response.

3.4.2 Impactor Thickness

The design of the impactor relies on the time that it takes for the entire shear response from the experiment to be collected. As a rule of thumb, this time must occur before the incident wave in the impactor reflects off its rear surface and travels back to the impactor-driver interface. Mathematically,

$$\frac{2D_I}{U_S^I} \geq t_4 + 1 \ \mu\text{sec}, \tag{3.4.5}$$

where D_I is the thickness of the impactor and U_S^I is the velocity of the shock generated upon impact in the impactor, found using impedance matching in Section 2.2.3.

3.4.3 Window Thickness

The final check is to make sure that the window is thick enough such that the information at the target-window interface is gathered before the transmitted shock hits the rear surface of the window. This calculation is made by using the velocity of the transmitted shock in the target and calculating how long it would take for it to travel from the target-window interface to the rear surface of the window; the time at which this wave arrives at the rear surface should occur after the shear response is found. These calculations are estimates and hence a starting point for the design, which can be refined by using numerical analysis.

3.5 Elastic Wave Simulations

To predict the magnitude of the shear response of the material in the oblique wedge design, one dimensional elastic wave simulations were implemented. These simulations used the theory presented in Section 2.1.2. Figure 2.4 has been overlaid onto the oblique wedge configuration in order to demonstrate how this theory has been applied. This is shown in Figure 3.8. In these simulations, the incident wave shown in Figure 3.8 is considered to be the incident wave in the driver material, the transmitted shock and shear waves correspond to the transmitted P and S waves, and the reflected shock and shear wave coincide with the reflected P and S waves in the elastic case. Equations 2.1.50 and 2.1.53 can be used to solve for the wave state. Prior to using these equations, some of the variables must be solved for in order to obtain an equivalent number of unknown variables and equations. In Figure 3.8, angle β is the angle of obliquity, or the angle of the incident wave with respect to the target, that allows for the normal $\underline{n_L^{A0}}$ to be found. The polarization vector $\underline{p_L^{A0}}$ is parallel to the normal for a longitudinal wave. Impedance matching can be used to find the particle velocity behind the incident shock; this is the magnitude of the velocity vector in Equation 2.1.50, α_{AL}^0. The elastic longitudinal wave velocity in Equation 2.1.54, c_1^A, is now set to the shock velocity of the incident wave, found using the linear $U_S - u_p$ relationship in Equation 2.2.7. This velocity can then be used to calculate the equivalent Láme constant, λ, which is assumed to change from the elastic value due to the shock wave. This constant is found from the definition of the longitudinal elastic wave velocity, giving

$$\lambda^A = \rho^A {c_1^A}^2 - 2\mu^A, \tag{3.5.1}$$

where c_1^A is now replaced with U_S^D, ρ^A is the initial density, and μ^A is the shear modulus of the

material.

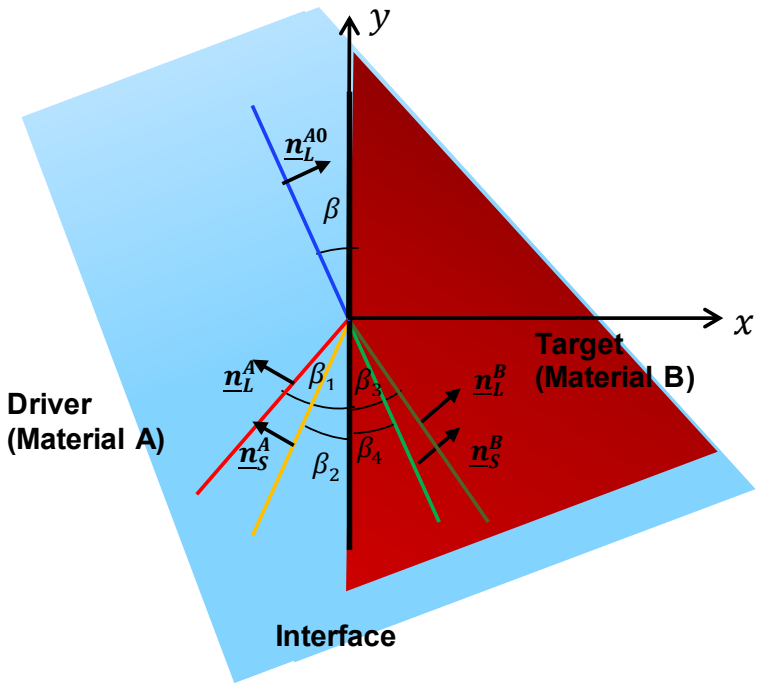

Figure 3.8: Elastic wave theory for oblique incident wave applied to oblique wedge configuration. The blue line represents the incident shock, the red is the reflected shock, the orange is the reflected shear wave, the dark green is the transmitted shock and the light green is the transmitted shear wave. $\underline{n}$ represents the normal to each wave and each β_i is the angle with respect to the interface.

The transmitted L wave in Figure 3.8 coincides with the transmitted shock wave, whose velocity is obtained using shock polar analysis in Section 2.2.4, and is used instead of the elastic longitudinal wave velocity c_1^B in Equation 2.1.54. Once again the Láme constant is found by using the definition of the wavespeed,

$$\lambda^B = \rho^B {c_1^B}^2 - 2\mu^B, \tag{3.5.2}$$

where $c_1^B = U_S^T$, ρ^B is the initial density, and μ^B is the shear modulus of the material. It is assumed that the reflected shock wave has the same velocity and angle of obliquity as the incident shock wave, in congruence with a true elastic model. The shear wave velocities are assumed to be the elastic values for the materials and the remaining angles of the waves with respect to the interface are found using Equation 2.1.54, from which the remaining normal and polarization vectors of each wave can be found. Incorporating this information, the only unknowns are the remaining particle velocity magnitudes in 2.1.50, which can be found by combining this with 2.1.53 to get 4 equations.

3.5.1 Applying Elastic Wave Theory

The premise behind using a pseudo-elastic wave theory approach for the oblique wedge configuration was to be able to predict the particle velocity behind the shear wave in the target such that experiments could be optimized without having to resort to time consuming numerical simulations. However, it was found that this approach essentially analyzed two hypothetical materials whose elastic properties matched the material properties after the shock wave propagated through them. For instance, for an oblique wedge configuration with a copper impactor, PMMA driver, and aluminum 6061-t6 target with a 10 degree angle for the incident wave and a 1000 m/s impact velocity, the calculated particle velocities after the transmitted longitudinal shock were

$$\underline{u_p^{BL}} = \alpha_{BL}\underline{p_L^B} = \begin{bmatrix} 385 \\ 106 \end{bmatrix} \text{ m/s}$$

and the predicted particle velocities after the transmitted shear wave were

$$\underline{u_p^{BS}} = \alpha_{BL}\underline{p_L^B} + \alpha_{BS}\underline{p_S^B} = \begin{bmatrix} 394 \\ 41 \end{bmatrix} \text{ m/s.}$$

To check if these one dimensional calculations matched with more detailed two dimensional numerical simulations, the program CTH was used – discussed in Section 3.6. Using material models and running the simulations showed that the velocities did not coincide. However, when a purely elastic approach was implemented using the Mie-Grüneisen equation of state for all of the materials with an elastic strength model, that implemented the modified Poisson's ratios after shock propagation for both the PMMA driver and aluminum target, the velocities agreed quite well with the elastic theory calculation. It should be noted here that the Poisson's ratios were calculated using the equation [12]

$$\nu = \frac{\lambda}{2\left(\lambda + \mu\right)}, \tag{3.5.3}$$

where the modified Láme constants found in 3.5.1 and 3.5.2 were used due to the parameter requirements for the elastic perfectly plastic strength model in CTH. This model requires a Poisson's ratio as well as a yield strength, the latter of which was set to 100 GPa such that the material did not yield.

Figure 3.9 shows the results of the CTH simulation. The timing of the particle velocities is not

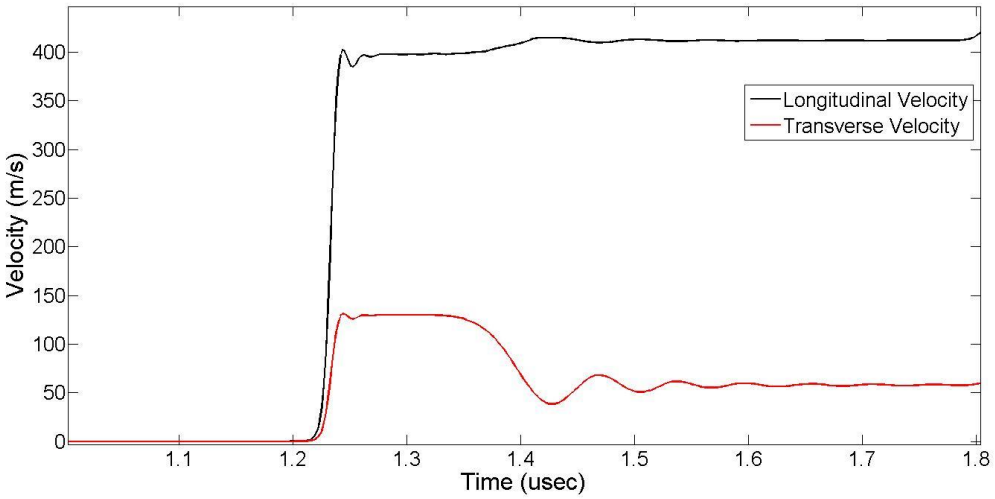

Figure 3.9: Particle velocities in target using elastic model for driver and target for oblique wedge configuration with copper impactor, polymethylmethacrylate driver, aluminum 6061-t6 target and lithium fluoride window for a 1000 m/s impact and 10 degree angle of obliquity.

of particular interest, but a tracer well into the target was chosen at which to find these velocities such that the separation between the longitudinal and shear waves could be studied. As can be seen, the longitudinal velocity here initially is 398 m/s and rises to 411 m/s, while the shear particle velocity starts out at 130 m/s and drops down to 59 m/s. Although these sets of velocities are not in exact agreement with velocities predicted in the elastic wave analysis, they are much closer to the 1D elastic predictions than the results found using actual material models, discussed in Section 3.6. What this result shows is that a numerical technique must be implemented that accounts for material strength to predict the shear response since the elastic wave analysis does not encompass the true nature of the experiment. Thus it can be concluded that when the target yields, the magnitude of the shear wave transmitted into the target can no longer be predicted. While shock polar analysis can be used to determine the longitudinal response, this wave analysis cannot be used to determine the shear wave magnitude.

3.6 CTH 2D Simulations

To have a better notion of the shear response of the material in the oblique wedge configuration, CTH hydrocode was used. CTH was developed by Sandia National Laboratories to model large deformation events and has the ability to analyze strong shock situations. It uses a two-step process to integrate the conservation equations starting with a Lagrangian step that allows the mesh to distort in order to follow material motion, followed by a remapping to the original mesh in the

Material	ρ_0 (g/cm^3)	C_0 $(J/Kg/K)$	S (km/s)	γ_0
Beryllium	1.850	7.92	1.124	1.19
Aluminum 6061-T6	2.703	5.22	1.37	1.97
Lithium Fluoride	2.638	5.15	1.35	1.69
Copper	8.930	3.94	1.489	1.99
Polymethylmethacrylate	1.186	2.30	1.75	1.91
Tantalum	16.654	3.39	1.22	1.60
Molybdenum	10.210	5.03	1.265	1.49
Sapphire	SESAME EOS			

Table 3.2: Equation of state parameters for materials used in the CTH simulations [73].

Eulerian frame. Although the simulation is mapped back into the original mesh, the code has the ability to update flow properties at given Lagrangian tracer locations [46].

3.6.1 Models

Two types of models used in CTH were the Equation of State (EOS) and the strength models. The EOS relates the pressure and internal energy, both thermodynamic quantities, to the density and temperature of a material. This type of model depicts the hydrodynamic response of the material. The main model used in these simulations was the Mie-Grüneisen model, discussed in Section 2.2.4, which uses shock Hugoniot data, found through experiments, to define an EOS. This is one of the most common models used in plate impact experiments. For the materials used in this research, the EOS was centered on the linear $U_S - u_p$ Hugoniot, the parameters of which are given in Table 3.2. The linear Hugoniot was used to define the shock pressure, $P^H(V)$, and internal energy, $E^H(V)$, in Equation 2.2.27, by

$$P_H = P_0 + \rho_0 U_S u_p \tag{3.6.1}$$

and

$$E_H = E_0 + 1/2 u_p^2, \tag{3.6.2}$$

which result from the shock jump equations of momentum and energy. The Grüneisen parameter in Equation 2.2.27 was assumed to be a function of volume, and the energy was given as a relation of a constant-volume specific heat, and temperature [55]. The only material whose EOS was not described by the Mie-Grüneisen model was Sapphire. For this material, a tabular form of the EOS given in the SESAME library was used.

The deviotoric response of the material is described by the strength models. Primarily, the Steinberg-Guinan-Lund Plasticity model was implemented for most of the materials for its ability to handle high pressures. However, for those materials that were outside the scope of this model – and in the case where the elastic response was required – a linearly elastic, perfectly plastic approach was used. The latter is based on the Von Mises yield surface. It uses the Von Mises yield criteria, defined in Equation 2.1.68, and the yield strength in simple tension, σ_Y^0, to test if the material is yielding. Prior to yield, stress can be related to strain by Equation 2.1.61. At yield, the material remains at the yield stress value. For the Steinberg-Guinan-Lund constitutive relation, which models a viscoplastic response, the expression for yield is strain-rate dependent and is given by

$$Y = \left[Y_T\left(\dot{\epsilon}, T\right) + Y_A f\left(\epsilon^p\right)\right] \frac{G\left(P,T\right)}{G_0}, \tag{3.6.3}$$

where Y_T, Y_A, f, and G are described by

$$\dot{\epsilon^p} = \left(\frac{1}{C_1} exp\left[\frac{2U_k}{T}\left(1 - \frac{Y_T}{Y_P}\right)^2 + \frac{C_2}{Y_T}\right]\right)^{-1}, \tag{3.6.4a}$$

$$Y_A f\left(\epsilon^p\right) = Y_A\left[1 + \beta\left(\epsilon_p + \epsilon_i\right)\right]^n \leq Y^*_{max}, \tag{3.6.4b}$$

and

$$G\left(P,T\right) = G_0\left[1 + A\frac{P}{\eta^{1/3}} - B\left(T - 0.02585eV\right)\right]. \tag{3.6.4c}$$

Here, Y_A is the yield strength at the Hugoniot Elastic Limit, Y_T is the thermally activated part of Y, Y^*_{max} is the work hardening maximum, G_0 is the initial shear modulus, C_1 is the exponential prefactor, C_2 is the coefficient of drag term, U_K is the activation energy, Y_P is the Peierls stress, n and β are work hardening parameters, A is the pressure dependence of the shear modulus and B is the temperature dependence of the shear modulus. These constants are all dependent on the material. ϵ^p is equivalent plastic strain, $\dot{\epsilon^p}$ is the equivalent plastic strain-rate, ϵ_i is the intial plastic strain, P is pressure, T is temperature, $\eta = \rho/\rho_0$ is compression, where ρ_0 is the initial density, and G is the bulk shear modulus [73]. To test for melting, the Lindemann law is used, where

$$T_m = T_{mo} exp\left[2a\left(1 - 1/\eta\right)\right] \eta^{2(\gamma_0 - a - 1/3)}. \tag{3.6.5}$$

Equation 3.6.5 is used to test for when temperature, T, exceeds T_m at which point Y and G are set

	Be	**Al**	**LiF**	**Cu**	**Ta**	**Mo**	**Sa**
$\rho_0(g/cm^3)$	1.85	2.703	2.638	8.930	16.690	10.200	–
$T_{mo}(eV)$	1.568e-1	1.051e-1	1.275e-1	1.542e-1	3.740 e-1	3.154e-1	–
a	1.0	1.5	1.4	1.5	1.3	1.3	–
γ_0	1.11	1.97	1.69	2.02	1.67	1.59	–
$A((dynes/cm^2)^{-1}$	1.54e-12	6.52e-12	5.0e-12	2.83e-12	1.45e-12	1.14e-12	–
$B(eV^{-1})$	2.994	7.149	7.172	4.375	1.509	1.764	–
n	7.8e-1	1.0e-1	0	4.5e-1	1.0e-1	1.0e-1	–
$C_1(sec^{-1})$	4.0e8	0	0	0	7.1e5	3.52e7	–
$C_2(dynes - sec/cm^2)$	1.2e5	0	0	0	1.2e5	1.2e4	–
$G_0(dynes/cm^2)$	1.51e12	2.76e11	4.9e11	4.77e11	6.9e11	1.25e12	–
β	2.6e1	1.25e2	0	3.6e1	1.0e1	1.0e1	–
ϵ_i	0	0	0	0	0	0	–
$Y_P(dynes/cm^2)$	3.0e9	0	0	0	8.2e9	1.67e10	–
$U_K(eV)$	3.1e-1	0	0	0	3.1e-1	3.72e-1	–
$Y^o_{max}(dynes/cm^2)$	1.31e10	0	0	0	4.5e9	1.6e10	–
$Y_A(dynes/cm^2)$	2.8e9	0	0	0	3.75e9	9.0e9	–
$Y_0(dynes/cm^2)$	3.3e9	2.9e9	3.6e9	1.2e9	7.7e9	1.6e10	3.55e9
$Y^*_{max}(dynes/cm^2)$	1.31e10	6.8e9	3.6e9	6.4e9	1.1e10	2.8e10	–
ν	0.18	0.33	0.25	0.333	0.3	0.375	0.28

Table 3.3: Strength parameters for materials used in the CTH simulations [73]. Materials are abbreviated as Be for beryllium, Al for aluminum 6061-t6, LiF for lithium fluoride, Cu for ohfc-copper, Ta for tantalum, Mo for molybdenum, and Sa for sapphire.

to zero. In this equation, T_{mo} is the melt temperature at constant volume, a is the coefficient of the volume dependence of the Grüneisen coefficent, and γ_0 is initial value of the Grüneisen coefficient. A summary of the parameters used for the materials in these simulations is given in Table 3.3 for both the Steinberg-Guinan-Lund and elastic perfectly plastic strength models. The only material in this table that uses the latter model is sapphire. It should be noted that PMMA, although not listed in Table 3.3, uses a viscoelastic-plastic model in CTH, the description of which is export controlled.

3.6.2 Slip at Material Interface

Since a shear wave is being transmitted into the specimen, slip can occur at the interface. CTH does not model slip and assumes materials are welded together at the interface, hence there is no easy way to accurately model this due to the inherent random nature of slip. Furthermore, samples are not perfectly flat in experiments as they are in CTH and often times two identical experiments can be conducted where one exhibits slip and the other does not. For this reason, experimentors will conduct the same experiment several times to determine if slip occurs.

3.6.3 Oblique Wedge Setup in CTH

After determining the appropriate materials to be used, the impact velocity and the angle of obliquity of the incident shock, the configuration was set up in CTH to be numerically analyzed. For ease of analysis, the configuration was first rotated in Matlab such that the rear surface of the target was parallel to the y-axis. This is shown in Figure 3.10. The reason for this was that the velocities obtained at the rear surface would coincide with those measured at the rear surface of the target in a given experiment. In other words, the transverse velocity would be along the y-axis and the longitudinal velocity would be perpendicular to the rear surface, along the x-axis in CTH.

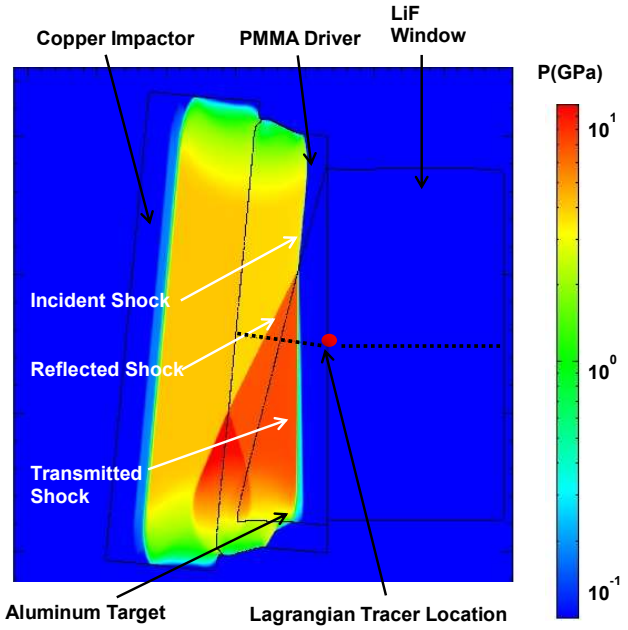

Figure 3.10: Two dimensional pressure plot for an oblique wedge configuration consisting of a copper impactor, polymethylmethacrylate (PMMA) driver, aluminum 6061-t6 (Al) target and lithium fluoride (LiF) window. Impact velocity is specified at 1000 m/s with a 10 degree angle of obliquity for the incident wave.

In Figure 3.10, a two dimensional pressure profile is shown to illustrate the wave state in the oblique wedge target. The incident, reflected and transmitted shocks can all be seen here, where the transmitted shock is parallel to the rear surface of the aluminum target. The Lagrangian tracer point shown in red is located at the aluminum-lithium fluoride interface and is the main point of interest since it demonstrates what would be measured in an experiment. Additional points are shown in the plot in the dotted black line and are used to study the wave propagation through the specimen. A two-dimensional rectangular mesh was used with Adaptive Mesh Refinement (AMR) in the target of interest in order to accurately depict what occurs in this region. A square mesh

was created throughout the entire problem ranging from 128 cells in the outer materials to 512 cells in the inner target. Convergence studies were performed on the mesh size to ensure that results remained consistent. Cell size was decreased until the stress and velocity outputs from the simulation no longer varied, at which point the largest possible cell size that produced no change in the results was chosen.

3.6.4 Progression of the Shear Wave

In these experiments, uniform loading is desired throughout the target. Furthermore, it is optimal to have the target respond to a maximum amount of shear stress in order to test its strength. To study if the shear wave is steady such that it has not dissipated once it propagates into the target, shear particle velocities throughout the target were plotted and are shown in Figure 3.11. The initial velocity is at a tracer point just after the driver-target interface and the final velocity profile is just before the target-window interface. The remainder of the velocity profiles, shown in a variety of different colors, are evenly distributed between these two points. In the first configuration, Figure 3.11a, the impactor and driver are beryllium (Be), the target is aluminum 6061-t6 (Al), the window is lithium fluoride (LiF), the impact velocity is 1000 m/s, and the angle of obliquity of the incident shock is 10 degrees. It can be seen that there is slight attenuation in velocity, although the profile remains similar throughout the specimen. The second configuration, shown in Figure 3.11b, consists of a copper (Cu) impactor, polymethylmethacrylate (PMMA) driver, an aluminum 6061-t6 target, a lithium fluoride window, has an impact velocity of 1000 m/s and an obliquity of 10 degrees. Here the wave is quite steady where the velocity profile remains constant throughout. Figure 3.11c shows the copper impactor, copper driver, tantalum (Ta) target, and lithium fluoride window configuration. In this setup, it is evident that there is some attenuation. In this case, the impact velocity was 1300 m/s with an angle of obliquity of 10 degrees. Closer to the target-window interface, reflections can be seen that appear to increase the velocity profile. The velocities at the last two tracers must experience edge effects since the velocity decreases rather than increases upon reflections from the window. The final configuration in Figure 3.11d is the molybdenum (Mo) impactor, molybdenum driver, tantalum target, and sapphire window with a 1000 m/s impact velocity and a 10 degree angle of obliquity. Here the velocity has some oscillation which could be due to the artificial viscosity in CTH. There is definitely some attenuation here of the wave as well as the effects of the reflected wave off of the window.

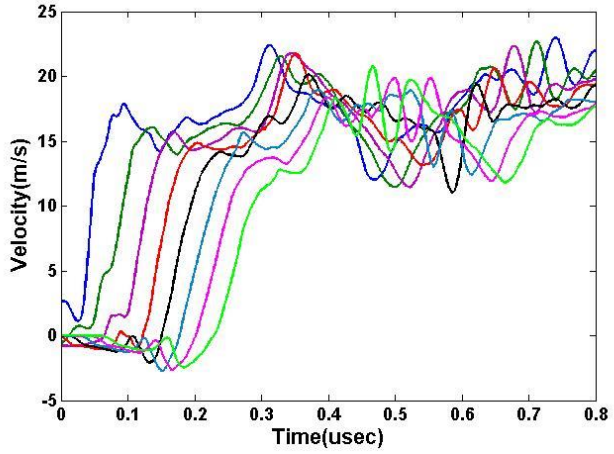

(a) Be Be Al LiF

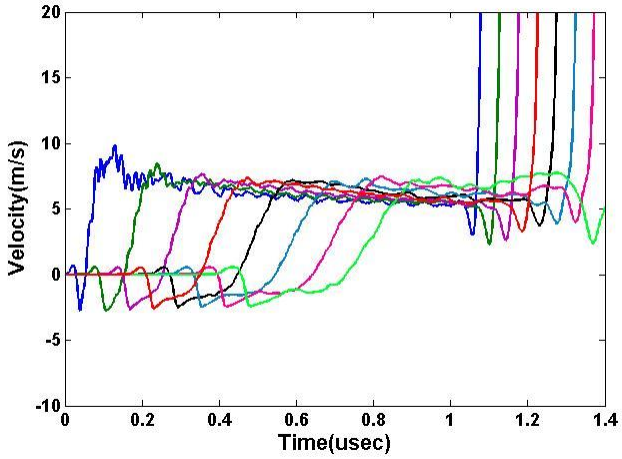

(b) Cu PMMA Al LiF

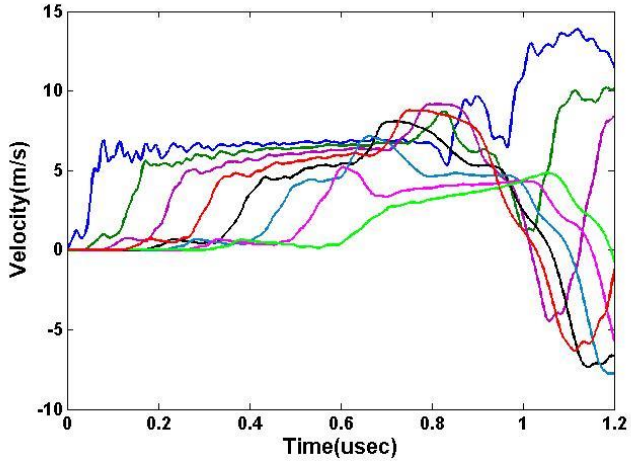

(c) Cu Cu Ta LiF

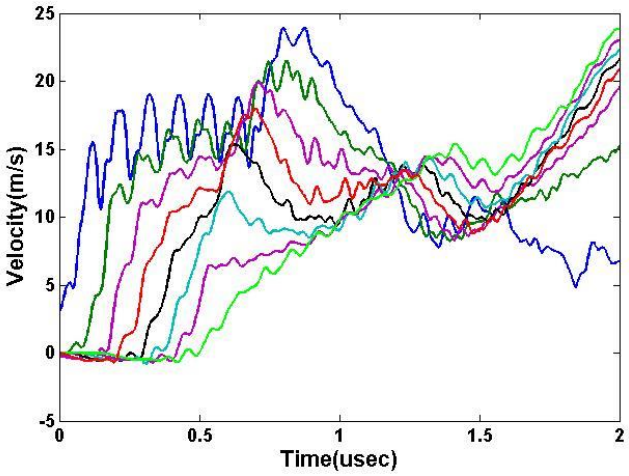

(d) Mo Mo Ta Sa

Figure 3.11: Progression of shear particle velocity within oblique wedge targets for four configurations. Initial velocity is at the tracer just within the target after the driver-target interface and the final velocity is at the tracer just within the target before the target-window interface; the remainder of the velocities are evenly distributed between these two points. The names of each simulation are abbreviated for impactor, driver, target, and window; i.e., for Be Be Al LiF, the impactor and driver are beryllium, the target is aluminum 6061-t6 and the window is lithium fluoride.

3.6.5 Strain-Rate Analysis

In order to calculate the strain-rate at which these simulations occur, Equation 2.1.19 can be used. Assuming that the problem is one dimensional in strain, this reduces to

$$\frac{\partial \epsilon}{\partial t} = \frac{\partial v}{\partial x}. \tag{3.6.6}$$

The difference of the output of the particle velocity in the x direction between two adjacent tracers

and their distance from one another can be used to find the strain-rate for each point in time. This calculation, performed at a tracer point just inside the target at the target-window interface for the four main configurations discussed above, is shown in Figure 3.12. As can be seen, the peak strain rates are 4.8x10^6/s for the Be Be Al LiF configuration, 4.1x10^6/s for the Cu PMMA Al LiF configuration, 2.3x10^6/s for the Cu Cu Ta LiF configuration, and 2.3x10^6/s for the Mo Mo Ta Sa configuration. The peak strain-rates occur at different times due to the geometry of each composite target.

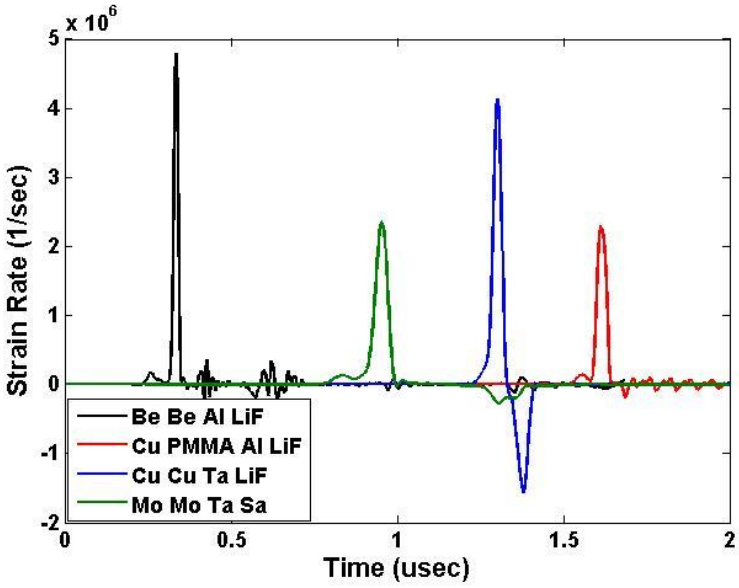

Figure 3.12: Strain-rate at target-window interface for four oblique wedge configurations. The first configuration is the beryllium impactor, beryllium driver, aluminum 6061-t6 target and lithium fluoride window with a 1000 m/s impact velocity. The second configuration is the copper impactor, polymethylmethacrylate driver, aluminum 6061-t6 target and lithium fluoride window with a 1000 m/s impact velocity. The third configuration is the copper impactor, copper driver, tantalum target and lithium fluoride window with a 1300 m/s impact velocity. The last configuration consists of a molybdenum impactor and driver, a tantalum target and a sapphire window for a 1000 m/s impact velocity. All of these configurations assumed a 10 degree angle of obliquity.

3.6.6 Stress Calculation

As previously mentioned, particle velocities at the rear surface of the target can be used to calculate the longitudinal and shear stresses. These were found in the simulation using the velocity outputs at the rear surface Lagrangian tracer, shown in Figure 3.13. It can be seen in Figure 3.13 that the shear wave arrives later in time than the longitudinal shock, as expected. Times t_L and t_S indicate the time of arrival at the rear surface of the target-window interface. By shifting the time scale so that time zero indicates arrival at the front surface of the wedge target, the arrival at the

rear surface of each wave can be used to find the time it takes each wave to propagate and hence the shock and shear wave velocities can be found, where these velocities are respectively defined as

$$U_S^T = \frac{d_T}{t_L} \tag{3.6.7a}$$

and

$$C_S = \frac{d_T}{t_S}. \tag{3.6.7b}$$

The distance d_T is measured halfway up the target. It must be noted that, although the shear wave comes in at an angle with respect to the rear surface of the target, the effect of this on the observed wave velocity is negligible. Using the initial density – since velocity is measured in the Lagrangian frame – as well as the wave velocities and particle velocities, v_p and u_p, the shear and longitudinal stresses are calculated from Equations 3.1.1 and 3.1.2.

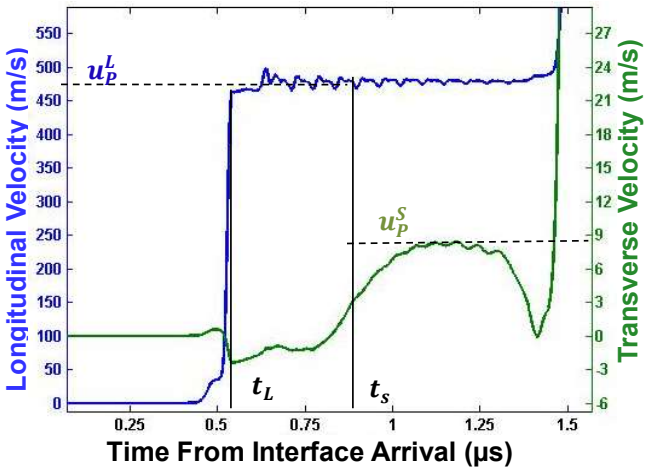

Figure 3.13: Longitudinal and shear velocity profiles at the rear surface of an oblique wedge target. Time is shifted such that time zero indicates shock arrival at the front surface of the target. u_p^L is the longitudinal particle velocity, u_p^S is the shear particle velocity, and t_L and t_S are the arrivals of the longitudinal and shear waves at the rear surface of the wedge target, respectively.

3.6.7 Comparison of Stresses vs. Yield

The process described above for stress calculation was repeated for a variety of different configurations. The four that are highlighted here correspond to the targets described above in the analysis to find if the shear wave was steady. The first configuration is Be Be Al LiF and is the theoretical

configuration proposed by Justin Brown in his Ph.D. thesis [13]. This theoretical case led to the study of this target design specifically because its shear stress matched closely to the maximum shear stress in the material, which could then be used to calculate strength. The impact velocity in this simulation was 1000 m/s, with an angle of obliquity of 10 degrees and resulted in a transmitted wave angle of 6.96 degrees with respect to the front edge of the target. The second design from above for Cu PMMA Al LiF resulted in a transmitted wave angle of 5.33 degrees. The Cu Cu Ta LiF configuration resulted in a 8.2 degree transmitted wave angle and the Mo Mo Ta Sa configuration resulted in a 7.0 degree transmitted wave angle. The windows were chosen to be as closely matched in impedance to the target as possible to mitigate angled reflections at the target-window interface for all but the Cu Cu Ta LiF. LiF was chosen here to test whether reflections off of its surface would result in a larger change in particle velocity. It was thought that it would be easier to determine variations in these velocities as oppposed to those resulting from reflections off the sapphire.

Since the strength of the material is of interest, the maximum stress was compared to the calculated shear stress to see if the shear stress reached in the experiment could be used to find the strength of the material. To calculate the maximum stress, the Von Mises yield criteria was used, giving

$$\tau_{max} = \frac{\sigma_Y^0}{\sqrt{3}}, \tag{3.6.8}$$

where σ_Y^0 is the yield strength and is a material property. To find out whether the material yields, Equation 2.1.68 can be used. The stresses used in these equations were found from the Lagrangian tracer point output in CTH and results of this analysis are shown in Figure 3.14.

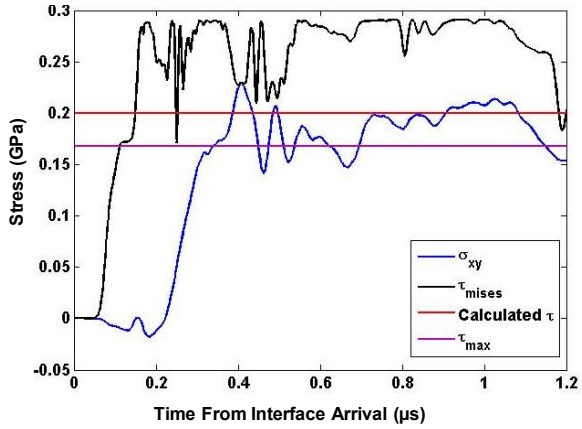

(a) Be Be Al LiF

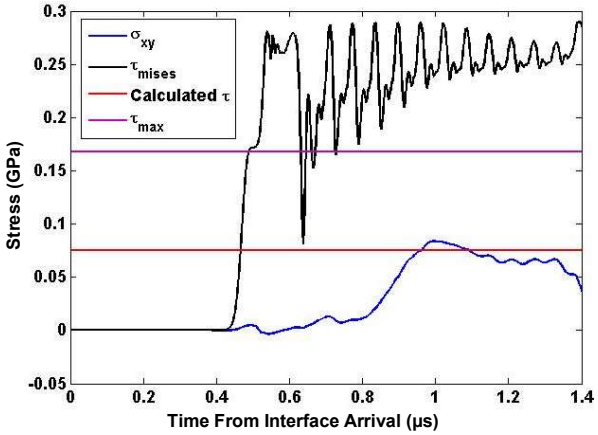

(b) Cu PMMA Al LiF

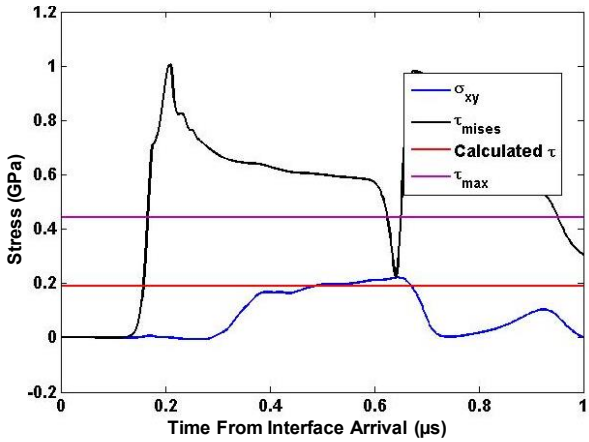

(c) Cu Cu Ta LiF

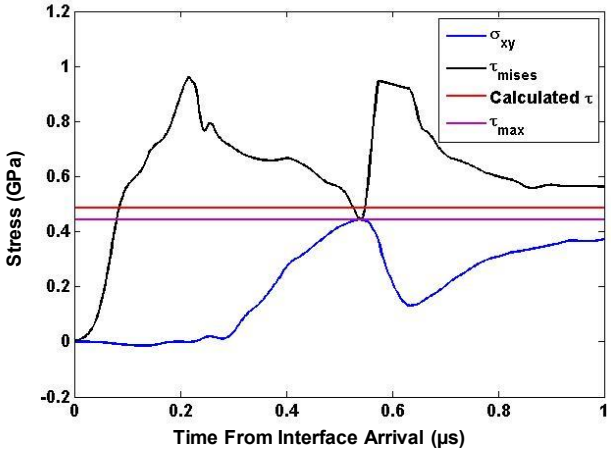

(d) Mo Mo Ta Sa

Figure 3.14: Shear stress, shear stress using Mises Yield criteria, calculated shear stress from transverse particle velocity and maximum shear stress for four oblique wedge configurations. Calculations were performed from CTH simulation results.

In Figure 3.14a, the theoretical case is shown – since beryllium is toxic and not well suited for a lab environment it is only a theoretical study here. In this figure, the shear stress, shown in blue from the stress tensor output, matches quite well with the shear stress calculated using the transverse particle velocity – 0.199 GPa for the calculated shear stress and 0.189 GPa for the average shear stress in the peak region. It is also close to the results using the Von Mises yield criteria, shown in black, the average of which is 0.27 GPa. The next two configurations, however, differ quite significantly from the Mises criteria value. Again, the calculated shear stress matches well for the Cu PMMA Al LiF in 3.14b, Cu Cu Ta LiF in 3.14c, and the Mo Mo Cu Sa in 3.14d, composite targets with 0.07 GPa vs. 0.075 GPa, 0.198 GPa vs. 0.189 GPa, and 0.428 GPa vs. 0.486 GPa, respectively, for the average shear stress from the tensor output vs. the calculated shear stress. The

Configuration	**Impact Velocity** (m/s)	**Angle of Obliquity** (deg)	**Transmitted Shock Wave Angle** (deg)	**Shear Stress CTH Output** (GPa)	**Calculated Shear Stress** (GPa)	**Mises Shear Stress** (GPa)	**Maximum Shear Stress** (GPa)
Be Be Al LiF	1000	10	6.96	0.189	0.199	0.270	0.167
Cu PMMA Al LiF	1000	10	5.33	0.070	0.075	0.255	0.167
Cu Cu Ta LiF	1300	10	8.2	0.198	0.189	0.614	0.444
Mo Mo Ta Sa	1000	10	7.0	0.428	0.486	0.960	0.444

Table 3.4: Summary of four oblique wedge configurations. Impact velocity and angle of obliquity were independent variables, while the transmitted shock wave angle was calculated using shock polar analysis. "Shear stress CTH output" is the mean shear stress at the peak region at the rear surface of the target. "Calculated shear stress" was found using the transverse velocity. "Mises shear stress" was found using the Von Mises yield criteria."Maximum shear stress" is the yield stress in simple tension divided by the square root of three, a material property.

Mises shear stress, however, is much higher for each of these configurations – 0.255 GPa, 0.614 GPa and 0.960 GPa, respectively. It should be noted here that the shear stress analyses for the Cu Cu Ta LiF and Mo Mo Ta Sa configurations were made at a Lagrangian tracer point midway into the target. The reason for this was the attenuation of the velocity profile further into the target and the reflections off of the windows, as described in Section 3.6.4. If these particular configurations were of interest in an experiment, it would be prudent to design a target larger in diameter to avoid any edge effects that could be causing the attenuation. These results are summarized in Table 3.4.

In all four cases, the target has yielded since the Mises stress that is calculated exceeds the maximum shear stress for each material. What this indicates is that, although the material is yielding, it is not yielding from pure shear, otherwise the shear stress would match or exceed the maximum shear stress value. For the Be Be Al LiF and Mo Mo Ta Sa cases, the shear stress is close to the maximum value. These could be slightly off due to yielding caused by the other stress components. Since the Mises stress is higher in all of the cases than the maximum shear stress, the yield surface must be analyzed to determine the mechanism causing yield to occur.

3.6.8 Yield Surface and Stress Path

The yield surface can be found using Equation 2.1.68 to further elucidate the yielding process in the oblique wedge setup. The analysis can be simplified assuming a 1D strain state as defined in Section 2.1.3.2, and superimposing a shear stress, resulting in the tensor

$$\boldsymbol{\sigma} = \begin{bmatrix} \sigma_{xx} & \sigma_{xy} & 0 \\ \sigma_{xy} & \sigma_{yy} & 0 \\ 0 & 0 & \sigma_{yy} \end{bmatrix}. \tag{3.6.9}$$

Applying 2.1.69 and substituting this into Equation 2.1.68 results in an equation for the shear stress as a function of the longitudinal, lateral, and yield stresses given by

$$\sigma_{xy} = \sqrt{\frac{{\sigma_Y^0}^2 - (\sigma_{xx} - \sigma_{yy})^2}{3}}. \tag{3.6.10}$$

This equation is the yield surface and allows for the stress path followed by the target material to be found by plotting σ_{xy} as a function of $\sqrt{\frac{(\sigma_{xx}-\sigma_{yy})^2}{3}}$ from the stress tensor output in CTH. The stress path as compared to the yield surface is shown for each of the configurations in Figures 3.15a-3.15d.

In Figure 3.15a the aluminum target in the Be Be Al LiF configuration first follows the yield surface and then exceeds it, ending up in a state of mostly shear, rather than the longitudinal and lateral stresses. Here, initial yield in simple tension is analyzed and since the stress path exceeds the surface, this result could indicate that the yield stress is strain-rate and pressure dependent, changing throughout the experiment, which results in a new yield surface. Nevertheless, since the material ends up in a state of pure shear, the measured transverse velocity can be used to calculate the shear stress and the yield strength thereafter. On the contrary, Figure 3.15b, the Cu PMMA Al LiF configuration, shows that the stress path follows the yield surface and is yielding, but it is not in pure shear at the end of the experiment. The same is true for the Cu Cu Ta LiF configuration in Figure 3.15c. Although in this case the stress path is not quite on the yield surface, it is evident in Figure 3.14c that it is yielding. The reason the stress path is off the yield surface could be due to the assumption of 1D strain with superimposed shear. In this assumption, σ_{yy} and σ_{zz} were assumed to be equal. Thus, σ_{zz} could be separately contributing to the yielding of the material. The final case in Figure 3.15d for the Mo Mo Ta Sa composite target indicates that the stress path follows the yield surface closely and ultimately ends up near the maximum value of shear stress, much like the Be Be Al LiF case. Overall, the four configurations have the ability to measure the shear stress, but not necessarily the strength, although this is promising with the Mo Mo Ta Sa composite target.

3.6.9 Higher Impact Velocities

At higher velocities it appears that the assumption of a constant shear wavespeed breaks down and thus the arrival time can not be used to calculate the shear wave velocity for the entire exper-

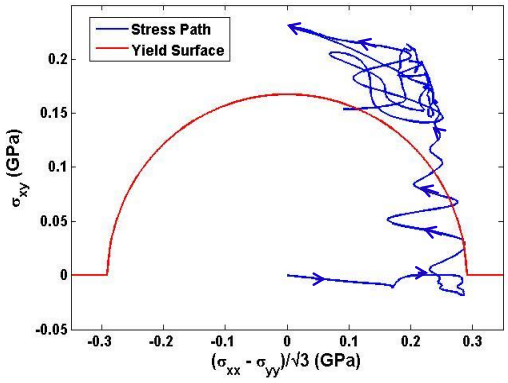

(a) Be Be Al LiF

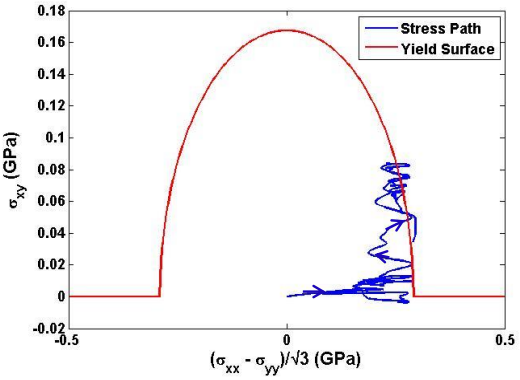

(b) Cu PMMA Al LiF

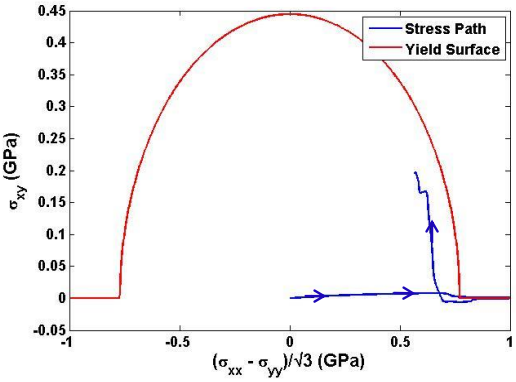

(c) Cu Cu Ta LiF

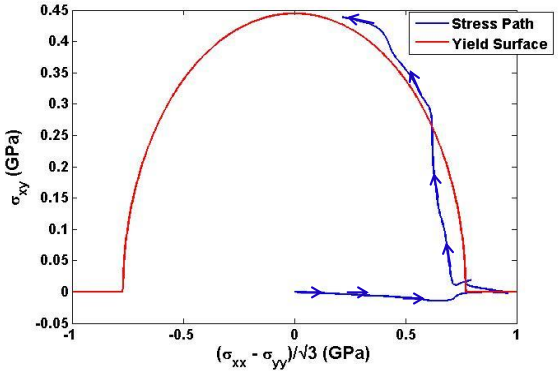

(d) Mo Mo Ta Sa

Figure 3.15: Stress path and yield surface calculations for four oblique wedge configurations The names of the configurations have been abbreviated as impactor, driver, target, and window.

iment. This is apparent in a higher velocity impact of the Cu PMMA Al LiF configuration, the results of which are shown in Figure 3.16. Note that, the region where the shear wave propagates in the target prior to reflection is in the first peak of the shear stress from the stress tensor. As can be seen, the target is yielding since the Mises criteria is much higher than the maximum shear stress. While the calculated shear – 0.145 GPa – is relatively close to the maximum value – 0.167 GPa – it is still quite a bit higher than the shear stress from the tensor, the average peak value of which is 0.107 GPa. The reason that the calculated value is higher than the actual shear stress value is attributed to the fact that shear wave velocity is assumed to be a constant value, when in reality it depends on the shear modulus which could be significantly different at higher pressures in comparison to the nominal value for the material.

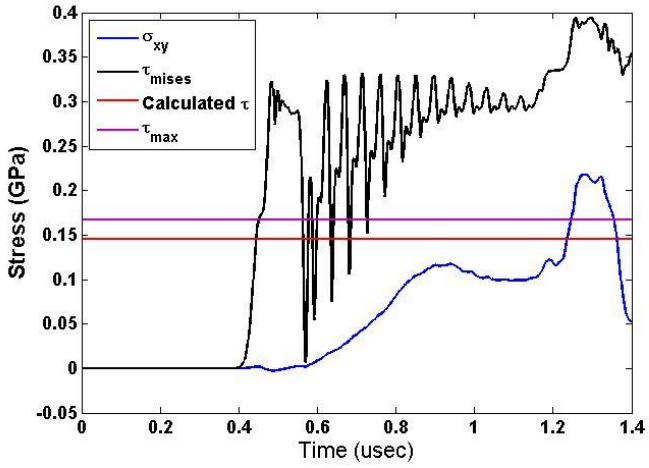

Figure 3.16: Shear stress, shear stress using Von Mises yield criteria, calculated shear stress from transverse particle velocity and maximum shear stress for the Cu PMMA Al LiF configuration at 1300m/s impact. Calculations were made from simulations in CTH hydrocode.

3.6.10 Impedance Matching to find In-Situ Velocities

Another concern with the oblique wedge design is that measurements are being made through a window. Though this is generally not a problem for planar shocks, it becomes an issue when the transmitted waves are not parallel to the rear surface. Specifically, this is a concern for the transverse velocity measurement since the shear wave is not parallel to the longitudinal shock and thus reflects off of the target-window interface at an angle. Figure 3.17 shows an x-t diagram for the waves propagating into the window.

In Figure 3.17 the target and window are assumed to be in a quiescent state – zero pressure and velocity. After the longitudinal wave propagates into the target, the state contains a longitudinal

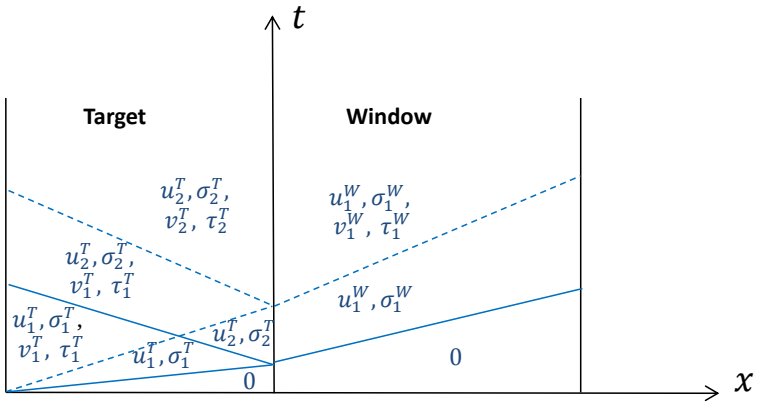

Figure 3.17: x-t diagram for the target and window in an oblique wedge configuration.

velocity u_1^T and stress σ_1^T. This is simplified since this state involves a three dimensional stress tensor in reality, however, a hydrostatic pressure prior to shear wave arrival may be assumed. Following this state, the shear wave arrives in the target and superimposes a transverse velocity v_1^T and stress τ_1^T. Some portion of the longitudinal wave reflects off the window and the rest transmits into it. Assuming continuity of stresses and particle velocities at the target-window interface, the state in the window, with velocity u_1^W and stress σ_1^W, is set equal to state u_2^T and σ_2^T in the target. Finally, the shear wave reaches the window and the state is superimposed with shear velocity and stress of v_1^W and τ_1^W, respectively, which is equal to state v_2^T and τ_2^T in the target . Equations 2.2.5 and 2.2.8 can be used to relate velocities measured in the window to the in-situ velocities in the target. Applying these equations for the longitudinal direction in the window and target results in

$$\sigma_1^W - \sigma_0^W = \rho_0^W U_S^W \left(u_1^W - u_0^W\right), \tag{3.6.11a}$$

$$\sigma_1^T - \sigma_0^T = \rho_0^T U_S^T \left(u_1^T - u_0^T\right), \tag{3.6.11b}$$

and

$$\sigma_2^T - \sigma_1^T = -\rho_0^T U_S^T \left(u_2^T - u_1^T\right), \tag{3.6.11c}$$

where Equation 3.6.11c incorporates the fact that the reflected wave travels in the negative direction with respect to the coordinate system. Since the transmitted shock wave enters a quiescent state, it can be assumed that $u_0^T = \sigma_0^T = 0$. The window is also initially at rest so $u_0^W = \sigma_0^W = 0$.

Applying continuity of tractions and velocities at the interface, results in $u_1^W = u_2^T = u_p^1$, $u_1^T = u_p^0$, and $\sigma_2^T = \sigma_1^W$. Substituting in these assumptions and combining Equations 3.6.11a-3.6.11c, an expression for the in-situ particle velocity is found:

$$u_p^0 = \frac{\left(\rho_0^W U_S^W + \rho_0^T U_S^T\right) u_p^1}{2\rho_0^T U_S^T}. \tag{3.6.12}$$

Here u_p^1 is the measured velocity, ρ_0^W and ρ_0^T are known values, and U_S^T can be measured based on the arrival of the shock and the thickness of the target. The shock velocity in the window, U_S^W, can be found from Equation 2.2.7 using the measured particle velocity, u_p^1. The same approach can be applied to the transverse direction to get the relation for the in-situ shear velocity:

$$v_p^0 = \frac{\left(\rho_0^W C_S^W + \rho_0^T C_S^T\right) v_p^1}{2\rho_0^T C_S^T}, \tag{3.6.13}$$

where v_p^1 is the measured shear particle velocity, C_S^W is assumed to be the elastic value for the shear wavespeed in the window, and C_S^T is measured based on arrival of the shear wave and the thickness of the target.

For the case of an aluminum target with a lithium fluoride window, the two materials are so well matched that this approach seems to work well. Figures 3.18a and 3.18b show the velocities measured in the window, the calculated in-situ velocity and the actual in-situ velocity from the simulation described above for the Cu PMMA Al LiF configuration with a 10 degree angle of obliquity and 1000 m/s impact. The window and calculated in-situ velocities appear time shifted due to the fact that they occur later since they are from the tracer in the window rather than the target. From Figures 3.18a and 3.18b, it appears that it is not necessary to use impedance matching to find the in-situ velocities. Furthermore, the longitudinal velocity in the window is actually slightly closer to the in-situ velocity than the calculated velocity.

This approach can also be applied to the Cu Cu Ta LiF configuration with the 10 degree angle of obliquity and 1000 m/s impact, where Ta and LiF are not well matched. These results are shown in Figure 3.19. In Figure 3.19a, it does appear that Equation 3.6.12 estimates the longitudinal in-situ velocity quite well from the window measurement. Nevertheless, 3.19b shows that the transverse velocity is not well matched. The simulation was repeated for a larger target and it was found that the peak in-situ velocity for no attenuation was 9.2 m/s rather than 8.7 m/s in the attenuated case and, while the non attenuated velocity was higher, performing impedance matching on the velocity measured at the target-window interface still yielded similar results to Figure 3.19b . Upon

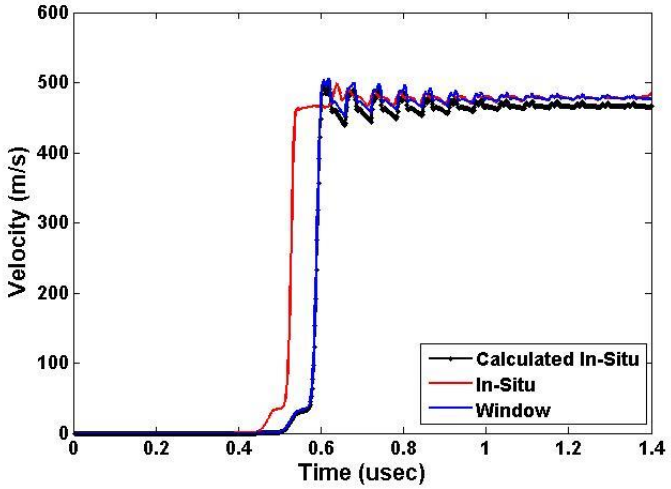

(a) Longitudinal Particle Velocities

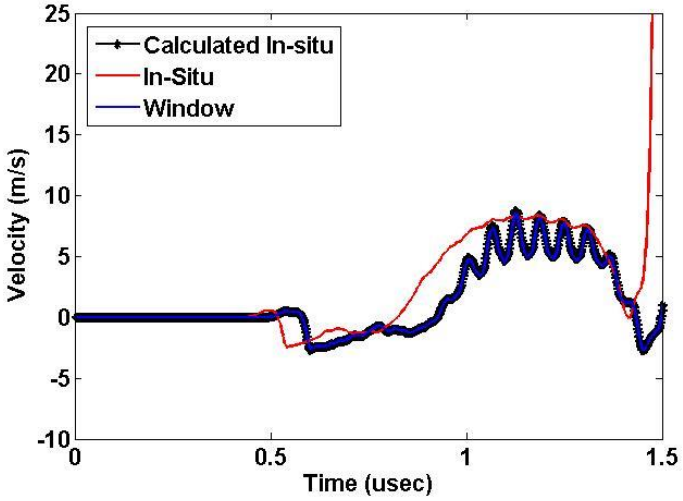

(b) Shear Particle Velocities

Figure 3.18: Longitudinal and transverse velocity profiles for Cu PMMA Al LiF oblique wedge configuration including velocities in the window, in-situ velocities in the target and calculated in-situ velocities from the window measurement. Calculations made using numerical simulations in CTH hydrocode.

further investigation, it was concluded that this result is not due to the attenuation of the wave but rather the inability of the impedance matching technique to capture the in-situ shear velocity for the oblique wedge setup. Another concern is that the window could also be yielding, which would mean that the maximum shear from target is not being transferred into the window and thus the shear measured through the window would relate more to the window response rather than the target response to the shear wave. It was concluded that a different approach would need to be used to obtain in-situ measurements.

3.6.11 Oblique Wedge Configuration Using Anvil Backing

As a solution to some of the issues exhibited with the rear surface window approach, an anvil can be used instead. The case of Mo Mo Ta Sa, described in Section 3.6.7, was re-examined to determine if sapphire was yielding. Equation 3.6.8 was used to determine the maximum shear stress the window would support, where σ_Y^0 was stored in CTH as 0.355 GPa, and Equation 2.1.68 was implemented to see if the window yielded. Figure 3.20 shows that the window does in fact yield. In this case, the window was modeled as elastic perfectly plastic and thus the stress does not exceed yield value, however, it does reach it which indicates that the material is yielding.

As mentioned in Section 3.6.10, the window yielding would not allow the maximum shear stress in the target to be transmitted and since this is the case here, an alternative technique must be approached. This new technique would also mitigate concerns in finding the in-situ velocities in the target since it was shown above that angled reflections at the target-window interface cause issues. Since the Mo Mo Ta Sa design exhibited a shear stress that was close to the maximum value, this oblique wedge design was used with the sapphire replaced by tungsten carbide (WC). WC was used because it has a higher strength than Ta — with initial yield strength $\sigma_Y^0 = 4.46$GPa for the WC and $\sigma_Y^0 = 0.77$GPa for the Ta [73] — and hence should allow for all of the shear stress from the Tantalum to be transmitted into it.

The goal of this new model would be to create an experiment that would allow for the in-situ measurement to be determined. To do this, a similar technique to that used in the elastic wave simulations, Section 3.5, was implemented. In Figure 3.21, the wave state is shown. Here it has been assumed that the incident shock wave is nominally parallel to the rear surface of the target and hence only causes longitudinal reflected and transmitted waves. Although the incident shear wave is not parallel to the rear surface, it is assumed that it is not a shock and hence any longitudinal reflected and transmitted waves due to the oblique shear waves will not have much effect on the

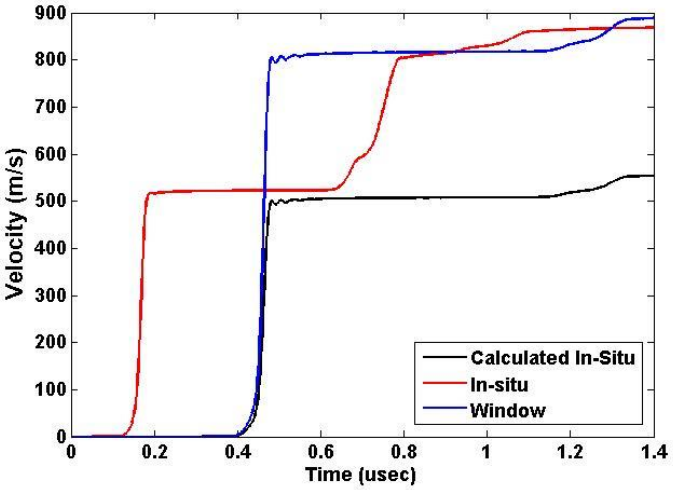

(a) Longitudinal Particle Velocities

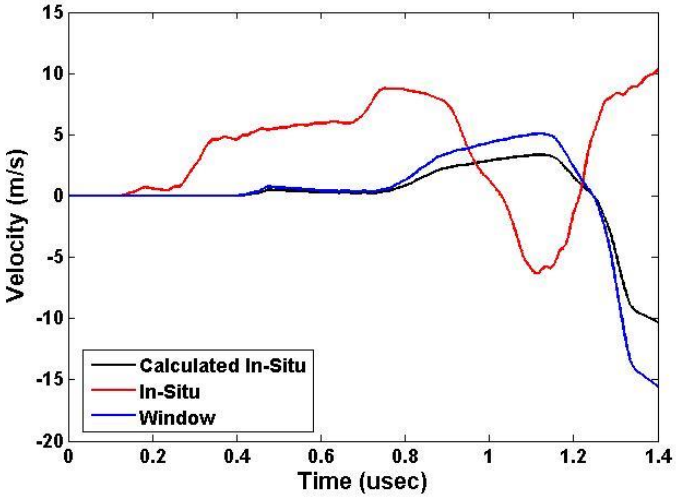

(b) Shear Particle Velocities

Figure 3.19: Longitudinal and transverse velocity profiles for Cu Cu Ta LiF oblique wedge configuration from CTH simulation including velocities in window, in-situ velocities in target and calculated in-situ velocities from window measurement.

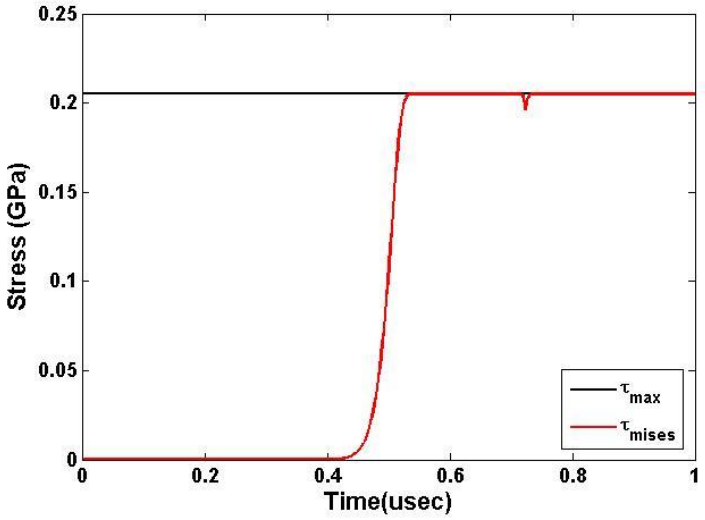

Figure 3.20: Maximum shear stress and Mises shear stress for oblique wedge configuration of Mo Mo Ta Sa using a CTH simulation.

state after the shock. Hence, transverse reflected and transmitted waves from the incident shear wave are only considered. These two assumptions simplify the problem. In Figure 3.21, angles β_{0L} and β_{0S} are the angles of the incident waves with respect to the target-anvil interface, where β_{0L} is assumed to be zero. β_{0S} is found using geometry and is given by the difference between the angle of the shear wave with respect to the driver-target interface and the angle of the target, the former of which is found from Equation 3.2.1. The wavespeeds in the target, c_{1A} and c_{2A}, are found by using the shock and shear wave arrival times at the rear surface of the target and the thickness of the target midway up. In an actual experiment, the arrival time at the rear surface of the target would need to be measured by using a technique such as VISAR probes, tilt pins, etc., outside the anvil diameter, but within the target diameter. To find the time that the shock traveled in the target, one would need to subtract travel time in the driver, which could be found by either finding travel time in a second experiment with just the flyer and driver or by using the Hugoniot of the driver. For higher impact velocities where the shear wave velocity is not a constant, either the elastic value can be used or the calculation with the arrival time can be used as an estimate. It can also be shown that the shear strain resulting from the transverse wave is quite low and hence it can be assumed that the wave travels at its elastic wavespeed. To show this, Equation 2.1.61 can be used to find the shear strain as a function of shear stress in the target, given by

$$\epsilon_{12} = \frac{\sigma_{12}}{2\mu}, \tag{3.6.14}$$

where μ is the shear modulus and can be found from the definition of the transverse wavespeed resulting in the equation

$$\mu = {c_2}^2 \rho. \tag{3.6.15}$$

Using the results in Table 3.4 for the calculated shear stress in each of the four configurations previously studied along with the wavespeeds and densities for both 6061 T6 Aluminum and Tantalum, it is found that the strain is 0.0037, 0.0014, 0.0013, and 0.0033 for the Be Be Al LiF, Cu PMMA Al LiF, Cu Cu Ta LiF, and Mo Mo Ta Sa configurations, respectively. The wavespeeds used were 3.15 km/s for the Al and 2.09 km/s for the Ta and the respective densities were 2.703 g/cm^3 and 16.656 g/cm^3 [60]. For further accuracy, simulations must be studied. Whichever method is used to find the wavespeeds, they can be used to calculate the equivalent Láme constant, λ, and shear modulus, μ, where

$$\lambda^A = \rho^A {c_1^A}^2 - 2\mu^A, \tag{3.6.16}$$

as in Equation 3.5.1 and the shear modulus is given by

$$\mu^A = {c_2^A}^2 \rho^A. \tag{3.6.17}$$

In these equations, the definitions of the wavespeeds have once again been used. It is assumed that the anvil is elastic and hence its defined material properties can be implemented. For tungsten carbide, $\rho^B = 15.4$ g/cm^3, $c_{2B} = 4.3$ km/s, and $c_{1B} = 6.858$ km/s [37]. From these values, the shear modulus and Láme constant can be found. As mentioned, the incident longitudinal wave angle was assumed to be parallel to the rear surface of the target meaning that $\beta_1 = \beta_3 = 0$. Then, using Equation 2.1.54, the remaining angles were found to be $\beta_2 = \beta_{0S}$ and $\beta_4 = sin^{-1}\left(\frac{c_{2B} sin\beta_{0S}}{c_{2A}}\right)$. From these angles, the normal and polarization vectors can be calculated.

To find the in-situ velocities in the target using the information from the target-anvil interface, continuity of velocities and tractions at the interface are applied. An approach similar to Equation 2.1.50 is used to obtain the continuity of velocity equation,

$$\alpha^0_{AL}\underline{p_L^{A0}} + \alpha^0_{AS}\underline{p_S^{A0}} + \alpha_{AL}\underline{p_L^A} + \alpha_{AS}\underline{p_S^A} = \alpha_{BL}\underline{p_L^B} + \alpha_{BS}\underline{p_S^B}. \tag{3.6.18}$$

Using Equations 2.1.51 and 2.1.52 at the target-anvil interface yields the continuity of traction

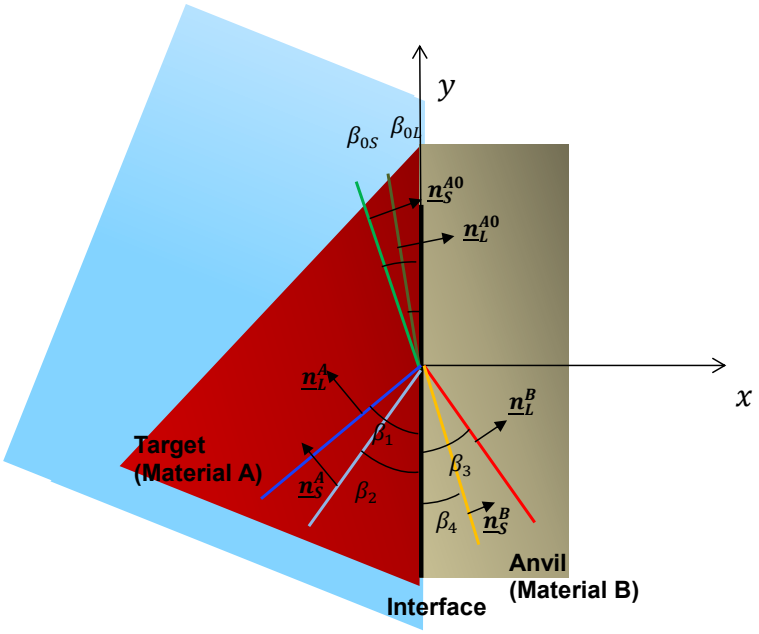

Figure 3.21: Wave state at target-anvil interface upon incidence of the shock and shear wave. The dark green line represents the incident shock, the light green is the incident shear wave, the dark blue line is the reflected shock, the light blue is the reflected shear wave, the red is the transmitted shock and the orange is the transmitted shear wave. β_i is the angle with respect to the interface for each wave and $\underline{n}$ is the normal for each wave, where the subscripts S and L refer to the shear and longitudinal waves, respectively, and the superscripts refer to material A or B. The superscript A0 refers to an incident wave.

relation

$$\left(\frac{1}{c_1^A}\mathbf{B_1C^AB^T_{AL0}}\right)\alpha^0_{AL}\underline{p_L^{A0}} + \left(\frac{1}{c_2^A}\mathbf{B_1C^AB^T_{AS0}}\right)\alpha^0_{AS}\underline{p_S^{A0}} + \left(\frac{1}{c_1^A}\mathbf{B_1C^AB^T_{AL}}\right)\alpha_{AL}\underline{p_L^A} + \left(\frac{1}{c_2^A}\mathbf{B_1C^AB^T_{AS}}\right)\alpha_{AS}\underline{p_S^A} = \left(\frac{1}{c_1^B}\mathbf{B_1C^BB^T_{BL}}\right)\alpha_{BL}\underline{p_L^B} + \left(\frac{1}{c_2^B}\mathbf{B_1C^BB^T_{BS}}\right)\alpha_{BS}\underline{p_S^B}. \tag{3.6.19}$$

As noted above, the material properties are obtained from the wave velocities, which can also be used for the stiffness matrices $\mathbf{C}$. The angles are also known values along with the particle velocity amplitudes at the interface, given by α_{BL} and α_{BS}. These amplitudes can be found in the simulation from the particle velocities at the target-anvil interface, giving

$$V_x^L\hat{i} + V_y^L\hat{j} = \alpha_{BL}\underline{p_L^B} = \alpha_{BL}\left(cos\beta_3\hat{i} + sin\beta_3\hat{j}\right) = \alpha_{BL}\hat{i}. \tag{3.6.20}$$

In Equation 3.6.20, V_x^L and V_y^L refer to the particle velocities normal and perpendicular to the rear

surface of the target, respectively, after the longitudinal wave arrives in the anvil. Since this wave is nominally parallel to the rear surface, $V_x^L = \alpha_{BL}$ and $V_y^L = 0$. Similarly for the shear wave,

$$V_x^S\hat{i} + V_y^S\hat{j} = \alpha_{BL}\underline{p_L^B} + \alpha_{BS}\underline{p_S^B} = \alpha_{BL}\left(cos\beta_3\hat{i} + sin\beta_3\hat{j}\right) + \alpha_{BS}\left(-sin\beta 4\hat{i} + cos\beta_4\hat{j}\right) = \left(\alpha_{BL} - \alpha_{BS}sin\beta_4\right)\hat{i} + \alpha_{BS}cos\beta_4\hat{j}. \tag{3.6.21}$$

The assumption that the longitudinal wave is parallel to the rear surface was used in Equation 3.6.21 to eliminate the angle dependence of β_3. With this decoupled equation, α_{BS} can be directly solved for using V_y^S and β_4. Combining Equations 3.6.18-3.6.21 leads to a system of equations with the unknowns α_{AL}^0, α_{AS}^0, α_{AL}, and α_{AS}. These equations can be used to find the in-situ particle velocities in the target given by

$$\alpha_{AL}^0\underline{p_L^{A0}}, \tag{3.6.22}$$

after the longitudinal wave, and

$$\alpha_{AL}^0\underline{p_L^{A0}} + \alpha_{AS}^0\underline{p_S^{A0}}, \tag{3.6.23}$$

after the shear wave.

Taking this approach one step further, the rear surface velocities at the anvil can be used to find the in-situ velocities within the anvil and the subsequent in-situ velocities in the target. This method could be used to find the in-situ velocities from the rear surface measurements in an experiment. In this case, Figure 3.22 shows the wave state. In Figure 3.22, it can be seen that the transmitted longitudinal and shear waves from Figure 3.21 are now the incident waves on the rear surface of the anvil. Furthermore, since the window is parallel to the rear surface of the target, the angles of the waves remain the same. Although the waves don't actually hit the rear surface at the same time, they are shown as they would appear at the rear surface when they arrive there. Using Equation 2.1.54 it can be shown the reflected angles are respectively the same as the incident angles for each wave. Using continuity of velocity at the rear surface of the anvil, the following relations can found

$$\left(\alpha_{IL} - \alpha_{RL}\right) - \left(\alpha_{IS} + \alpha_{RS}\right)sin\beta_4 = V_x^{end} \tag{3.6.24}$$

and

$$(\alpha_{IS} - \alpha_{RS})\, cos\beta_4 = V_y^{end}. \tag{3.6.25}$$

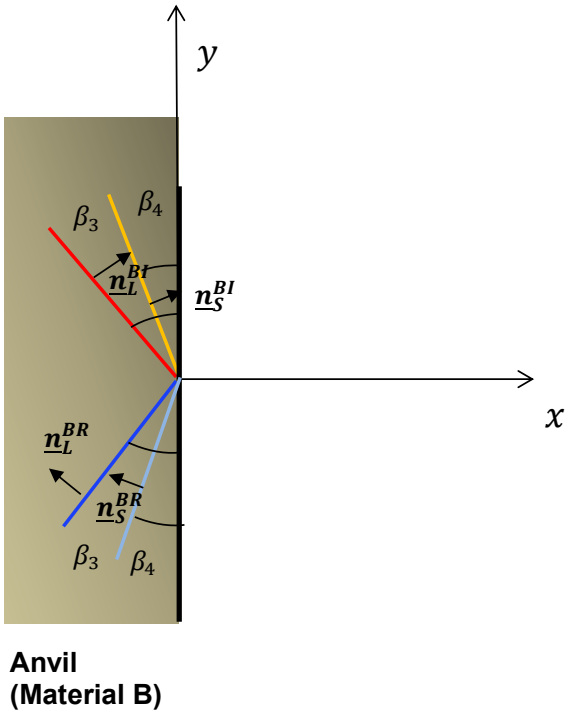

Figure 3.22: Wave state at rear surface of anvil for the oblique wedge setup. The red line is the incident shock wave, the orange is the incident shear wave, the dark blue is the reflected shock and the light blue is the reflected shear. β_i is the angle with respect to the interface for each wave and $\underline{n}$ is the normal for each wave, where the subscripts S and L refer to the shear and longitudinal waves, respectively, and the superscripts BI and BR indicate an incident or reflected wave in material B, the anvil, respectively. The incident waves don't hit the rear surface at the same time, but have been shown as they would appear at the rear surface.

Here, α_{IL}, α_{RL}, α_{IS},and α_{RS} are the amplitudes of the particle velocities across the incident and reflected longitudinal waves, and the incident and reflected shear waves, respectively. V_x^{end} and V_y^{end} are the particle velocities measured at the rear surface of the anvil. Applying continuity of tractions, where the rear surface tractions are set to zero, results in the equations

$$\frac{\lambda + 2\mu}{c_1}(\alpha_{IL} + \alpha_{RL}) - \frac{2\mu cos\beta_4 sin\beta_4}{c_2}(\alpha_{IS} - \alpha_{RS}) = 0 \tag{3.6.26}$$

$$\frac{\mu\left(cos^2\beta_4 - sin^2\beta_4\right)}{c_2}(\alpha_{IS} + \alpha_{RS}) = 0. \tag{3.6.27}$$

From 3.6.27, it is found that $\alpha_{IS} = -\alpha_{RS}$ and substituting this result into 3.6.25 leads to

$$\alpha_{IS} = \frac{V_y^{end}}{2cos\beta_4}. \tag{3.6.28}$$

Substituting in the results of Equation 3.6.27 for $(\alpha_{IS} + \alpha_{RS})$ into Equation 3.6.24, and combining this with Equation 3.6.26 solves for α_{IL}, where

$$\alpha_{IL} = \frac{2\mu c_1 \alpha_{IS} cos\beta_4 sin\beta_4}{c_2\left(\lambda + 2\mu\right)} + \frac{V_x^{end}}{2}. \tag{3.6.29}$$

The results of Equations 3.6.28 and 3.6.29 can finally be used to find the in-situ particle velocities in the anvil which can then be used to find the in-situ velocities in the target through the approach described by Equations 3.6.18 and 3.6.19.

To test whether these theories could be used for velocities measured in experiments, CTH was implemented to model the setup. WC was modeled in CTH with the Mie-Grüneisen EOS. These parameters are not in the model database in CTH and hence had to be found through outside sources. The parameters used for this model were $\rho = 15.4$ g/cm^3, $C_0 = 4.93$ km/s, $S = 1.309$, $c_v = 238$ J/Kg/K, and $\gamma_0 = 1.44$ where ρ is the density, C_0 is the sound speed in Equation 2.2.7, S is the empirical constant in Equation 2.2.7, c_v is the specific heat, and γ_0 is the Grüneisen parameter. Density, sound speed and the empirical constant S were all found in [40], c_v was found from [23], and the Grüneisen parameter was determined from [59]. The linearly elastic perfectly plastic strength model was used, as a more detailed model was not available in CTH, with parameters Poisson's ratio $\nu = 0.2$ and yield strength in tension $\sigma_Y^0 = 4.46$ GPa [37]. The results of this simulation are shown in Figures 3.23 and 3.24.

In Figures 3.23 and 3.24, the longitudinal and transverse particle velocities are shown for the Mo Mo Ta WC oblique wedge configuration at a 10 degree angle of obliquity and 1000 m/s impact. In these figures, u_p and v_p are the longitudinal and transverse particle velocities in the target. The "calculated u_p in target from anvil" and "calculated v_p in target from anvil" use Equations 3.6.18-3.6.23 to calculate in-situ particle velocities in the target from the particle velocities in the anvil measured after the passage of the longitudinal shock and shear wave into the anvil. "Calculated u_p in target using impedance" uses impedance matching techniques for a shock wave, much like the approach described in Figure 3.17 for a window, and uses the particle velocity in the anvil to make these calculations. "u_p in anvil" and "v_p in anvil" are the particle velocities in the anvil after the passage of the transmitted shock and shear waves. "Calculated u_p in target using end velocity" and "calculated v_p in target using end velocity" implement Equations 3.6.24-3.6.29 to find the in-situ

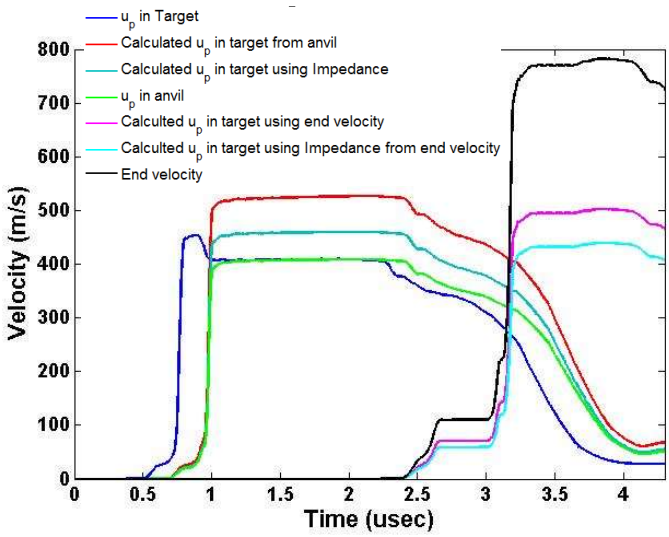

Figure 3.23: Longitudinal particle velocities for Mo Mo Ta WC oblique wedge configuration. u_p is the velocity in the target, "calculated u_p in target from anvil" is the longitudinal velocity calculated from the particle velocity in the anvil. "Calculated u_p in target using impedance" uses impedance matching techniques for a shock wave using particle velocity in the anvil. "u_p in anvil" is the particle velocity in the anvil. "Calculated u_p in target using end velocity" is the particle velocity in the target calculated using the velocity measured at the rear surface of the anvil. "Calculated u_p in target using impedance from end velocity" uses impedance matching techniques for shock waves from the rear surface of the anvil. "End velocity" is the particle velocity at the rear surface of the anvil.

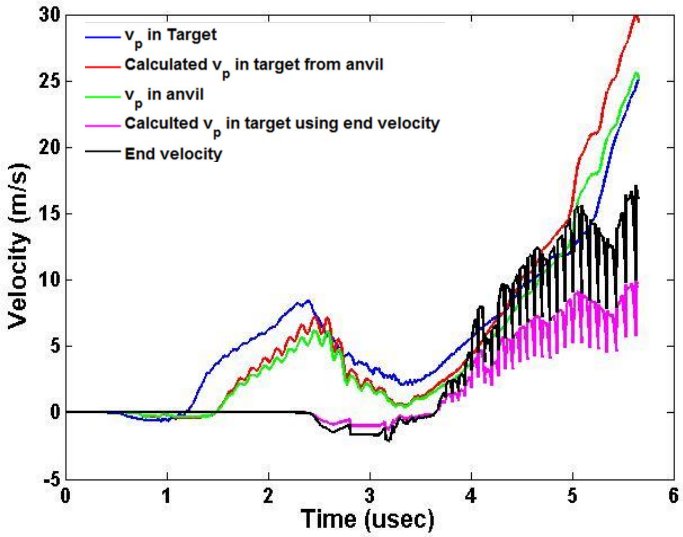

Figure 3.24: Transverse particle velocities for Mo Mo Ta WC oblique wedge configuration. v_p is the velocity in the target. "Calculated v_p in target from anvil" is the transverse velocity calculated from the particle velocity in the anvil. "v_p in anvil" is the particle velocity in the anvil. "Calculated v_p in target using end velocity" is the particle velocity in the target calculated using the velocity measured at the rear surface of the anvil. "End velocity" is the particle velocity at the rear surface of the anvil.

velocities in the anvil from the rear surface measurements of the anvil and subsequently find the in-situ particle velocities in the target using Equations 3.6.18-3.6.23 with these calculated velocities in the anvil. "Calculated u_p in target using impedance from end velocity" uses impedance matching techniques for shock waves once again, but starting from the rear surface of the anvil to find the in-situ velocity in the target. This results in dividing the rear surface velocity in half, which gives the in-situ velocity in the anvil, and then using the same approach as that in Figure 3.17 to find the velocity in the target. Finally "end velocity" in both figures is the particle velocity at the rear surface of the anvil.

In Figure 3.23, the longitudinal velocity in the target prior to the shear wave arrival is 448.8m/s. Interestingly enough the velocity does increase to 453.5 m/s after the shear wave passes which does indicate an effect of the oblique shear wave on longitudinal velocity, however, this is only a 1.05% growth and hence the assumption that only the shock wave affects the longitudinal velocity suffices. The remainder of the velocities are shown in Table 3.5. As can be seen from the results, the impedance matching technique works much better for finding the in-situ velocities as opposed to the psuedo-elastic wave analysis, where the difference for the impedance matched in-situ velocity is 3.63% using the rear surface velocity versus 10.23% for the psuedo-elastic technique. In Figure 3.24, it can be seen that the shear velocity is not level and peaks at a certain point. This trend could be due to a variety of reasons such as wave reflections from the shock wave (if it is not perfectly parallel to the rear surface), as well as the unsteady nature of the wave due to the changing viscosity of the material. For this case, impedance matching was not used since it was shown for the windowed example that it did not work well. Furthermore, it is clear that the shear wave is not parallel to the rear surface and impedance matching does not take this into account. Using the psuedo-elastic approach described above, the in-situ velocities calculated from the in-situ anvil particle velocity and rear surface particle velocity are shown in Table 3.6 and are 14.85% and 11.16% different, respectively, than the actual transverse in-situ particle velocity in the target, given by the simulation. Here it should be noted that the peak velocity was taken for all but the "rear surface" and "in-situ calculated from rear surface" velocity values. In these cases, the average peak value was found. In the latter case, it is apparent in Figure 3.24 that there is an oscillatory nature to the velocity perhaps due to an issue with the mesh if there were two materials in one cell and hence the average value had to be taken. Although the error here is higher than for the longitudinal velocity found using impedance matching, the values are still promising and show that this technique could be used in an experiment.

The final analysis that needs to be made is to determine whether the anvil is yielding. Using

	u_p Target	u_p Target from Anvil	u_p Impedance	u_p Anvil	u_p Target from End	u_p Impedance from End	u_p End
Velocity (m/s)	448.8	532.2	457.7	407.2	494.7	432.5	770.0
Difference from in-situ in Target (%)	n/a	16.58	1.98	n/a	10.23	3.63	n/a

Table 3.5: Longitudinal particle velocities in Mo Mo Ta WC oblique wedge configuration.

	v_p Target	v_p Target from Anvil	v_p Anvil	v_p Target from End	v_p End
Velocity (m/s)	8.42	7.17	6.13	7.48	12.19
Difference from in-situ in Target (%)	n/a	14.85	n/a	11.16	n/a

Table 3.6: Transverse particle velocities in Mo Mo Ta WC oblique wedge configuration.

the same approach outlined for the Mo Mo Ta Sa configuration, where Equation 3.6.8 was used to find the maximum shear strength the anvil could support, it was found that the anvil does yield. Once again, a linearly elastic perfectly plastic model was used with $\sigma_Y^0 = 4.46$ GPa [37]. The results of this study are shown in Figure 3.25. As with the sapphire window, the analysis shows that the material is yielding, but it is not clear by how much since σ_Y^0 could be strain-rate dependent and not a constant value. Nevertheless, although yielding does occur, this approach still seems to be working which could indicate that the material is just starting to yield. A more detailed model for tungsten carbide could be used in the future to study this phenomenon.

3.7 Conclusions

Theoretically, a variety of driver materials, impactor materials, angles of obliquity and impact velocities can be implemented in the oblique wedge configuration to study the response to shear stress at a wide range of pressures. This study has shown that with an increased impact velocity, a greater state of longitudinal stress can be created at which the shear response can be tested. Furthermore, with an increase in the angle of obliquity for the incident wave, a larger shear wave angle will form. It has been shown that this setup can measure shear stress for both tantalum and aluminum, but it has limitations. For the case of Be Be Al LiF, the maximum shear stress was close to the shear stress in the experiment, while this was not true for the Cu PMMA Al LiF configuration. An explanation for this could be that the PMMA may have yielded while the Be did

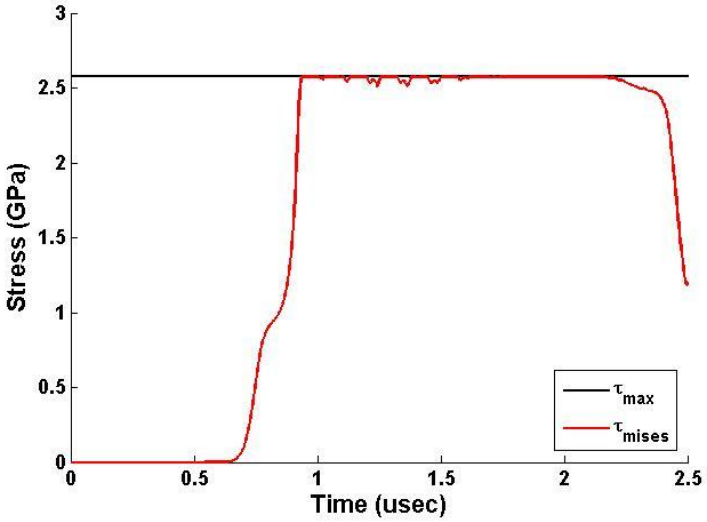

Figure 3.25: Maximum shear stress and Mises shear stress for oblique wedge configuration of Mo Mo Ta WC in the WC anvil calculated from CTH simulation.

not and hence the shear wave transmitted into the Al was weaker, causing the material to yield from longitudinal and lateral stresses, rather than shear. To mitigate a similar problem in the Cu Cu Ta LiF configuration, Mo was used as a driver since it has a higher shear impedance and yield strength than Cu which resulted in a higher transmitted shear in Ta that was close to maximum shear stress and could be used to calculate the strength of the material. Thus, it was concluded that the driver material must have a higher shear impedance and strength than the target for the target to reach the maximum shear stress value in a state of pure shear.

At higher impact velocities, it was found that a constant shear wavespeed cannot be assumed. Impedance matching for transverse waves is also difficult since they are not parallel to the transmitted longitudinal waves and is an issue when dealing with targets and windows that are not very close in impedance. A solution to the latter problem could be the implementation of high strength anvils that remain elastic throughout the experiment such that the elastic oblique wave analysis can be used to relate the measured particle velocities at the rear surface of the anvil to the in-situ velocities in the target. Using the Mo Mo Ta Sa configuration and replacing the sapphire with tungsten carbide, it was shown that such an approach could work.

Chapter 4

Y-Cut Quartz Sandwich Configuration

4.1 Introduction

Another novel method to test the effects of shear on materials is by using y-cut quartz as a shear generator. Upon impact, y-cut quartz generates two waves due to its anisotropic nature [75], [77]. The first wave, called "quasi-longitudinal" (QL), travels at a faster velocity than the second "quasi-transverse" (QT) wave, however, both waves contain longitudinal and shear particle velocity components. If the sample is cut such that the crystallographic Y direction is normal to the surface and Z is parallel, then the waves will always travel in the direction of the Y axis, with velocity components in the Y and Z directions [18]. In Figure 4.1, a schematic of a y-cut quartz sandwich configuration is shown. Note that, in the simulations conducted for this study, the impact is in the x direction in the experiment coordinate frame, and the crystallographic Y direction of the quartz is oriented in this direction with the quartz Z direction in the z direction of the simulation. Both coordinate systems are shown in Figure 4.1, with the quartz coordinates denoted by upper cases letters and the superscript q. Upon impact, the waves travel into the quartz where the components of velocity are transmitted into the target of interest. These velocity components generate both pressure and shear waves in the target. Using an anvil that remains elastic throughout the experiment allows the velocity to be measured at the rear surface, which can be used to find the stress state in the target, defined by equations

$$\sigma = \frac{1}{2}\rho_0^A C_L^A u_{fs} \tag{4.1.1}$$

and

$$\tau = \frac{1}{2}\rho_0^A C_S^A v_{fs}. \tag{4.1.2}$$

In these equations, ρ_0^A is the initial density of the anvil, C_L^A and C_S^A are the elastic longitudinal and shear wavespeeds in the anvil, respectively, and u_{fs} and v_{fs} are the longitudinal and transverse free surface velocities, respectively.

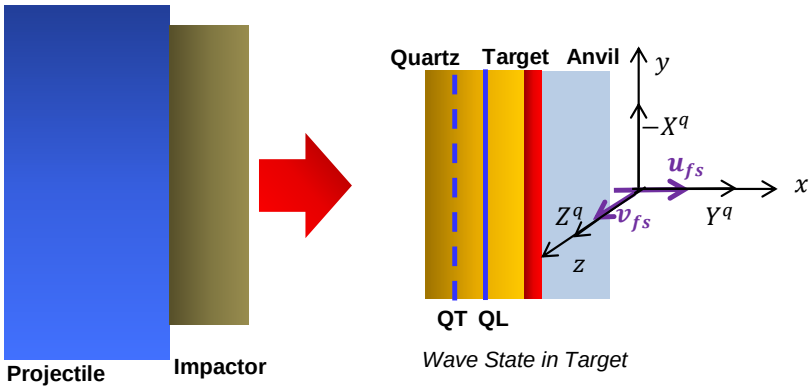

Figure 4.1: Schematic of the y-cut quartz sandwich configuration to test material response to shear. Upon impact, a quasi-longitudinal (QL) and quasi-transverse (QT) wave is generated due to the anisotropic nature of the quartz. Each wave has a shear and longitudinal component of velocity that is transmitted into the target. The coordinate systems for the simulations and the quartz are shown. Simulation coordinates are in lower case letters and quartz coordinates are in upper case with the superscript q.

4.2 Oblique Gun Experiments

To study shear response and strength measurement in materials, the pressure-shear experiment has been used. Many of these types of experiments were conducted using an oblique (or slotted barrel) gun. In this experimental setup, the impactor and target are oriented parallel to one another, but at an angle with respect to the horizontal axis. Rotation of the projectile is eliminated by implementing a key that is guided by a keyway in the gun barrel [2]. The velocity vector of the projectile contains both longitudinal and shear components due to the skewed angle and hence, both pressure and shear waves are generated upon impact. One dimensional wave theory, as discussed in Section 2.1.3, can be used to analyze the effects of the waves propagating into the specimen since the target is loaded uniformly. This analysis is no longer valid when cylindrical unloading waves from the edges of the target reach the point of observation.

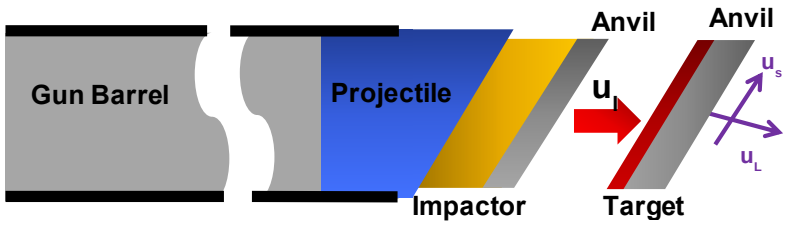

Figure 4.2: Schematic of slotted barrel gun.

A basic schematic of this setup is shown in Figure 4.2. In this type of experiment, the impactor can be either a solid material, or consist of a hard anvil backed by a material with a different impedance in order to conduct strain-rate change tests [76]. The target can also be either a solid material, or a thin sample backed by a high strength anvil. To maintain high shear strain-rates, thin foil samples (< 500 μm) sandwiched between plates that remain elastic are used [58], [30]. Within the specimen, the stress state rings up until it is uniform throughout the sample and is continuous at each of the anvil-specimen interfaces. For this reverberation to occur, the target and flyer plates must have a higher impedance than the sample. The longitudinal velocity difference causes the material to be compressed due to the 1D strain assumption, at which point it reaches a steady state and the velocity is continuous. If the specimen responds elastically, the velocity will be continuous throughout, however, if it behaves plastically, the shear velocity is discontinuous and the difference between the front and back surfaces can be used to find the strain-rate [42], where

$$\dot{\gamma} = \frac{v_F - v_B}{h}. \tag{4.2.1}$$

Here, $\dot{\gamma}$ is the strain-rate, v_F and v_B are the velocities at the front and back surfaces of the specimen, respectively, and h is the thickness of the specimen and is assumed to be a known value. The velocity at the back surface of the specimen, v_B, is assumed to be continuous with the velocity in the anvil and is given by

$$v_B = \frac{1}{2} v_{fs}, \tag{4.2.2}$$

which can be shown to be the case by using the characteristic in Equation 2.1.60b. The development of the longitudinal and shear stress states is shown in Figures 4.3a and 4.3b. As can be seen in Figure 4.3a, the impactor begins to travel at u_0, which for the oblique gun is equal to $V_0 cos\theta$ — where V_0 is the impact velocity and θ is the angle of inclination of the impactor and target. Once the impactor hits the thin sample, the sample reaches some stress state and continues to reverberate

between the two Hugoniots, shown in red and beige in Figure 4.3a. Although initially these are the target and impactor Hugoniots, since the two anvils are assumed to be the same material, their Hugoniots actually reflect onto one another as the sample wave reverberates between the two plates. The shear stress state, however, is slightly different. Here, the sample reaches some stress state as it is impacted by the flyer and, after a few reverberations (not shown in Figure 4.3b), the sample reaches a shear stress state at which point it begins to flow. The anvil unloads at the rear surface at some free surface velocity, v_{fs}, and zero stress. The stress must be continuous across the sample and hence the impactor anvil and target anvil at the interfaces with the sample must be at the same shear stress. Velocities are not necessarily continuous and hence the front of the sample reaches some velocity, v_F, while the in-situ velocity in the anvil backing plate, v_B, matches that of the sample's back surface. This technique was found to be advantageous to using a homogeneous target where the wave profile attenuates and shear strain-rates diminish.

4.3 Y-Cut Quartz Sandwich Configuration

The concept of the sandwich configuration that is used with the oblique gun can be employed in a normal impact gun by using y-cut quartz to generate the shear wave. Figure 4.4 depicts the x-t diagram for such a configuration. In this case, there are two anvils, unlike the setup shown in Figure 4.1. Upon impact, the QL and QT waves propagate into the y-cut quartz and generate two longitudinal (P) waves and two shear (S) waves due to each wave having both longitudinal and shear particle velocity components in the quartz. It is assumed here that since the specimen is so thin, the waves propagate in the second anvil without an impact to their velocity.

Although in the oblique gun sandwich experiment the specimen front surface velocity can be found by using the impact velocity and impedance matching, using y-cut quartz complicates the problem. Thus, to find the front surface velocity and be able to calculate the strain-rate, one could monitor the velocity by using interferometry techniques with a probe monitoring the rear surface of the anvil through a notch in the full target or by conducting a separate experiment with the impactor and target, where the target would consist of the quartz backed by the anvil. The free surface measurement off of the WC would match the in-situ measurement in the full target setup with the specimen and the anvil. This in-situ measurement — let it be called v_{IS} — can be used with the jump conditions to find the front surface velocity for the specimen. Figure 4.5 shows the shear stress-particle velocity Hugoniot for such a configuration. It is similar to Figure 4.3b, however, v_0 is now an unknown since the WC driver is stationary. Furthermore, this time the Hugoniots are

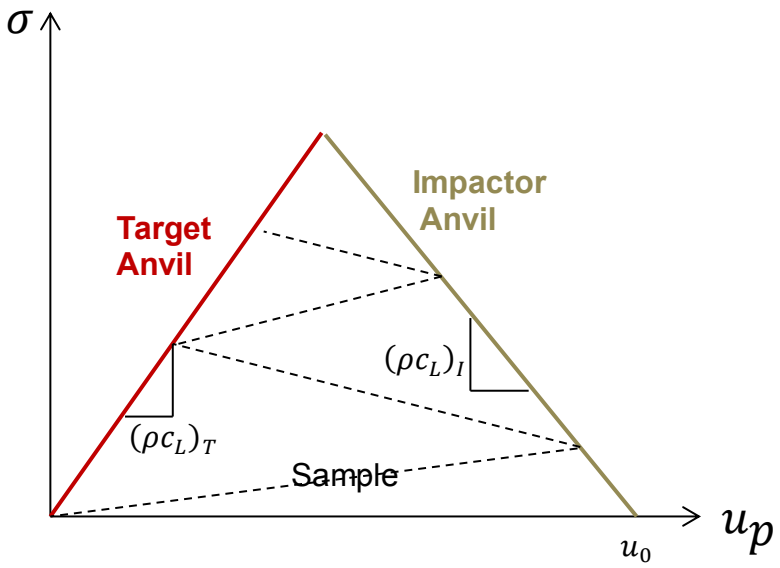

(a) Longitudinal Stress State

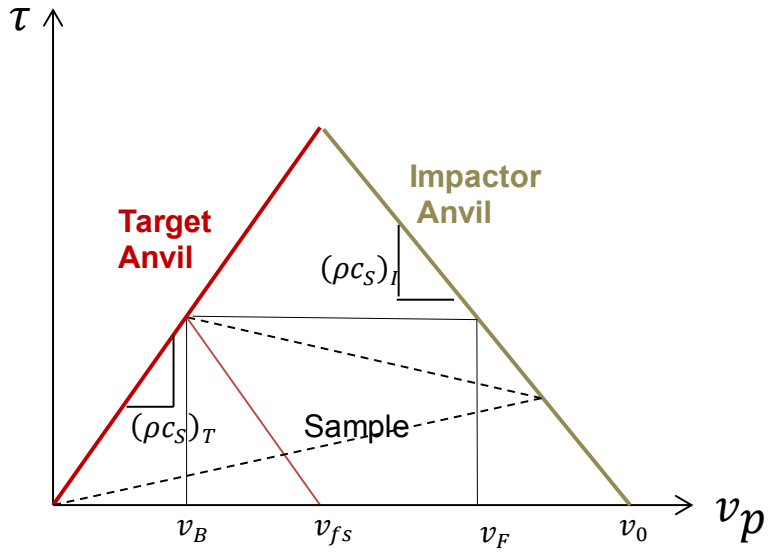

(b) Shear Stress State

Figure 4.3: Development of stress state in sample for the pressure-shear experiment.

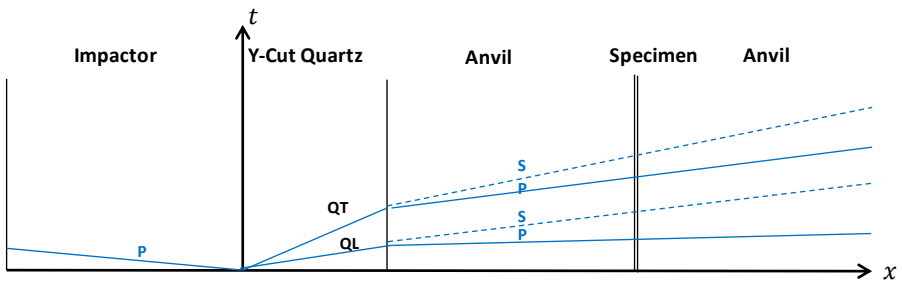

Figure 4.4: x-t diagram for a y-cut quartz sandwich configuration with two anvils.

labeled as forward and backward for each of the WC plates. The reason for this is that, initially, the shear wave travels forward into the WC and the driver reaches some shear stress τ_{IS}. At this point, the wave travels forward into the sample, but part of it is reflected into the WC driver; thus the stress state in the driver can be found along the backward Hugoniot. As the wave in the sample travels forward, it is reflected at the sample-backing interface, and a wave is sent forward into the backing anvil plate, where its stress state lies along the forward Hugoniot. At this point the sample reaches some stress state τ_S, and the backing anvil must unload to zero stress and some free surface velocity v_{fs}. It is assumed that the sample reaches a steady state and the shear stress is uniform throughout such that the front surface velocity at the WC driver-sample interface lies on the backward Hugoniot. Equation 2.2.8 can be used to find the following relations from Figure 4.5:

$$\tau_{IS} = \rho_{WC} c_2 v_{IS}, \tag{4.3.1}$$

$$\tau_S = \rho_{WC} c_2 v_B, \tag{4.3.2}$$

and

$$\tau_{IS} = \tau_S + \rho_{WC} c_2 \left(v_F - v_{IS}\right), \tag{4.3.3}$$

where τ_{IS} is the in-situ shear stress in the WC and τ_S is the shear stress throughout the specimen. Equation 4.3.1 can be used to solve for τ_{IS} in order to substitute it into Equation 4.3.3. The stress in the specimen, τ_S, can be calculated using the free surface velocity in the two driver setup to find v_B and plugging it into Equation 4.3.2. Finally, v_F can then be found from Equation 4.3.3.

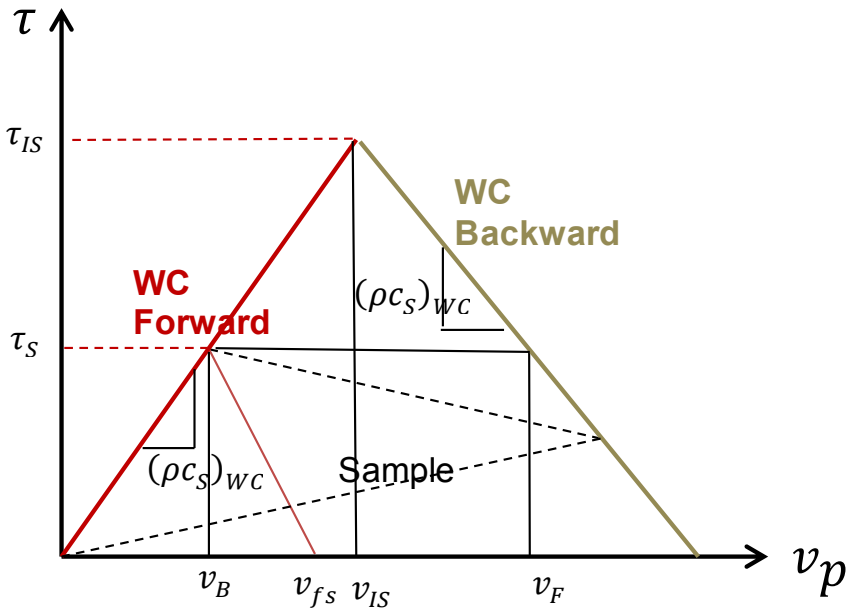

Figure 4.5: Shear stress-particle velocity Hugoniot for y-cut quartz two driver configuration.

4.3.1 Laslo Simulations

To design targets for testing, numerical simulations were performed using Laslo (Lagrangian Analysis and Simulation of Loading in One dimension) [70]. Developed at Sandia National Laboratories, Laslo is a 1D transient dynamics – time history analysis – code and uses an updated Lagrangian formulation to solve the conservation equations. To integrate these equations, it discretizes spatially with linear two-node elements and uses a central difference scheme to integrate in time. The theory behind this code is covered in [11].

4.3.1.1 Models

As mentioned, at high pressures, solid materials behave in a fluid like manner, however, to model shock wave discontinuities, artificial viscosity is used [15]. This term is implemented to "smooth" the shock front. The user can choose to describe viscosity with either a linear or quadratic equation, given by [11]

$$q = c_0 \rho \left(\triangle u\right)^2 + c_L a \rho \left|\triangle u\right|, \tag{4.3.4}$$

where $\triangle u$ is the jump in velocity across the element, c_0 and c_L are non-dimensional constants, ρ is density and a is sound speed.

	Tungsten Carbide [39]	**Y-Cut Quartz** [47]
$\rho\,(kg/m^3)$	15400	2650
$C_{11}\,(GPa)$	720.0	86.8
$C_{12}\,(GPa)$	254.0	7.0
$C_{13}\,(GPa)$	151.0	11.9
$C_{14}\,(GPa)$	0.0	-18.0
$C_{15}\,(GPa)$	0.0	0.0
$C_{16}\,(GPa)$	0.0	0.0
$C_{22}\,(GPa)$	720.0	86.8
$C_{23}\,(GPa)$	151.0	11.9
$C_{24}\,(GPa)$	0.0	18.0
$C_{25}\,(GPa)$	0.0	0.0
$C_{26}\,(GPa)$	0.0	0.0
$C_{33}\,(GPa)$	972.0	105.8
$C_{34}\,(GPa)$	0.0	0.0
$C_{35}\,(GPa)$	0.0	0.0
$C_{36}\,(GPa)$	0.0	0.0
$C_{44}\,(GPa)$	328.0	58.2
$C_{45}\,(GPa)$	0.0	0.0
$C_{46}\,(GPa)$	0.0	0.0
$C_{55}\,(GPa)$	328.0	58.2
$C_{56}\,(GPa)$	0.0	-36.0
$C_{66}\,(GPa)$	233.0	39.9

Table 4.1: Elastic constants for the stiffness matrices of tungsten carbide and y-cut quartz. The parameter ρ is density and Cij is each term in the stiffness matrix.

Tungsten carbide was used for the anvil in all of the simulations due to its high strength so that it could be used for a variety of specimens since it stays elastic at higher pressures. A linear elastic model was used for both y-cut quartz and WC, with parameters for the stiffness matrix given in Table 4.1. The theory to predict wave propagation in y-cut quartz is based on the work by Johnson [47], [48].

The remaining materials, tantalum and aluminum 6061-t6, used a Mie-Grüneisen EOS, see Section 3.6.1, and a Johnson-Cook strength model with the parameters set such that the model was essentially linear elastic perfectly plastic. The reason for the latter step is that the linear plastic model does not work in Laslo and hence the Johnson-Cook model can be used instead. The Johnson-Cook model describes strength in the following way:

$$Y = (a + b\epsilon^n)\,(1 + c\log\dot{\epsilon})\,(1 - T^{*m})\,, \tag{4.3.5}$$

where Y is the strength and is strain-rate dependent. The value a is the initial yield strength, ϵ is the equivalent plastic strain, $\dot{\epsilon}$ is the strain-rate, and T^* is the non-dimensional temperature defined by

	Aluminum 6061-T6 [73]	**Tantalum** [73]	**Polyurethane** [73], [54]
$\rho\,(kg/m^3)$	2703	16654	1265
ν	0.34	0.33	0.18
$a\,(GPa)$	0.29	0.77	0.0021
b	0	0	0
c	0	0	0
m	1	1	1
n	0	0	0
$T^*\,(K)$	273	273	273
$t_{ref}\,(K)$	298	298	298
$c_v\,(J/Kg/K)$	1070	160	86
γ	1.97	1.60	1.55
S	1.37	1.22	1.577
$C_0\,(m/s)$	5220	3390	2486

Table 4.2: Parameters for the Mie-Grüneisen EOS and Johnson-Cook Strength models. ρ is density, ν is poisson's ratio, a is the initial yield strength, b, c, and n are strain-rate hardening factors, m is a thermal-softening factor, T^* is a nondimensional temperature, t_{ref} is the initial temperature, c_v is the specific heat capacity, γ is the Grüneisen parameter, S is the linear coefficient and C_0 is the sound speed in the $U_S - u_p$ Hugoniot.

$$T^* = \frac{T - T_r}{T_m - T_r}, \tag{4.3.6}$$

where T_r is the room temperature, T_m is the melt temperature and T is the temperature which is somewhere between the two, $T_r \leq T \leq T_m$. The remaining parameters, b, c, and n, are all strain-rate hardening factors and the constant m is a thermal-softening factor [62]. The parameters for these models are given in Table 4.2.

4.3.2 Two Driver Target Design

The first approach used was the y-cut quartz (YQ) sandwich design with a WC and YQ driver followed by a thin sample and a WC anvil bounding plate. Simulations were performed with an aluminum 6061-t6 impactor at 400, 450, and 500 m/s. It was determined that 400 m/s was the choice of interest due to material yielding, which will be discussed later. Although it does not necessarily matter what impacts the quartz, x-cut quartz and aluminum 6061-t6 are most commonly used as they are both well matched to the quartz and therefore produce a close to symmetric impact. The advantage of using aluminum is that it is light-weight and hence can be thick such that reflections will not be a problem during the experiment.

Figure 4.6 shows the x-t diagram for part of the configuration. As can be seen, upon impact the waves generated correspond to those discussed for Figure 4.4. Figures 4.7a and 4.7b show the velocity

profiles at the tracers shown in red and green on Figure 4.6. The tracer at 0.01 m corresponds to the interface between the YQ and WC, and the green tracer at 0.015 m is midway through the WC. Times t_1 and t_2 indicate the arrival times for QL and QT at the YQ-WC interface. The times t_3, t_4, t_5, and t_6 indicate the times of arrival of the pressure and shear waves due to QL and the pressure and shear waves due to QT, respectively, at the tracer midway through the WC.

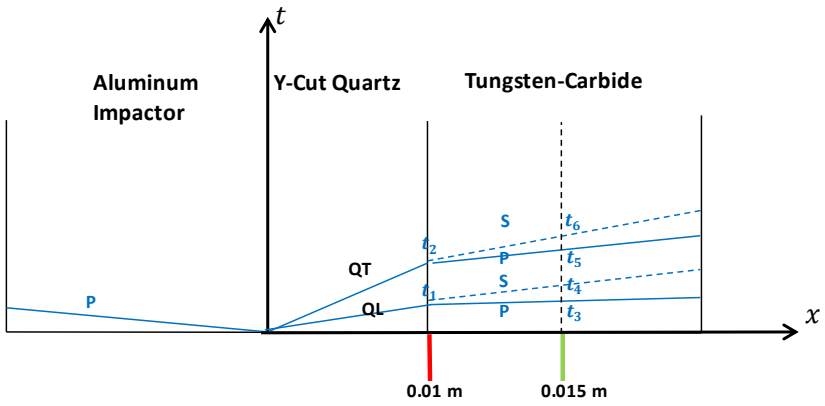

Figure 4.6: x-t diagram for the two driver y-cut quartz sandwich configuration for the impactor and two drivers, YQ and WC.

The distance traveled and the individual arrival times can be used to find the wave velocities in each material, where the wave velocities of QL and QT in the YQ are given by

$$C_{QL}^{YQ} = \frac{0.01 \text{ m}}{t_1} = 6031.36 \text{ m/s} \tag{4.3.7}$$

and

$$C_{QT}^{YQ} = \frac{0.01 \text{ m}}{t_2} = 4391.74 \text{ m/s}, \tag{4.3.8}$$

respectively. Since the WC remains elastic, both pressure and shear waves should travel at the same elastic longitudinal and transverse velocities, respectively, and thus only the first arrival time for each wave needs to be used for the calculation. These velocities are

$$C_{L}^{WC} = \frac{0.005 \text{ m}}{t_3 - t_1} = 6849.32 \text{ m/s} \tag{4.3.9}$$

and

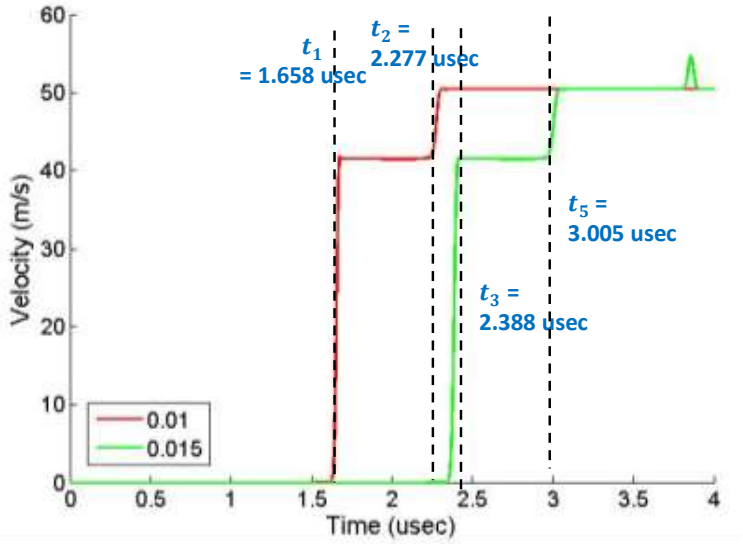

(a) Longitudinal velocity profile for two tracers, one at the YQ-WC interface (red) and the other midway through the WC (green).

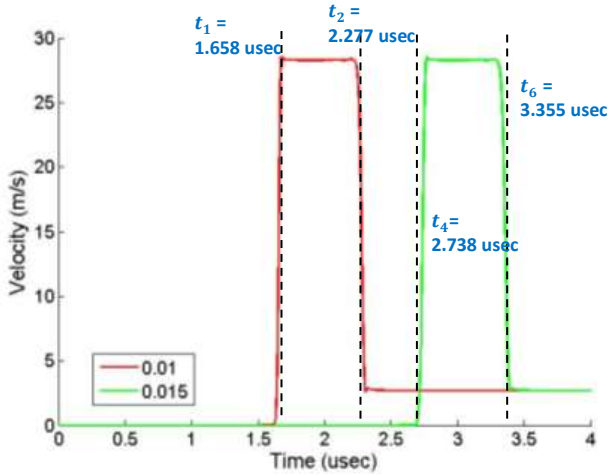

(b) Transverse velocity profile for two tracers, one at the YQ-WC interface (red) and the other midway through the WC (green).

Figure 4.7: Longitudinal and shear particle velocities for y-cut quartz (YQ) two driver sandwich configuration. The second driver and anvil are tungsten carbide (WC). Tracer locations are shown in (m).

$$C_S^{WC} = \frac{0.005 \text{ m}}{t_4 - t_1} = 4629.63 \text{ m/s}. \tag{4.3.10}$$

The goal in this experiment is to subject the specimen to the largest amount of shear, which will occur from the response to the first wave, QL, since its transverse component of velocity is larger. Figure 4.8 shows the entire x-t diagram for the composite target. In this schematic, times t_7, t_8, t_9, and t_{10} correspond to the first and second longitudinal and transverse waves arriving at the rear surface of the WC bounding plate. The goal here is to maximize the amount of time the state after t_8 and prior to t_{10} is seen. These times can be calculated by dividing the distance traveled by the velocity of each wave,

$$t_7 = t_1 + \frac{DWC}{C_L^{WC}} \tag{4.3.11}$$

$$t_8 = t_1 + \frac{DWC}{C_S^{WC}} \tag{4.3.12}$$

$$t_9 = t_2 + \frac{DWC}{C_L^{WC}} \tag{4.3.13}$$

$$t_{10} = t_2 + \frac{DWC}{C_S^{WC}}, \tag{4.3.14}$$

where DWC is the entire thickness of the two WC plates with the specimen.

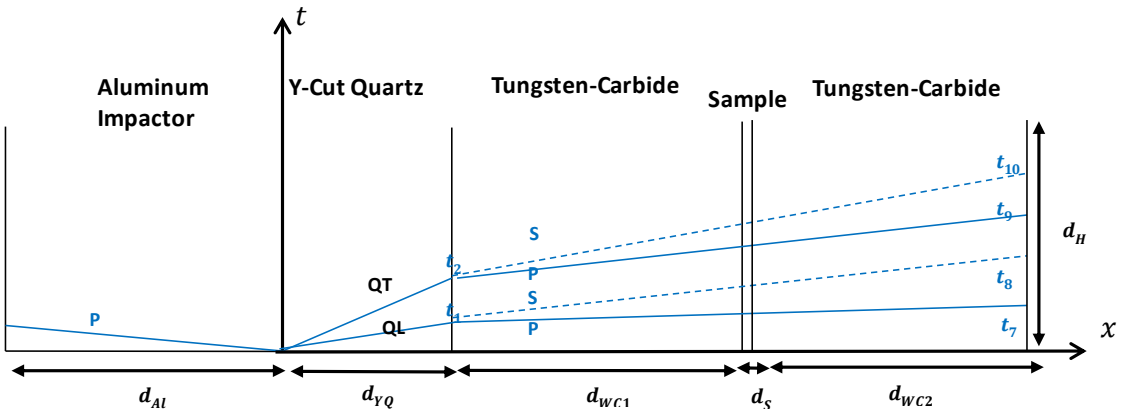

Figure 4.8: x-t diagram for full y-cut quartz two driver sandwich configuration using tungsten carbide as the second driver and the anvil.

The first consideration is to see the entire shear response from the first transverse wave plus a

given read time prior to edge wave arrival. Figure 4.9 illustrates the propagation of edge waves in the composite target. Upon impact, waves begin to propagate in from the corners of the YQ. Since YQ is an anisotropic material, the waves will travel at different velocities depending on the direction of analysis, which results in an elliptical wave front [26]. As a safe measure, the fastest wavespeed can be used to approximate the wave traveling in a cylindrical manner, which is assumed to be traveling at the same velocity as QL. Assuming edge waves travel at the same velocity as the fastest wave is a common practice in the analysis of plate impact experiments. The time it takes for the waves to travel is the distance along the shortest path divided by the velocity of the wave. It is assumed here that the edge waves travel inwards until they reach a certain diameter at the WC interface at which point they continue to propagate towards the center, but this time at the elastic longitudinal wave speed of the WC. The first step is to calculate the shear wave arrival plus some given read time and make certain this occurs prior to edge wave arrival. This step results in

$$t_8 + t_r \leq t_{yq} + \frac{S}{C_L^{WC}}. \tag{4.3.15}$$

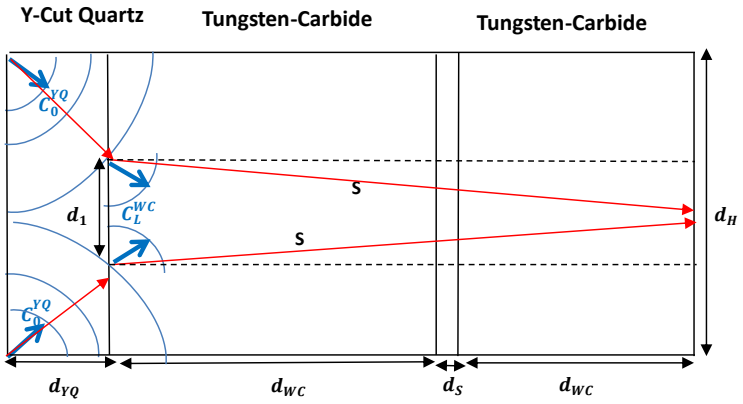

Figure 4.9: Edge wave propagation in two driver y-cut quartz sandwich configuration.

As defined above, t_8 is the arrival of the first shear wave at the rear surface of the second WC plate and the term t_r is the read time after the wave arrives. The sum of these times is set equal to the arrival of the edge waves at the rear surface of the target, which is the time it takes the first set of edge waves to propagate through the quartz, t_{yq}, and the time for the second set to propagate through the remainder of the target, $\frac{S}{C_L^{WC}}$. The most conservative estimate of the time for the edge waves to travel until they affect diameter d_1 in the WC is $\frac{d_{YQ}\sqrt{2}}{C_{QL}^{YQ}}$ and the time for the waves to travel

from this diameter to the point of observation at the rear surface of the WC is $\frac{\sqrt{(DWC)^2+\left(\frac{d_1}{2}\right)^2}}{C_L^{WC}}$, where d_1 can be defined by $d_H - 2d_{YQ}$. Thus, Equation 4.3.15 becomes

$$t_8 + t_r = \frac{d_{YQ}\sqrt{2}}{C_{QL}^{YQ}} + \frac{\sqrt{(DWC)^2 + \left(\frac{d_H - 2d_{YQ}}{2}\right)^2}}{C_L^{WC}}, \tag{4.3.16}$$

where the $\leq$ sign has been replaced by an equal sign for the worst case scenario. Plugging in for t_8 in Equation 4.3.12 results in

$$t_1 + \frac{DWC}{C_S^{WC}} + t_r = \frac{d_{YQ}}{C_{QL}^{YQ}} + \frac{DWC}{C_S^{WC}} + t_r = \frac{d_{YQ}\sqrt{2}}{C_{QL}^{YQ}} + \frac{\sqrt{(DWC)^2 + \left(\frac{d_H - 2d_{YQ}}{2}\right)^2}}{C_L^{WC}}, \tag{4.3.17}$$

where t_1 was replaced by $\frac{d_{YQ}}{C_{QL}^{YQ}}$. Rearranging the terms, the equation becomes a quadratic function for DWC,

$$\begin{aligned} DWC^2\left[\frac{1}{C_S^{WC^2}} - \frac{1}{C_L^{WC^2}}\right] + DWC\left[\frac{2d_{YQ}\left(1-\sqrt{2}\right)}{C_{QL}^{YQ}C_S^{WC}} + \frac{2t_r}{C_S^{WC}}\right] + \\ \left[\frac{d_{YQ}^2\left(1-\sqrt{2}\right)^2}{C_{QL}^{YQ^2}} + \frac{2d_{YQ}t_r\left(1-\sqrt{2}\right)}{C_{QL}^{YQ}} + t_r^2 - \frac{d_H^2}{4C_L^{WC^2}} + \frac{d_H d_{YQ}}{C_L^{WC^2}} - \frac{d_{YQ}^2}{C_L^{WC^2}}\right] = 0. \end{aligned} \tag{4.3.18}$$

This equation is in the form of

$$A\left(DWC\right)^2 + B\left(DWC\right) + C = 0, \tag{4.3.19}$$

where the quadratic formula can be used, given by

$$DWC = \frac{-B \pm \sqrt{B^2 - 4AC}}{2A}. \tag{4.3.20}$$

In addition to edge wave effects, it is important that the sample remain in compression for shear to be transmitted, otherwise slip will occur. As can be seen in Figure 4.10, the focus has now shifted to the effects of the first set of waves resulting from QL since it has the highest shear response. The constraint here indicates that the shear wave arrival plus a certain read time must be recorded prior to the reflected pressure wave off the rear surface of the bounding anvil arriving at the sample and then reflecting back to the anvil rear surface at time t_{11} in Figure 4.10. Similarly, the experiment

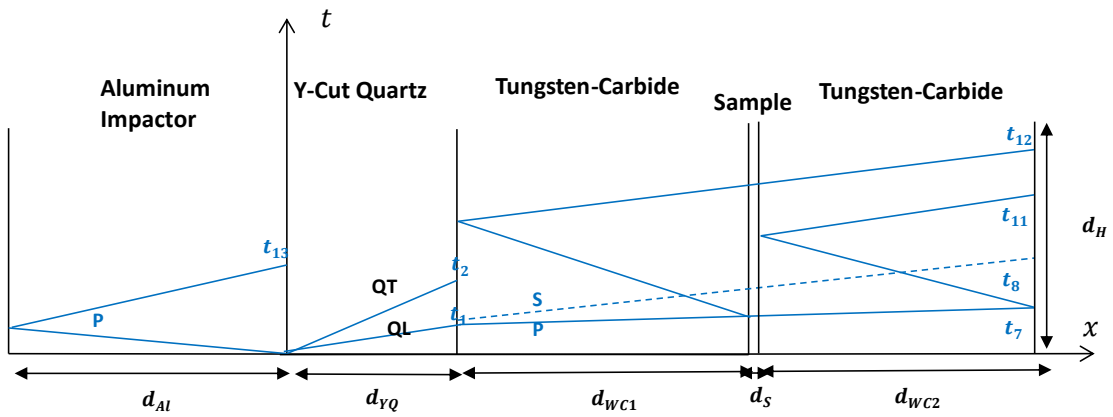

Figure 4.10: x-t diagram for full y-cut quartz two driver sandwich configuration with longitudinal waves reflected at rear surface of bounding anvil and YQ-anvil interface.

must finish prior to the arrival of the P wave that is reflected from the sample, then the YQ-anvil interface and back to the sample, where the back of the anvil receives this information at time t_{12}. Mathematically this becomes

$$t_{11} = t_7 + 2\frac{d_{WC2}}{C_L^{WC}} \geq t_8 + tr. \tag{4.3.21}$$

Plugging in for t_7 and t_8 this equation becomes

$$\frac{DWC}{C_L^{WC}} + 2\frac{dWC_2}{C_L^{WC}} \geq \frac{DWC}{C_S^{WC}} + t_r. \tag{4.3.22}$$

Similarly,

$$t_{12} = t_1 + 2\frac{d_{WC1}}{C_L^{WC}} + \frac{DWC}{C_L^{WC}} \geq t_8 + t_r. \tag{4.3.23}$$

Substituting in the definitions for t_{12} and t_8 this equation becomes

$$2\frac{d_{WC1}}{C_L^{WC}} + \frac{DWC}{C_L^{WC}} \geq \frac{DWC}{C_S^{WC}} + t_r. \tag{4.3.24}$$

Using the fact that $DWC = d_{WC1} + d_{WC2} + dS$, replacing the $\geq$ sign with an $=$ sign for the worst case scenario, and combining 4.3.24 and 4.3.22 results in the stipulation that

$$DWC = \frac{t_r + d_S/C_L^{WC}}{2/C_L^{WC} - 1/C_S^{WC}}. \tag{4.3.25}$$

Equations 4.3.20 and 4.3.25 can be combined for a variety of values for d_H, d_{YQ} and d_S to solve for

Case	d_{YQ} (m)	d_H (m)	d_S (μm)	t_r (ns)	d_{WC1} (mm)	d_{WC2} (mm)	t_8 (μs)	t_{10} (μs)
1	0.01	0.025	25	396.27	2.65	2.64	2.81	3.43
2	0.005	0.025	25	447.80	2.99	3.00	2.13	2.44
3	0.01	0.05	25	902.65	5.95	5.95	4.23	4.85
4	0.005	0.05	25	994.67	6.56	6.57	3.67	3.97

Table 4.3: Calculated read time, t_r, and tungsten carbide (WC) thickness for y-cut quartz two driver sandwich configuration. d_{YQ} is the thickness of the y-cut quartz, d_H is the height of the target, d_S is the sample thickness, d_{WC1} is the thickness of the tungsten carbide driver, d_{WC2} is the thickness of the tungsten carbide backing, t_8 is the arrival of the first shear wave at the rear surface of the target, and t_{10} is the arrival of the second shear wave at the rear surface of the target.

the read time t_r and the thicknesses of the anvils, d_{WC1} and d_{WC2}. Matlab was used to solve for these values and the results of this study are shown in Table 4.3.

In Table 4.3, the values of d_{WC1} and d_{WC2} must be rounded since machining techniques can only be accurate to several decimal places and hence the read time is recalculated. To calculate the true read time, the smallest arrival time out of the arrival of the edge waves at the rear surface, Equation 4.3.16, the arrival of the L wave from the rear surface of the bounding anvil to the target and back to the anvil rear surface, Equation 4.3.22, and the arrival of the L wave from the quartz-anvil interface to the target and then to the rear surface, Equation 4.3.24, is taken from which the arrival of the shear wave at the rear surface, Equation 4.3.16, is subtracted. It is also important to make sure that the second shear wave does not arrive before the entire read time is seen since its shear response is lower. The arrival of both the first and second shear waves are shown in Table 4.3. The only case in which the second shear wave arrives after the entire read time is the first case. The re-calculated read times, representing the time between the arrival of the first and second shear waves, are 309.5 ns, 619 ns, and 309.5 ns for cases 2-4, respectively. As can be seen, case 2 and 4 have the same actual read time due to the fact that the quartz is the same thickness and thus the separation between the shear waves will be the same. For this reason, to obtain the optimal read time and the maximum shear for the greatest amount of time, it is best to optimize for the quartz thickness along with the other parameters, where it appears that a taller target allows for a longer read time and a thicker quartz sample gives the largest separation between the two shear wave arrivals.

4.3.2.1 Checking Assumptions

As previously mentioned, the main assumptions of this experiment are that the second bounding plate remains elastic so that the in-situ shear stress at the sample-anvil interface can be found using the elastic wavespeed, and that the bounding plates have a higher impedance than the sample so that it can be subjected to a high strain-rate for a longer period of time. Furthermore, the YQ must

remain elastic since the two-wave structure breaks down above the elastic limit. For this reason, Equation 3.6.8 was used to find the maximum shear stress the bounding plates could support and Equation 2.1.68 was implemented to determine if the materials yielded. σ_Y^0 for the YQ is 5.17 GPa, found by using the Hugoniot Elastic Limit in [36] and Equation 2.1.71. For the WC, σ_Y^0 is 4.46 GPa [37]. The results of these calculations are shown in Figures 4.11a, 4.11b and 4.11c.

In Figure 4.11, a dotted line has been added for each material to illustrate where the region of time the QL wave occurs since it is the wave focused on for its higher shear value. The profiles were calculated for tracers within each material, hence the time discrepancy. In Figure 4.11a, it is evident that the YQ remains elastic for the region of interest. The WC driver, although it slightly yields in Figure 4.11b, remains elastic for the most part. The reason the stress increases is that there are wave reflections between the sample and the y-cut quartz. If yielding is a concern, a lower impact velocity can be chosen, but this is the lower range of the Caltech powder gun and hence poses a constraint. Furthermore, if this plate is still higher in impedance than the sample, it shouldn't affect the sample remaining at a high strain-rate level. Figure 4.11c shows that the WC backing remains elastic, which indicates that its elastic wavespeed can be used to find the shear stress. It can thus be assumed that both materials can be used for this experiment with an impact of 400 m/s.

The next assumption that must be checked is to make sure that the 1D strain with a superimposed shear stress assumption for the stress tensor is valid. In this case, the stress tensor is assumed to be

$$\sigma = \begin{bmatrix} \sigma_{xx} & 0 & \sigma_{xz} \\ 0 & \sigma_{yy} & 0 \\ \sigma_{xz} & 0 & \sigma_{yy} \end{bmatrix}, \tag{4.3.26}$$

where shear stress is now given by σ_{xz} rather than σ_{xy} in the stress tensor for the oblique wedge configuration in Equation 3.6.9. The reason for the shear being in this direction is due to the orientation of the y-cut quartz. Figure 4.13 shows the values of the stress tensor at various points in the configuration. The tracer location corresponds to that shown in Figure 4.12.

In Figures 4.13a-4.13c, it is clear that the assumptions made in the stress tensor in Equation 4.3.26 for stresses σ_{xx}, σ_{yy} and σ_{zz} coincide with the simulation, where σ_{yy} and σ_{zz} are equal. Figures 4.13d and 4.13f also support the hypothesis that the only shear is in the xz direction, which is shown in Figure 4.13e.

Since it has been demonstrated that the tensor assumed in Equation 4.3.26 holds true in the experiment, the stress path can be found as it relates to the yield surface as was done for the oblique

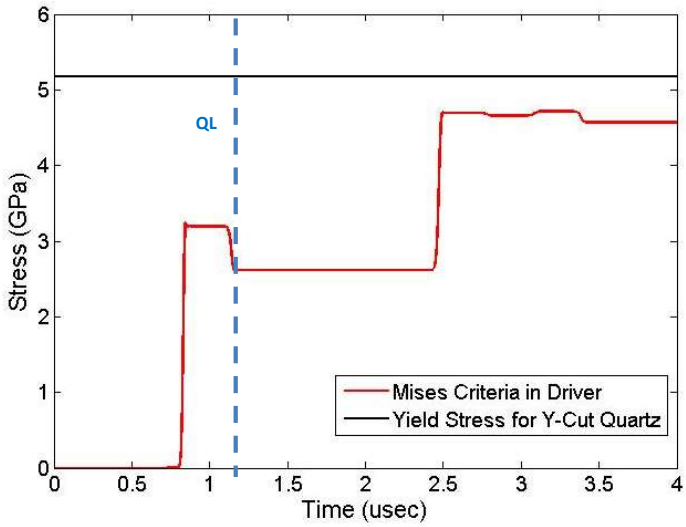

(a) YQ Driver.

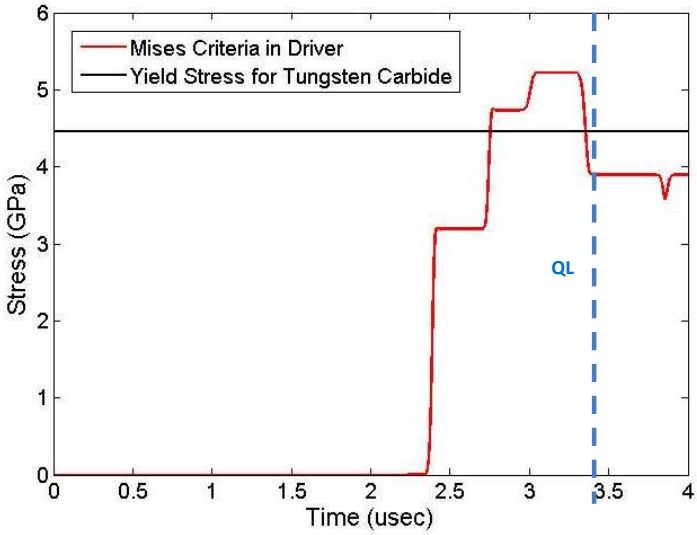

(b) WC Driver.

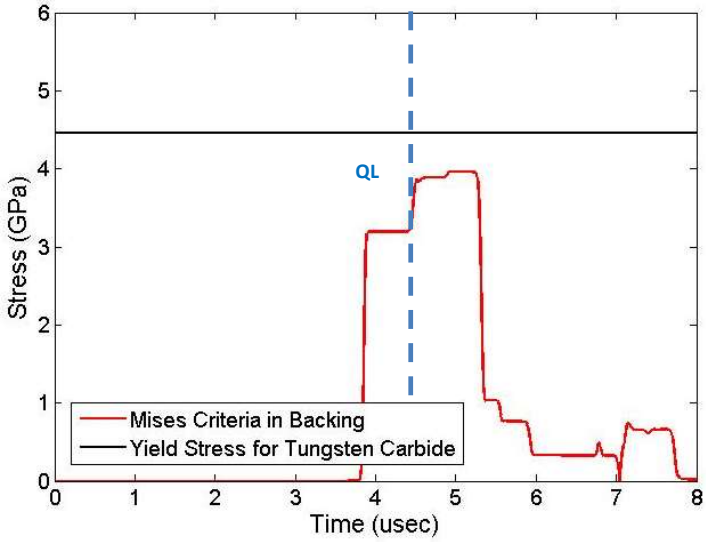

(c) WC Backing.

Figure 4.11: Von Mises criteria for the two drivers and backing plate in the y-cut quartz two driver sandwich configuration with maximum shear stress to determine if material is yielding.

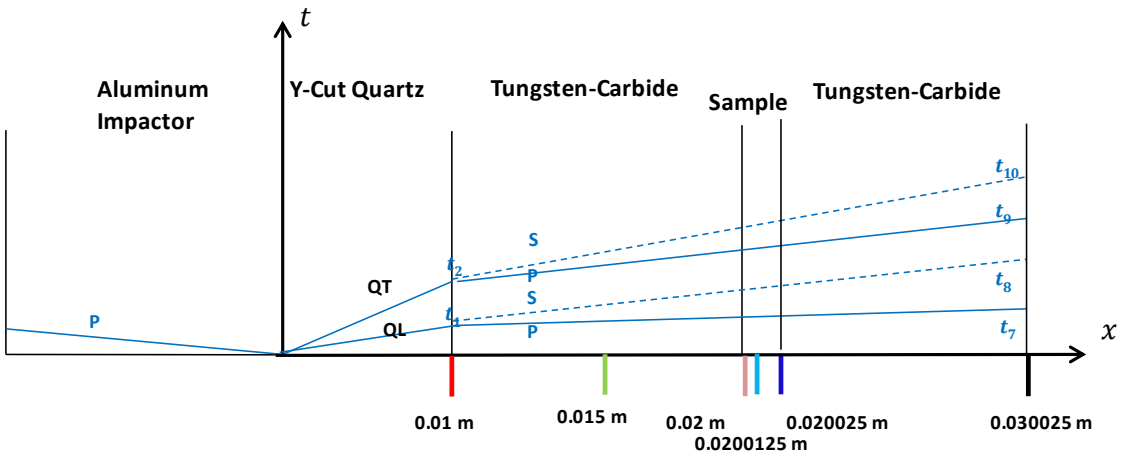

Figure 4.12: Tracer locations for two driver y-cut quartz sandwich configuration.

wedge configuration. Using the same approach as that used for Equation 3.6.10, it can be shown that

$$\sigma_{xz} = \frac{\sqrt{\sigma_Y^{0\,2} - (\sigma_{xx} - \sigma_{yy})^2}}{3}, \tag{4.3.27}$$

which is the equation for the yield surface. The stress path can then be found using the output from the stress tensor in the sample by plotting σ_{xz} as a function of $\frac{\sqrt{(\sigma_{xx}-\sigma_{yy})^2}}{3}$. The results of this calculation are shown in Figure 4.14.

In Figure 4.14, the stress path follows the yield surface until it ends up in a state of pure shear. Although this simulation assumes an elastic-perfectly plastic model, in a given experiment a different strength model can be used to model the setup that is strain-rate dependent, therefore, the material response at different pressures can be tested. The key here however, is that the sample is in pure shear for a large duration of the experiment. Assuming it follows the yield surface in a similar manner, it should reach its maximum shear value, which means that the transverse velocity could be used in conjunction with Equation 4.1.2 to find the maximum shear stress, from which the yield strength of the material can be calculated using Equation 3.6.8.

4.3.2.2 Calculating Strength, Strain-Rate, and Impactor Thickness

The predictions from the simulation can be used to show the feasibility of the experiment. As mentioned, the transverse velocity at the rear surface of the anvil can be used in Equation 4.1.2 to find the shear stress. Figure 4.15 shows the velocity profiles at the various tracers tracked in the simulation. In particular, the values at the WC driver-sample interface, at the sample-anvil interface

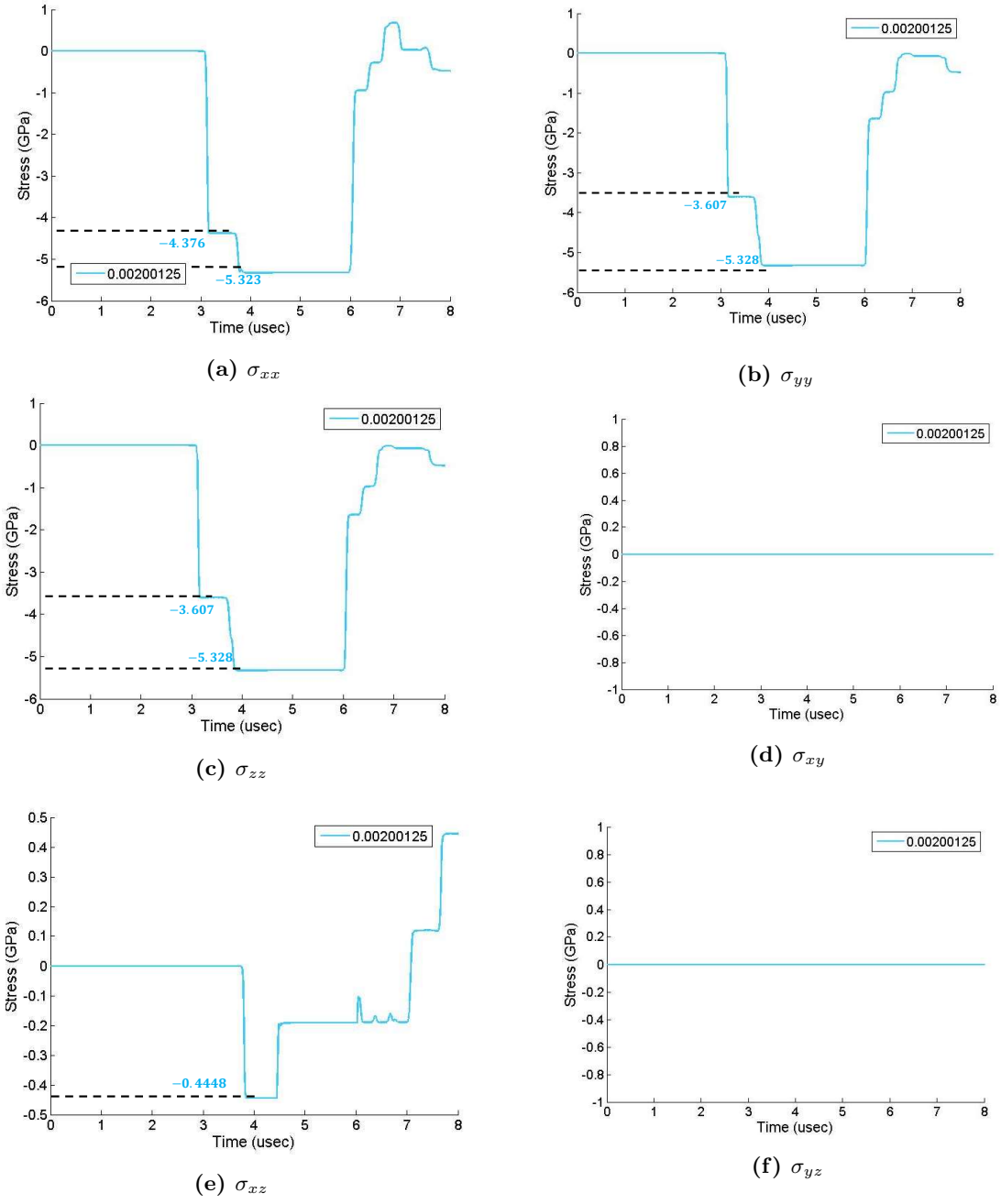

(a) σ_{xx}

(b) σ_{yy}

(c) σ_{zz}

(d) σ_{xy}

(e) σ_{xz}

(f) σ_{yz}

Figure 4.13: Outputs from the stress tensor for the y-cut quartz two driver sandwich configuration. Tracer taken midway through sample. Location of tracer in (m).

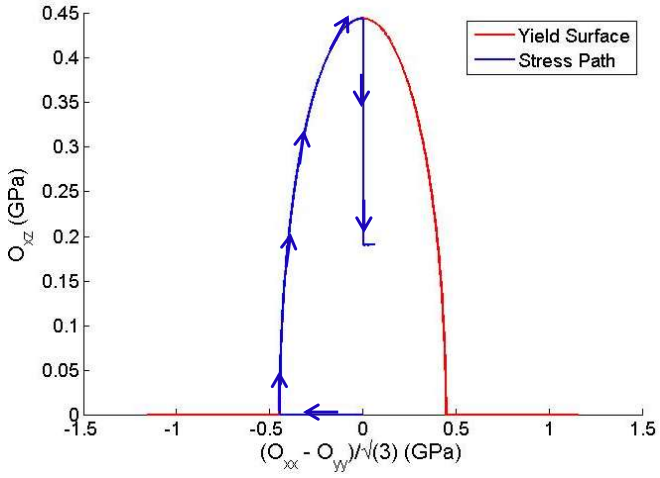

Figure 4.14: Stress path and yield surface for a tantalum sample in y-cut quartz two driver sandwich configuration.

and at the rear surface of the anvil are shown. The velocity at the back of the bounding plate, shown as 12.49 m/s in Figure 4.15, would correspond to what is measured in an experiment at the free surface. Thus, using this value in Equation 4.1.2 with density $\rho_{WC} = 15400$ kg/m^3 and shear wave velocity $C_S^{WC} = 4629.63$ m/s, it is found that the shear stress is equal to

$$\tau = \frac{1}{2}\rho_{WC} C_S^{WC} \mathbf{v_p} = 0.445 \text{ GPa}. \tag{4.3.28}$$

The maximum value in tantalum, with $\sigma_Y^0 = 0.77$ GPa, is 0.445 GPa which indicates that this experiment can be used to find the strength of the sample material.

The next calculation that can be made is for the strain-rate by using Equation 4.2.1 which gives

$$\dot{\gamma} = \frac{\mathbf{v_p} - \mathbf{v_p}}{h}. \tag{4.3.29}$$

In the Laslo simulation, the strain-rate was recorded at the tracer within the sample and is shown in Figure 4.16. From Figure 4.16, it is clear that the strain-rate given by the simulation is lower than that given by the velocity calculation, which gives 1.76 x 10^6/s, by a factor of 3.6. It is not clear at this time why the strain-rate calculated is lower than the simulation value, however, this is a question to be pursued in the future.

The final calculation that can be made is to ensure that the impactor is thick enough such that the reflection of the shock off its back surface does not reach the impact surface prior to the end of the experiment. Thus,

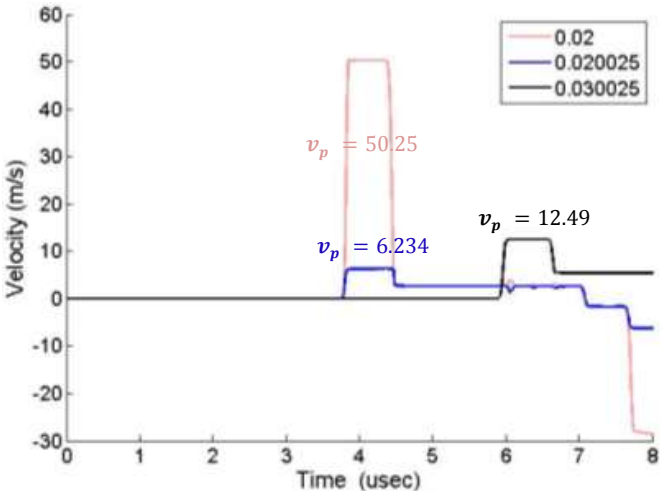

Figure 4.15: Transverse velocity at tracers throughout the y-cut quartz two driver sandwich configuration. Tracers locations are at the driver-sample interface (pink), sample-backing interface (blue), and rear surface of the backing (black). Tracer locations in legend are given in units of (m).

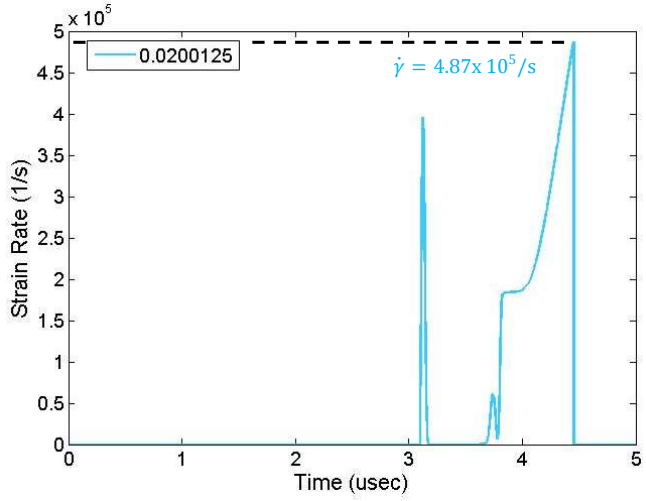

Figure 4.16: Strain-rate in tantalum target in two driver y-cut quartz sandwich configuration. Location given in legend in (m).

$$\frac{2d_{Al}}{U_S^{Al}} \geq t_4 + t_r, \tag{4.3.30}$$

where U_S^{Al} can be found by using the $U_S - u_p$ Hugoniot relation in 2.2.7, giving

$$U_S^{Al} = C_0^{Al} + S_{Al} u_p. \tag{4.3.31}$$

Since aluminum and y-cut quartz are well matched, this can be treated like a symmetric impact

problem where the particle velocity is just half of the impact velocity. Depending on the configuration used and the time of arrival of the first shear wave at the back of the bounding anvil, Equation 4.3.30 can be rearranged to solve for the dimension of the impactor.

4.3.3 One Driver Target Design

As can be seen in Table 4.3, the read times for the experimental setup are decent, however, an alternative method could be used to increase them. Height $d_H = 0.025$ m would be the largest that would fit into the chamber of the Caltech powder gun and thus the largest read time would be 447.80 ns for a quartz driver of 0.005 m thickness. This occurs after the second shear wave arrival, so the read time here would actually be smaller for the larger shear stress level. This driver could be increased in width, however, edge waves could soon pose to be an issue. An alternative approach is to eliminate the WC anvil driver.

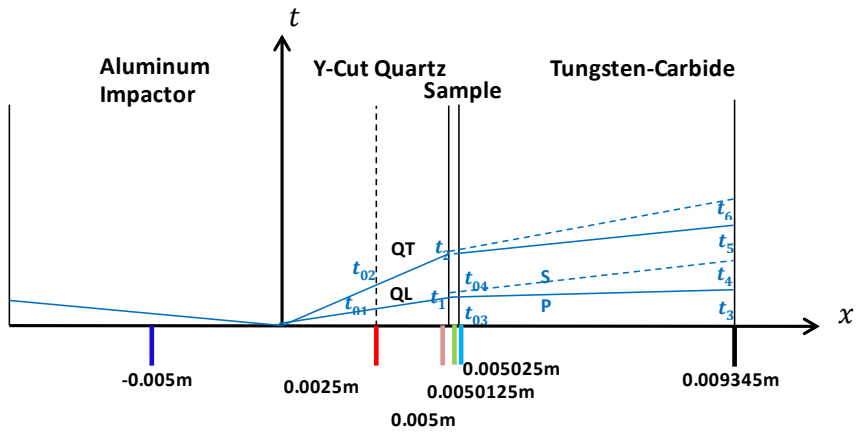

Figure 4.17: x-t diagram for y-cut quartz one driver sandwich configuration with tracers indicating where velocity profiles are read.

Figure 4.17 shows the x-t diagram for this configuration. Here, times t_{01} and t_{02} indicate the arrival of QL and QT, respectively, midway through the quartz, which are used to find the velocities of these waves. Times t_1 and t_2 correspond to the arrival of QL and QT, respectively, at the front face of the sample, times t_{03} and t_{04} coincide with the arrival of the pressure and shear waves, respectively, at the interface of the sample and WC. Times t_3, t_4, t_5, and t_6 correspond to the arrivals of the first longitudinal and transverse waves and the second longitudinal and transverse waves, respectively, at the rear surface of the bounding anvil. This simulation was conducted for a 450 m/s impact due to concerns that at 500 m/s the YQ might yield. The dark blue tracer is midway through the aluminum impactor, the red tracer is midway through the quartz, the pink

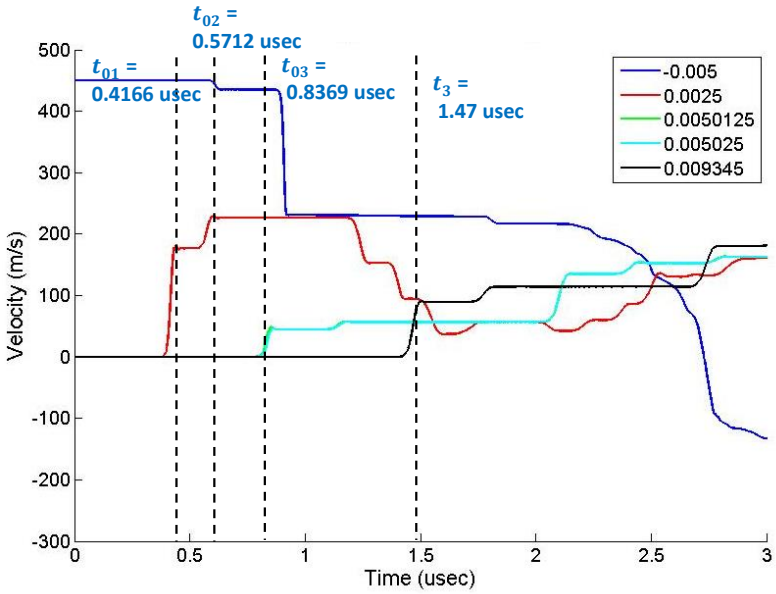

(a) Longitudinal velocity profile.

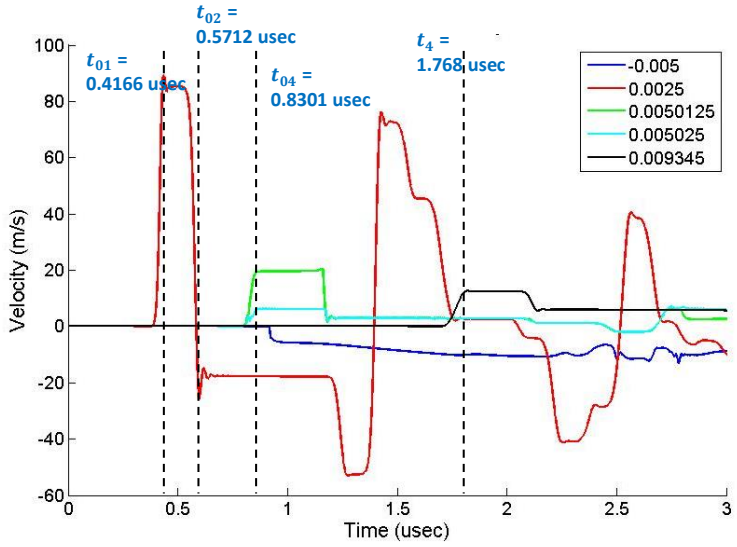

(b) Transverse velocity profile.

Figure 4.18: Longitudinal and shear particle velocities for y-cut quartz one driver sandwich configuration. Tracer locations are given in (m) for tracers midway through the impactor (dark blue), midway through the quartz driver (red), midway through the sample (green), at the sample-backing interface (light blue), and at the backing anvil rear surface (black).

tracer is at the YQ-sample interface, the green tracer is midway through the sample, the light blue tracer is at the sample-WC interface, and the black tracer is at the rear surface of the bounding anvil.

Once again, the arrival times of each wave, shown in Figure 4.18, can be used to find the wave velocities in each material. Using the red tracer, the outputs of which are shown in Figures 4.18a-4.18b, it is found that the wave velocities in the quartz are

$$C_{QL}^{YQ} = \frac{0.0025 \text{ m}}{t_{01}} = 6000.96 \text{ m/s} \tag{4.3.32}$$

and

$$C_{QT}^{YQ} = \frac{0.0025 \text{ m}}{t_{02}} = 4376.75 \text{ m/s}. \tag{4.3.33}$$

These velocities are slightly different than those in the 400 m/s impact due to the increased impact velocity. The velocities for the first pressure and shear waves, which should be the same for the second two waves since the WC should remain elastic, are

$$C_{L}^{WC} = \frac{0.009345 \text{ m} - 0.005025 \text{ m}}{t_3 - t_{03}} = 6823.57 \text{ m/s} \tag{4.3.34}$$

and

$$C_{S}^{WC} = \frac{0.009345 \text{ m} - 0.005025 \text{ m}}{t_4 - t_{04}} = 4606.03 \text{ m/s}, \tag{4.3.35}$$

respectively. Once again, these are slightly different than the velocities found in Equations 4.3.9 and 4.3.10, however, this could be due to what point in the wave profile the arrival time was chosen. These velocities are also fairly close to those given by Frutschy and Clifton [37] where for pure WC, $C_L^{WC} = 6858$ m/s and $C_S^{WC} = 4300$ m/s.

Using the same approach as that for the two driver configuration, the edge waves are first analyzed, shown in Figure 4.19. At the YQ-sample interface, the time it takes for the edge waves to travel to diameter d_1 is

$$\frac{d_{YQ}\sqrt{2}}{C_{QL}^{YQ}}. \tag{4.3.36}$$

Since the sample is so thin, it is assumed that the waves travel at the same velocity through the sample as they do in the WC backing plate. Thus, the time for the edge waves to travel from

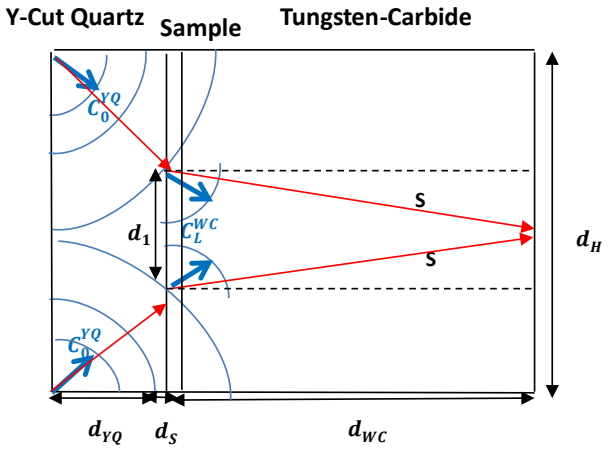

Figure 4.19: Edge wave diagram for y-cut quartz one driver sandwich configuration.

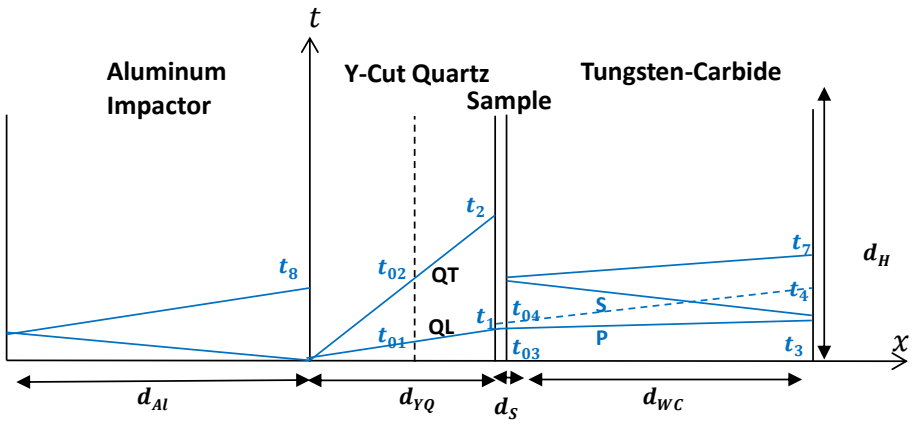

Figure 4.20: x-t diagram for y-cut quartz one driver sandwich configuration with a focus on the first shear wave resulting from the QL wave in the quartz.

diameter d_1 to the point of observation at the rear surface of the target is

$$\frac{\sqrt{(DWC)^2 + \left(\frac{d_1}{2}\right)^2}}{C_L^{WC}}. \tag{4.3.37}$$

In this equation, $DWC = d_{WC} + d_S$. At time t_4, shown in Figure 4.20, when the shear wave reaches the back surface of the anvil, a certain amount of time t_r should be allotted for the data to be collected before the edge waves set in. This consideration results in the following constraint

$$t_4 + t_r = \frac{d_{YQ}\sqrt{2}}{C_{QL}^{YQ}} + \frac{\sqrt{(DWC)^2 + \left(\frac{d_H - 2d_{YQ}}{2}\right)^2}}{C_L^{WC}} = \frac{d_{YQ}}{C_{QL}^{YQ}} + \frac{DWC}{C_S^{WC}} + t_r, \tag{4.3.38}$$

Case	$\mathbf{d_{YQ}}$ (m)	$\mathbf{d_H}$ (m)	$\mathbf{d_S}$ (μm)	$\mathbf{t_r}$ (ns)	$\mathbf{d_{WC}}$ (mm)	$\mathbf{t_4}$ (μs)	$\mathbf{t_6}$ (μs)
1	0.01	0.025	25	623.59	2.81	2.82	2.90
2	0.005	0.025	25	786.58	3.55	1.61	1.92
3	0.015	0.05	25	1288.42	7.1	4.05	4.97
4	0.02	0.05	25	1255.62	5.65	4.56	5.80

Table 4.4: Calculated read time, t_r, and tungsten carbide (WC) thickness for y-cut quartz one driver sandwich configuration. d_{YQ} is the thickness of the y-cut quartz, d_H is the height of the target, d_S is the sample thickness, d_{WC} is the thickness of the tungsten carbide, t_4 is the arrival of the first shear wave at the rear surface of the target, and t_6 is the arrival of the second shear wave at the rear surface of the target.

where it was used that $d_1 = d_H - 2d_{YQ}$ and $t_4 = \frac{d_{YQ}}{C_{QL}^{YQ}} + \frac{DWC}{C_S^{WC}}$. This is the same Equation as 4.3.17 and hence Equations 4.3.18-4.3.20 can be used to solve for DWC. As mentioned above, the sample should be in compression for shear to be transmitted and thus the experiment must take place before the L wave from the rear surface of the anvil reflects, hits the target and then travels back to the rear surface of the bounding plate at time t_7, shown in Figure 4.20. This results in the following stipulation

$$t_7 = t_3 + 2\frac{d_{WC}}{C_L^{WC}} = \frac{d_{YQ}}{C_{QL}^{YQ}} + \frac{DWC}{C_L^{WC}} + 2\frac{d_{WC}}{C_L^{WC}} \geq t_4 + t_r. \tag{4.3.39}$$

Plugging in for times t_3 and t_4 in terms of the lengths and wave velocities and rearranging for DWC results in

$$DWC = \frac{t_r + 2\frac{d_S}{C_L^{WC}}}{\frac{3}{C_L^{WC}} - \frac{1}{C_S^{WC}}}. \tag{4.3.40}$$

In Equation 4.3.39, the $\geq$ sign was set to equal the quantity on the right to solve for the worst case scenario. Since YQ and aluminum 6061-t6 are well matched, the L wave reflecting off of the front surface of the target is not of concern when it hits the YQ-aluminum interface (as it was in the two driver configuration for the reflection off of the YQ-WC interface). Thus, Equations 4.3.38 and 4.3.40 can be used to solve for the read time and anvil thickness by varying the height of the target, quartz thickness and sample thickness. The summary of these results is given in Table 4.4. Again, the shortest arrival time between the edge waves and the arrival of the reflected L wave from the rear surface of the anvil back to the target was selected, from which the shear wave arrival at the anvil back surface was subtracted to find the actual read time due to the rounding off of the thickness of the WC.

In Table 4.4, the analyzed YQ was thicker for the taller targets in cases 3 and 4 to see if the read

time would be increased from the two driver design. As can be seen in Table 4.4, the read times are much larger for this configuration especially where the YQ is thicker, but once again the second shear wave will hit the rear surface of the anvil during the read time. This is in fact the case for all of the configurations, where the read time between the two shear wave arrivals will be 618.4 ns for the first case, it will be 309.20 ns for the second case, and it will be 927.6 ns and 1236.80 ns for the last two cases, respectively. Thus, to increase the read time of the experiment, the YQ driver plate can be made thicker, which seems to work well, however, only to a certain extent. In Table 4.4, case 4 has a thicker quartz driver than case 3, which has the same height of the target, however, their read times are about the same (ignoring when the shear wave arrives). The advantage here to making the quartz thicker is that the time between shear wave arrivals is larger, but it appears that the read time prior to edge wave arrival or decompression of the specimen decreases. Overall, it is clear that both quartz thickness and the height of the target can also be altered, depending on the dimensions of the loading system. By altering the target parameters, the experiment can be optimized for a larger read time at the higher level of shear stress observed for the first shear wave.

4.3.3.1 Checking Assumptions

Once again the driver and backing need to be checked to make sure that they remain elastic throughout the experiment. Equation 3.6.8 was again used to find the maximum shear stress and Equation 2.1.68 was implemented to determine if the materials yielded. The analysis was run for a case where the sample, polyurethane, had a lower impedance than the y-cut quartz and for a sample made of tantalum, with a higher impedance to see if it was necessary to have a lower impedance material as in the oblique gun experiments. The results of these calculations are shown in Figures 4.21a, 4.21b, 4.21c, and 4.21d.

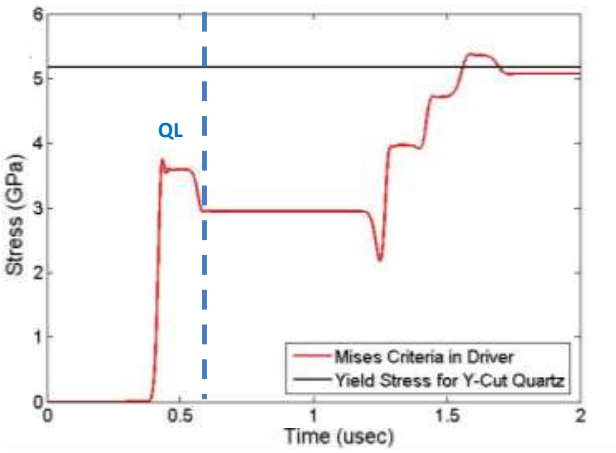

(a) YQ Driver Polyurethane Sample.

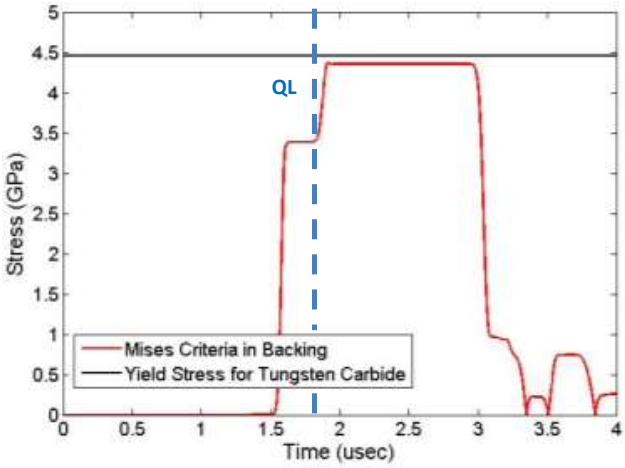

(b) WC Backing Polyurethane Sample.

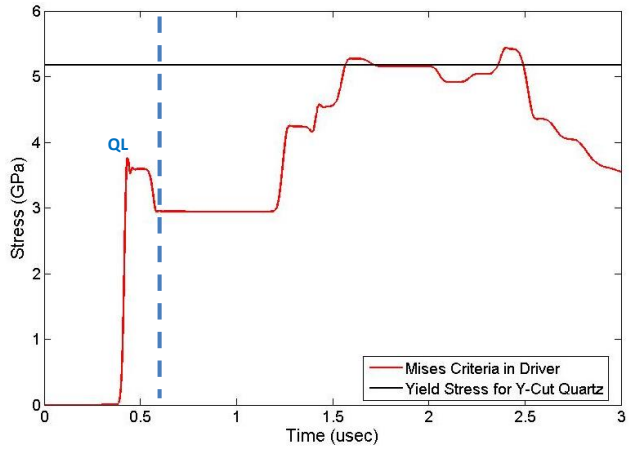

(c) YQ Driver Tantalum Sample.

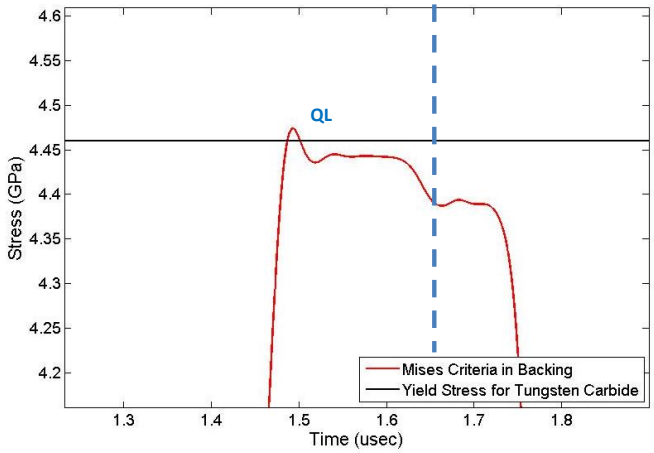

(d) WC Backing Tantalum Sample.

Figure 4.21: Mises criteria for driver and backing in y-cut quartz one driver sandwich configuration for a tantalum and polyurethane sample with maximum shear stress to determine if material is yielding.

From Figures 4.21a and 4.21b, it is clear that both the driver and backing remain elastic for the polyurethane sample. The same is mostly true for the tantalum sample in Figures 4.21c and 4.21d however, the WC slightly yields for a short period of time. Since it falls below the Mises criteria for most of the simulation, it can be utilized for both materials with an impact of 450 m/s. If the yielding of WC at the very beginning of the simulation is of concern, the impact velocity can be lowered.

Once again, the 1D strain with superimposed shear stress assumption must be checked. This tensor is defined in Equation 4.3.26. The tracer locations correspond to those shown in Figure 4.17. In Figures 4.22a-4.22c, it is clear that the assumptions made in the stress tensor in 4.3.26 for stresses σ_{xx}, σ_{yy} and σ_{zz} agree with the simulation, where σ_{yy} and σ_{zz} are equal. There is a slight difference

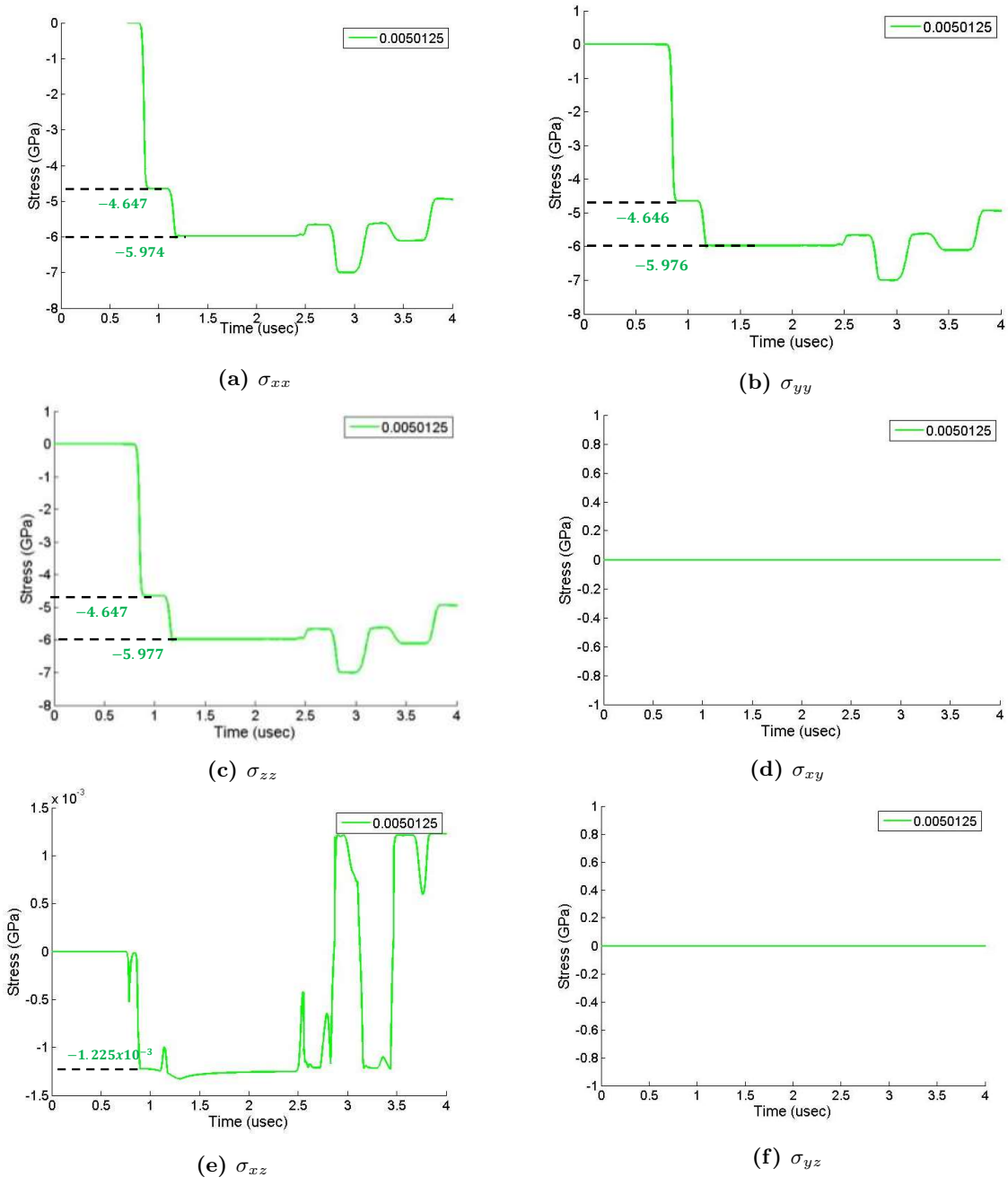

Figure 4.22: Outputs from the stress tensor for the one driver y-cut quartz sandwich configuration. Tracer taken midway through the polyurethane sample and shown in units of (m).

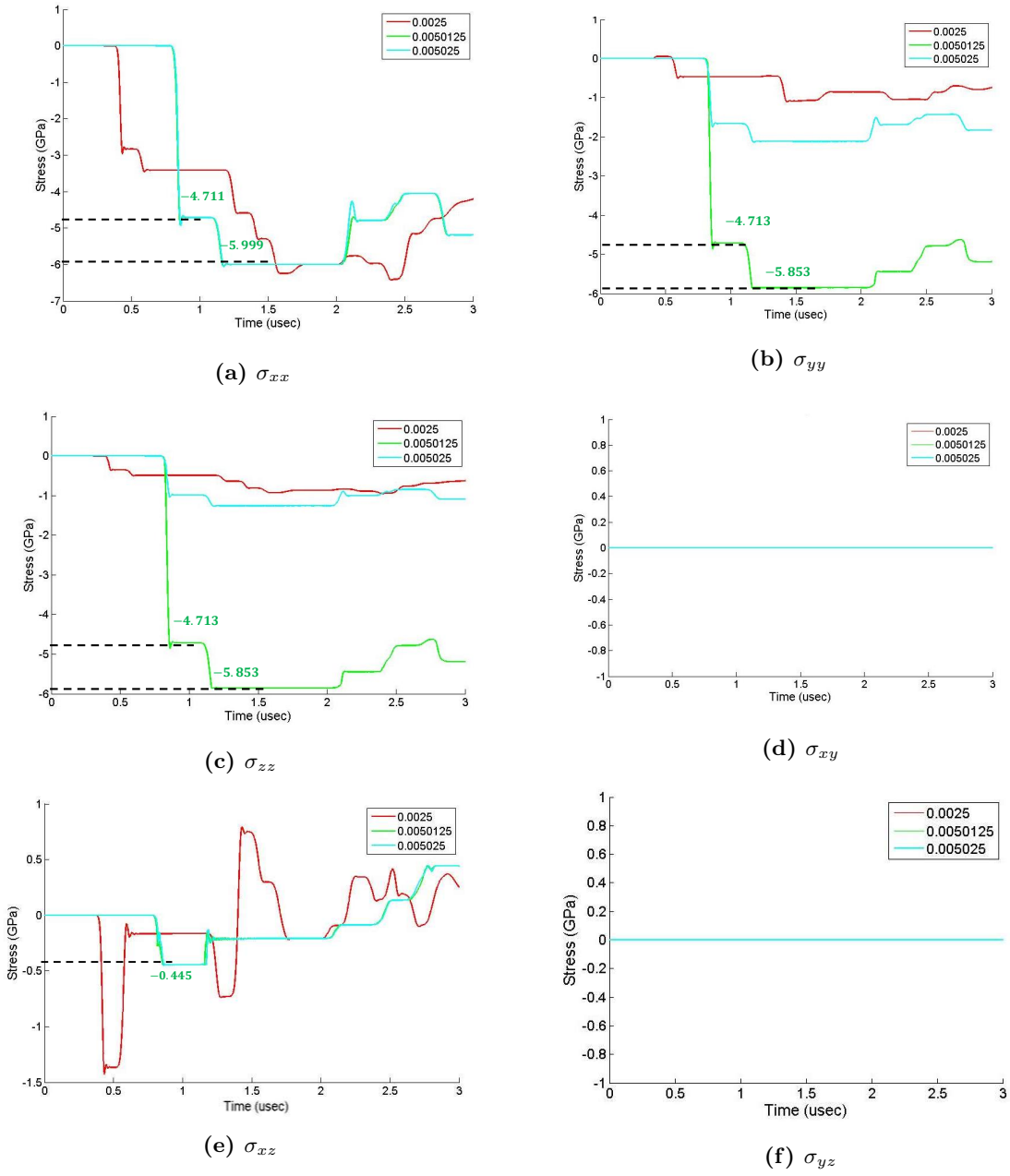

(a) σ_{xx}

(b) σ_{yy}

(c) σ_{zz}

(d) σ_{xy}

(e) σ_{xz}

(f) σ_{yz}

Figure 4.23: Outputs from the stress tensor for the one driver y-cut quartz sandwich configuration. Tracers taken midway through the driver (red), midway through the tantalum sample (green) and at the sample-backing interface (light blue) and are shown in units of (m).

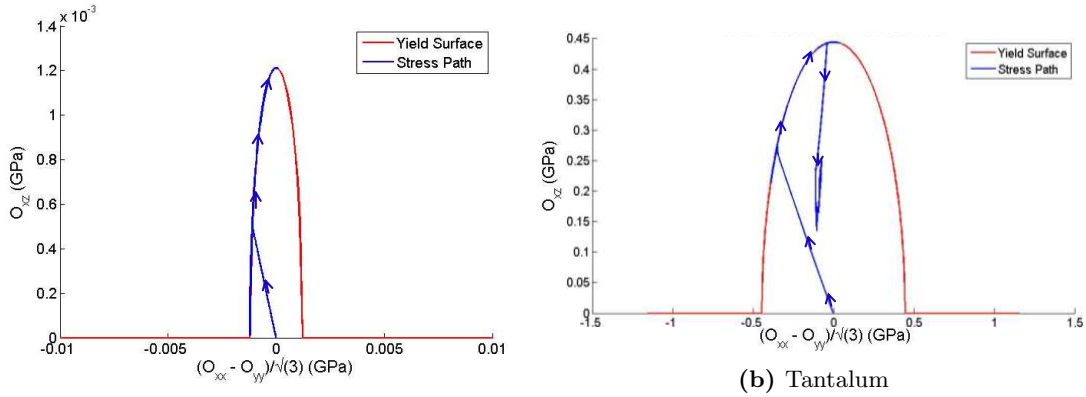

(a) Polyurethane

(b) Tantalum

Figure 4.24: Stress path and yield surface for tantalum and polyurethane samples in the one driver y-cut quartz sandwich configuration.

between the two however, it is by only 0.1%. It is also interesting to note that σ_{xx} is also equal to σ_{yy} which coincides with the hydrodynamic assumption commonly used for shock waves. Figures 4.22d and 4.22f also coincide with the assumption that the only shear is in the xz direction, which is shown in Figure 4.22e. Interestingly enough, the case with the higher impedance sample also falls within the assumptions of the stress tensor, as can be seen in Figure 4.23. Here the shear stress is much larger than for the polyurethane configuration.

Now that the assumptions have been shown to hold for the stress tensor, the stress path vs. yield surface can be found using Equation 4.3.27 and the approach for the two driver target described in Section 4.3.2.1. The calculations for the two samples are shown in Figures 4.24a and 4.24b. For both cases in Figures 4.24a and 4.24b, the stress path ends up in a state of pure shear at the highest value of shear stress. Once again, it is interesting to note that, although tantalum has a higher impedance than y-cut quartz, it too reaches a state of maximum shear at the highest value of shear in the simulation. These results indicate that both samples could potentially be used in the one driver y-cut quartz sandwich configuration to find the strength of each material.

4.3.3.2 Calculating Strength, Strain-Rate, and Impactor Thickness

To find the strength of the material, the transverse velocity at the rear surface of the anvil backing must be found. Figures 4.25a and 4.25b show the velocities for the polyurethane and tantalum samples with the color of the tracer corresponding to the position of the tracers in Figure 4.17. The only difference in positions is for the polyurethane configuration, which has a wider backing and hence has the rear surface tracer located at 0.015025 m in the simulation. As can be seen, only the velocities at the sample-backing interface and the backing rear surface were shown

for both materials. The reason for this is that these velocities are much smaller than the shear velocities throughout the remainder of the target and hence it is easier to see them without the other data. The velocities in the polyurethane example are much smaller than the tantalum setup due to the large impedance mis-match between polyurethane and tungsten carbide, where the shear impedances are 1.302 x 10^6 kg/m^2/s [60] and 66.22 x 10^6 kg/m^2/s [37], respectively. Using Equation 4.1.2 with density $\rho_{WC} = 15400$ kg/m^3, shear wave velocity $C_S^{WC} = 4606.03$ m/s found above, and rear surface velocity 0.0343 m/s for the polyurethane, it is found that the shear stress is,

$$\tau = \frac{1}{2}\rho_{WC} C_S^{WC} \mathbf{v_p} = 1.21 \text{ MPa}. \tag{4.3.41}$$

The maximum value in polyurethane, with $\sigma_Y^0 = 2.1$ MPa, is 1.21 MPa which indicates that this experiment can theoretically be used to find the strength of the sample material. Unfortunately, the velocity observed is quite low and hence a backing with a lower impedance would be recommended for practical purposes. For the tantalum case, the rear surface velocity 12.55 m/s can be used with Equation 4.3.41 to get 0.445 GPa, where the maximum value is $\frac{\sigma_Y^0}{\sqrt{3}} = 0.445$ GPa. Once again, this result shows that this experiment could be implemented as a method to measure the strength of tantalum.

Next, the strain-rate can be found from the velocity difference between the two sides of the target using Equation 4.2.1. The velocity at the y-cut quartz-polyurethane interface, shown in Figure 4.17 at 0.005 m, is 211.6 m/s. This is the velocity profile after reflection at the y-cut quartz-sample interface which is different than the in-situ velocity in the quartz. The velocity at the rear surface of the sample is shown in Figure 4.25a as 0.0171 m/s — or half of the backing rear surface velocity. The sample is 25 μm thick which gives a strain rate of 8.46 x $10^6/s$. For the tantalum sample, the velocity at the front of the tantalum sample is 174.5 m/s, the velocity at the back surface is 6.241 m/s and the thickness is the same resulting in a strain-rate of 6.73 x $10^6/s$. The strain-rate in the target was found from the Laslo simulations and is shown in Figure 4.26. As can be seen, the strain-rate for the polyurethane sample is 5.742 x $10^6/s$ according to the simulation, which is on the same order of magnitude as that given by the velocity difference calculation, but it is still off by a a factor of 1.17. For the tantalum sample, the strain-rate is found as a factor of mesh size. It appears that with increasing mesh size, the strain-rate is larger, but still differs from the calculated value. Something else to note is that the strain-rate drops, but then stays at an elevated value for a while in the polyurethane as it would in an oblique gun experiment due to the reverberations of the shear wave inside the lower impedance sample. Although the value of the strain-rate itself

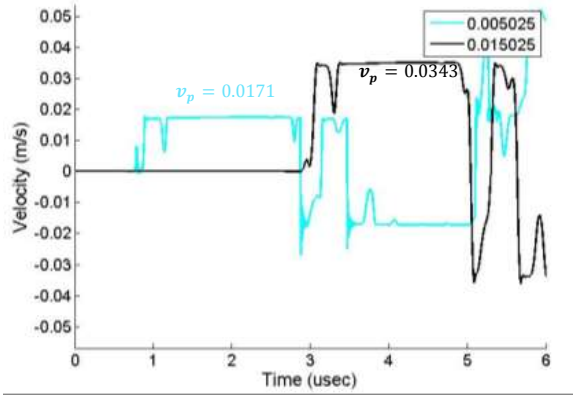

(a) Polyurethane

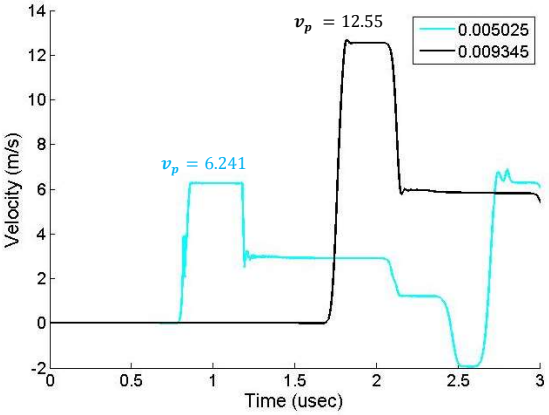

(b) Tantalum

Figure 4.25: Transverse velocity at tracers throughout the one driver y-cut quartz sandwich configuration for polyurethane and tantalum samples. Tracers given at the sample-backing interface (light blue) and at the rear surface of the backing (black). Tracer locations shown in (m).

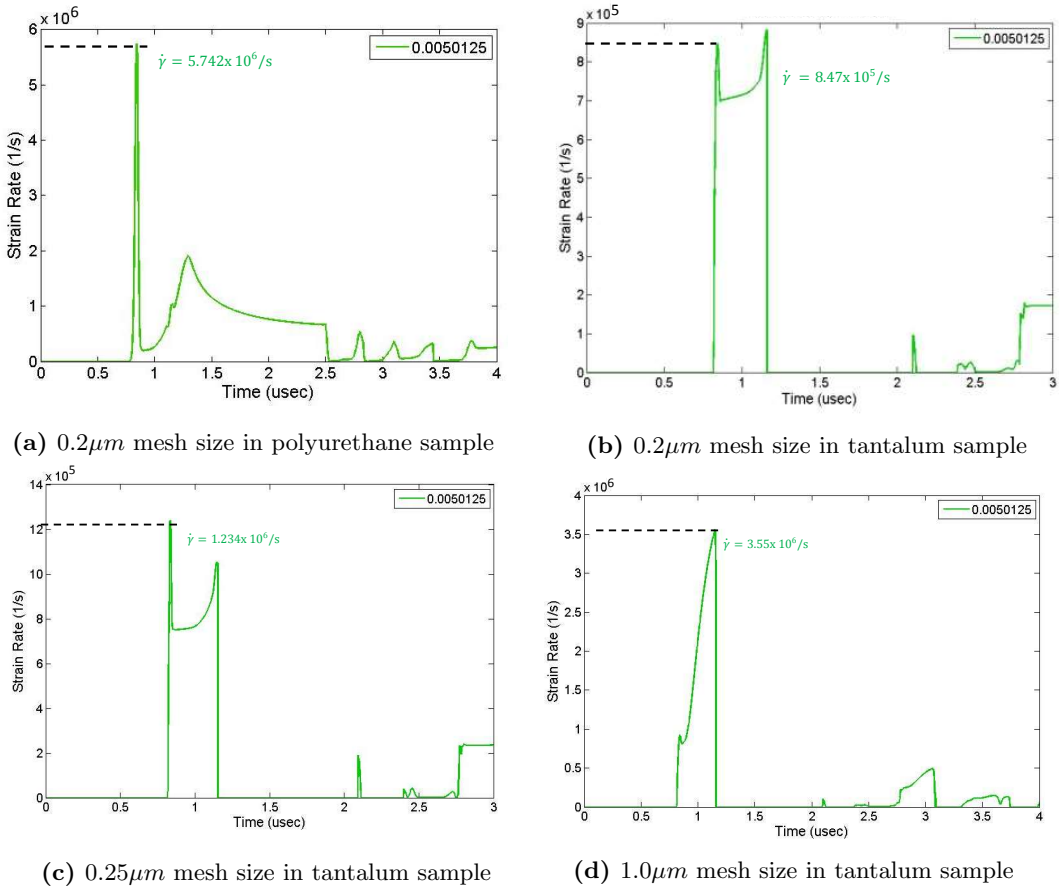

(a) $0.2\mu m$ mesh size in polyurethane sample

(b) $0.2\mu m$ mesh size in tantalum sample

(c) $0.25\mu m$ mesh size in tantalum sample

(d) $1.0\mu m$ mesh size in tantalum sample

Figure 4.26: Strain-rate in polyurethane and tantalum samples in one driver y-cut quartz sandwich configurations. Tracer shown in (m).

could be mesh dependent, it does appear that the strain-rate is closer to being constant for a larger portion of time for the lower impedance polyurethane sample. At this point, it is not clear why the strain-rate behaves so differently for the various mesh sizes and why the velocity calculation differs from the simulation value, however, this is a question to be pursued in the future and could be due to the complexities of using y-cut quartz as a driver material and the reflections that occur at the driver-sample interface. In practice, to calculate the strain-rate, the front surface velocity could be found by using a simulation since it would be difficult to measure in an experiment. This value would be combined with the rear surface measurement on the anvil to find the strain-rate.

The final calculation to be made is for the impactor thickness and the same approach described in Equations 4.3.30-4.3.31 can be used.

4.4 Limitations

4.4.1 CTH Simulations

Although Laslo captures the one dimensional effects of the wave propagation in both the two driver and one driver y-cut quartz sandwich configurations, it does not definitively analyze the edge wave effects. The methodology described above is only an estimate. Unfortunately, CTH hydrocode, which does model two dimensional configurations, does not have a model for y-cut quartz. For this reason, the one dimensional analysis with estimation of edge effects can be used. Other numerical codes can also be implemented to mitigate this problem.

4.4.2 Slip

In y-cut quartz there are two waves (QL and QT) and both waves have longitudinal and transverse components. As seen in the simulations, the QL wave will apply some shear at exactly the same time it applies the longitudinal compression and this value cannot be increased by varying the angle of impact, as it can be in an oblique gun experiment. Therefore, the benefit of the increased longitudinal compression in resisting the shear wave is not seen. This is why it is difficult to transmit shear at the quartz-sample interface. Furthermore, the harder the quartz is hit by the flyer, the larger the component of shear and the greater the chance of slipping. The most shear observed to be transmitted has been 0.35 GPa [75]. Nevertheless, epoxy was previously used with a mixture of diamond particles between the quartz and specimen and it is anticipated that by binding the sample directly to the quartz by depositing epoxy on the outer edges of the two materials, rather than between them, and lapping the quartz to a smooth surface, more shear will be transmitted. See Section 7.2 for more detail.

4.4.3 Impact Velocity

As with the oblique gun experiments, the higher the impact velocity, the larger the amplitude of the incoming wave. If the stress level is low enough for the material to remain elastic, the shear stress in the sample "rings up" to the level of the shear stress in the incident wave. Higher impact velocities will result in a difference in transverse velocities at the back and front surfaces of the sample and hence a strain-rate can be observed with consequently larger plastic strains for the same pulse duration at even larger impact velocities. At this point the shear stress in the sample depends on the flow stress and strain-rate [76]. Nevertheless, as long as the backing anvil remains elastic, the

traction on the interface between the sample and the anvil will be measured. Furthermore, as long as the quartz remains elastic, the two-wave structure will be seen. Thus, the impact velocity can be increased until a level is reached at which the quartz and backing anvil are no longer elastic.

4.4.4 Two Drivers vs. One Driver

In the above simulations, it is evident that the one driver sandwich configuration exhibits a longer read time than the two driver approach. Although using the one driver approach with the y-cut quartz as the upstream bounding plate works for a variety of materials, the backing material must be chosen carefully such that it remains elastic and has a low enough impedance that the transmitted shear velocity is observable. Alternatives would be to use different anvils such as Ti6Al4V or Tool Steel, which are lower impedance materials, and to use a much lower impact velocity. The one-driver configuration will also not work for an aluminum sample since it is well matched to the y-cut quartz and hence there would not be any reverberations between the two bounding plates. Another concern is that it is difficult to extract the front surface velocity for the sample since reflections at the rear surface of the quartz are quite complex. To measure strain-rate, simulations would need to be conducted to find the front surface velocity such that it could be combined with the velocity measured at the anvil rear surface. If using the two driver approach, more analyses would need to be conducted to find if varying the quartz thickness and target height would help increase the read time.

4.5 Conclusions

It has been shown that the y-cut quartz sandwich configuration can be used in a manner similar to oblique gun experiments, but with a normal impact gun, which is advantageous since the latter setup is more prevalent. Although both the two driver configuration consisting of the quartz plate and an anvil or the one driver with only the quartz plate can be implemented, using only one driver allows for a longer read time. It also appears that increasing quartz thickness can lead to a longer read time in both setups. With both experimental setups, transverse velocity can be measured and used to find the maximum shear stress the sample is subjected to and thus the yield strength of it. The drawbacks to this configuration are that only a certain pressure can be attained since the larger the longitudinal stress the larger the shear stress generated by the quartz, which results in the sample slipping. Likewise, as the impact velocity is increased, the quartz and backing anvil

begin to yield, which will lead to the breakdown of the two-wave structure in the quartz and the inability to use the elastic properties in the anvil to calculate shear stress in the sample. Though there are limitations, this technique has promise as a method of finding the strength of a material with a normal impact configuration and experiments must be conducted for both the two driver and one driver setups to study the results and compare them to the 1D simulations. Further analysis must also be performed to determine if the velocity difference approach to finding the strain-rate is indicative of the actual strain-rate in the target.

Chapter 5

Loading Systems and Diagnostics

5.1 Loading Systems

The loading technique considered here is the plate impact experiment, performed using gas or powder guns. In this type of experiment, a cylindrical plate is propelled by either high pressured gas or gun powder at which point it impacts a cylindrical target of interest. This impact produces waves in both the impactor and target. These types of experiments study the Hugoniot of the material, spallation, phase changes, etc., and are used here to study shear response.

5.1.1 Caltech Single Stage Powder Gun

The propellant gun at Caltech, shown in Figure 5.1, is a high velocity planar impact loading system consisting of a 3 meter long launch tube with a 36 mm diameter bore. Impact velocities range between 400-2000 m/s and can be adjusted by the powder to sabot ratio, given by

$$\frac{Powder}{Sabot} = 0.2799V^2 + 0.0583, \tag{5.1.1}$$

where $\frac{Powder}{Sabot}$ is a mass ratio and V is the impact velocity [78]. When an experiment is set to be performed, a solenoid is used to fire the projectile. The solenoid, made by McMaster Carr, is powered by 120 V of AC power. When the powering circuit closes upon pressing the firing switch, the solenoid shaft pushes against a trigger pin. This pin is a tapered cylindrical rod made from 4340 steel and has a 1.8 mm diameter hole drilled 19 mm deep where a gauge steel pin fits. Upon firing, this steel pin protrudes enough to indent the primer of a bullet by 0.6-0.8 mm. As the volume of the primer reduces, it burns and produces a high temperature and pressure gas flame that ignites 3 g of 2400 handgun powder encased in the brass cartridge surrounding the primer. This powder produces

an even hotter flame which travels into a hollow Vascomax C-300 maraging steel cylindrical tube called a flame splitter that uniformly distributes the flame. The flame splitter contains 16 holes that are evenly distributed in a 45 degree spiral which causes up to 50 g of H4198 smokeless rifle powder surrounding this tube, in a device called the breech, to ignite uniformly [78]. The high pressure and temperature gas in the breech exerts considerable force on a nylatron sabot that is sealed in front of the breech in the launch tube. This sabot consists of small steps with increasing diameter and a final stop ring that is seated in the barrel. The steps increase in diameter and form a uniform seal between the breech and launch tube. The gas builds up uniformly behind the sabot due to the angled and then planar surface at the breech end. Once enough pressure builds up, the stop ring is broken and the sabot propels down the barrel. The impact face of the sabot contains counterbores where the flyer is glued. An air gap is created between the flyer and sabot due to the sabot design which allows for the formation of a well characterized release wave at the rear surface of the impactor. An image of the sabot is shown in Figure 5.2.

Figure 5.1: Caltech single stage powder gun.

The target is mounted to a target holder, bolted 25.4 mm away from the barrel end in the vacuum chamber such that, as the impactor hits it, part of it remains in the barrel in order to avoid tilt. This

(a) View at the breech end. **(b)** View at the impact side.

Figure 5.2: Nylatron sabot used to launch projectiles at Caltech powder gun facility.

positioning also blocks the high pressure gas from disturbing the target. The chamber is evacuated to approximately 28 inHg gauge pressure. To measure the velocity of the impactor, several methods are implemented. The first is the light interruption system, shown in Figure 5.3. In this diagnostic, fiber optic cables are mounted onto the gun barrel via a "barrel extension" which attaches to the end of the barrel. On one side, white light is directed into two cables where it is then collected by another set of two cables on the other side of the barrel. This set is connected to photodiodes that turn on when light is received and turn off as the projectile travels down the gun barrel and blocks the emitted light. When the first diode is turned off, a signal is sent to the oscilloscope to start recording; this records the second signal as well. The time interval between these two signals along with the 40.35 mm separation between the two sets of fibers is used to find the velocity. The second method to measure velocity is by using shorting pins. Electric shorting pins, purchased from Dynasen (CA-1038), short upon impact due to the closure of a gap between the outer conductive casing and a central insulting pin. A pin mixer is used to provide a signal for the pins and after the pins short, this signal is sent to the oscilloscope. By staggering the pins in height from the impact surface, the impact time of each pin and the distance between each pin height can be used to calculate impactor velocity. The final method of velocity measurement is to use a fiber optic probe with a VISAR, much like the observation of the rear surface of a target.

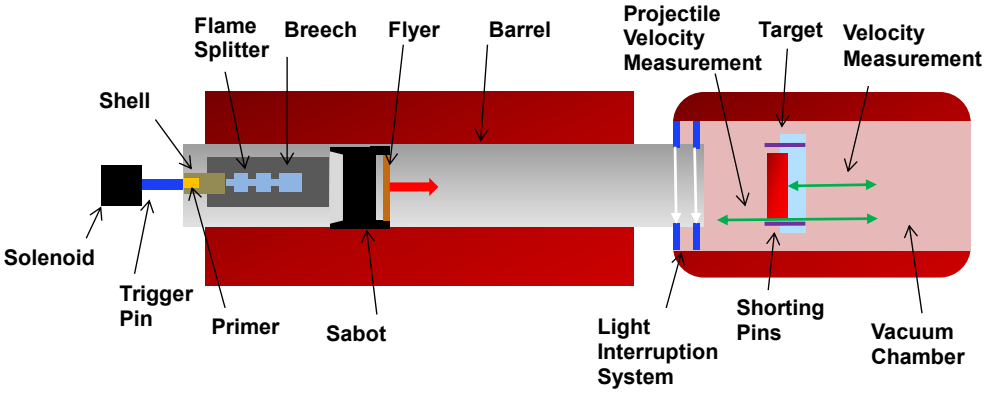

Figure 5.3: Schematic of Caltech single stage powder gun and components during an experiment. Upon pressing a trigger, the solenoid fires and indents the primer. This ignites 2400 handgun powder, which creates a flame that travels into the flame splitter that evenly ignites H4198 rifle powder that creates an even hotter and higher pressured gas. This gas propels a nylatron sabot with an attached flyer down the barrel where it passes through a light interruption system that measures its velocity. This projectile then hits the target of interest, whose velocity is measured by laser interferometry techniques.

To ensure planarity of the impact, several alignment procedures are conducted prior to the experiment. The first step is to align a low powered alignment laser down the gun barrel such that

it is collinear with the barrel. To do this, the laser light is controlled by a series of mirrors [78]. At the vacuum end, the light is focused on the target. Using a sharpee, one can mark where the light hits the target and then use a metal insert which has a small hole drilled into its center. Once the laser light through the small pinhole is coincident on the target with the larger dot of light, marked without the metallic insert on the target, the laser is considered to be collinear with the barrel. This light is now centered down the barrel and is used to align the target at the center of the impact. The final alignment is for tilt. Three sets of bolts with springs are used and inserted into a polycarbonate target holder. Adjustments can be made with a screw driver to adjust the tilt of the target. To minimize tilt, the light from the alignment laser must be reflected back onto itself from the target. The light is checked back at the laser end for concentric interference rings that indicate the laser is collinear with itself. This process mitigates tilt down to 5 mrad [13]. To check for the tilt during the experiment, four shorting pins distributed evenly around the target at the same radius can be used. These pins are set flush with the surface of the target – unlike the velocity pins which are staggered – and tilt is calculated using the pin circle radius, impact velocity and the center of the impact time:

$$\alpha = \frac{V_I t_c}{R}. \tag{5.1.2}$$

Here, α is the tilt in radians, V_I is the velocity of the projectile, R is the radius of the target, and t_c is the time for the shock wave to reach the center of the target, found by subracting the earliest pin arrival time from the average arrival time given by the 4 pins [56]. It should be noted that to avoid edge effects it is best to place the pins in the target holder rather than the target, but make sure that the diameter of the pins is within that of the flyer.

5.1.2 Sandia Single Stage Propellant Gun

The propellant gun used at Sandia National Laboratories is housed at the STAR (Shock Thermodynamic Applied Research) facility and contains an 89 mm smooth bore launch tube with a 17 m long barrel. Velocities range from 300-2300 m/s and are obtained by implementing phenolic projectiles weighing up to 1.5 kg. Unlike the Caltech system, the STAR powder gun has a direct mount to the barrel end for the target and an optical flat is used to align the target against the barrel to less than 1 mrad tilt. Shorting pins are used to measure the velocity, as described in the Caltech powder gun Section 5.1.1. In the vacuum chamber, the target and impactor are decelerated by a combination of steel plates and aluminum honeycomb [6]. Figure 5.4 shows the vacuum chamber

end of the gun.

Figure 5.4: Vacuum chamber of Sandia National Laboratories' single stage propellant gun.

5.1.3 Sandia Intermediate Velocity Gas Gun

For lower velocity impacts, Sandia's intermediate velocity gas gun was implemented. The advantage of this system is that it does not employ gun powder and hence cleanup is much simpler with a shorter turn-around time between shots. This gun contains a 7.6 m smooth bore launch tube with a velocity capability of 15-1000 m/s. Helium is used to obtain pressures of up to 6000 psi (˜41 MPa). To acheive the fast release of gas needed to propel the projectile down the barrel, the gun uses a double burst diaphragm that activates the gas release in ports contained in the gun breech. Alignment between the target and impactor is controlled by using an optical flat resulting in a tilt of less than 5 mrad. Projectile velocity is measured using shorting pins [6]. Figure 5.5 shows images of the gas gun.

(a) Launch end of the gas gun.

(b) Vacuum chamber end of the gas gun.

Figure 5.5: Sandia National Laboratories' intermediate velocity gas gun.

5.2 Diagnostics

The primary diagnostic used for velocity measurements in shock physics experiments has been velocimetery. Using laser light, experimentalists can measure the velocity of surfaces traveling in the km/s range. Two of these systems are the VISAR and PDV.

5.2.1 VISAR

5.2.1.1 Basic Theory

The Velocity Interferometer System for any Reflector (VISAR), was developed by Barker and Hollenbach [9] in 1972. Although laser interferometry was used previously, the techniques available required a mirror surface on which the light was reflected and only small amounts of tilt. The VISAR, on the otherhand, allowed for a diffuse surface to be monitored while still retaining 1-2% accuracies that previous techniques observed using nominal targets. The basic premise of the VISAR is that one portion of light is reflected off of a moving target which causes the light to be Doppler shifted. This shifted light is combined with itself after some delay time τ, which creates a beat frequency that can be related to velocity. A basic schematic of a VISAR system is shown in Figure 5.6.

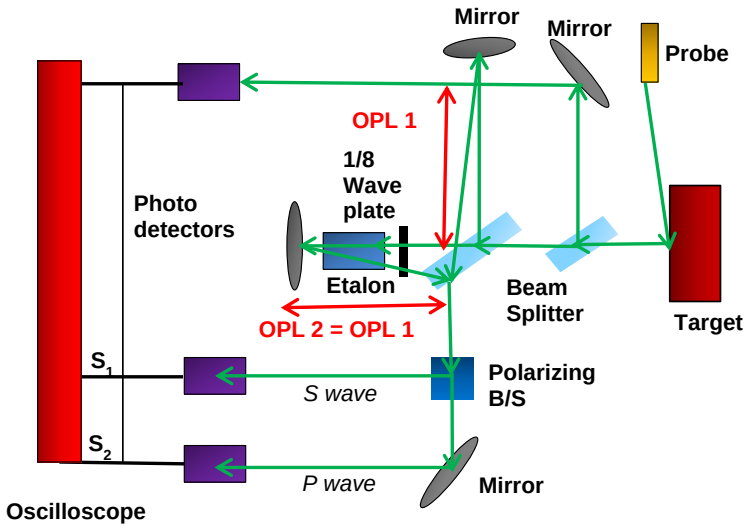

Figure 5.6: Schematic of a basic VISAR system.

As can be seen in Figure 5.6, light is reflected off of a target and sent into a beam splitter; 30% of this light is sent to a beam intensity monitor – the top photodetector in the diagram – and the rest

is sent into a 50/50 beam splitter. Part of this light is then sent into optical path length 1 (OPL1) and the rest is sent to OPL2, where the optical path lengths are the physical distance multiplied by the index of refraction. Although these paths are optically equal in length, the second path results in a time delay. The reason that both legs of light are equal in length is to allow for fringe contrast even when a surface is diffuse or spatially incoherent. In OPL2, the light is sent into a high index of refraction glass called an etalon and then into a 1/8 wave plate where it is reflected in the mirror. Since it passes twice through the etalon, the waveplate becomes an effective 1/4 waveplate resulting in the P component of light being retarded by 90 degrees and being circularly polarized. Light from both paths are collected at the polarizing beam splitter resulting in two interferometry fringes that are 90 degrees out of phase. This is known as quadrature and allows for acceleration and deceleration of the target to be detected. To obtain the fringe count from the signals measured at the detectors, s_1 and s_2 in Figure 5.6, the signal can be "unwrapped" with the equation

$$F(t) = \tan^{-1}\left(\frac{s_2}{s_1}\right). \tag{5.2.1}$$

This equation stems from the fact that the two signals are 90 degrees out of phase and hence their ratio is a tangent function. Signals s_1 and s_2 are a function of the measured intensity at the detectors, the intensity at the beam intensity monitor and normalization factors [45].

5.2.1.2 Angled Measurements

To understand mathematically what occurs in the combination of the light, the two optical fields can be described by [17],[32],[61].

$$\vec{E_1} = \hat{l_1} E_{01} e^{i\left(\vec{k_1}\cdot\vec{r}-\omega t+\phi_1\right)} \tag{5.2.2a}$$

and

$$\vec{E_2} = \hat{l_2} E_{02} e^{i\left(\vec{k_2}\cdot\vec{r}-\omega t+\phi_2\right)}, \tag{5.2.2b}$$

where $\hat{l_i}$ is a unit vector denoting direction of oscillation of the electric field $\vec{E_i}$, $\vec{k_i}$ is the propagation vector of the given field, E_{0i} is the amplitude of the electric field, $\vec{r}$ is the position vector of the point of observation, ω is the angular frequency, t is time, and ϕ_i is the initial phase angle of the beam. The propagation vector can be related to the wave number by

$$\vec{k_i} = \frac{2\pi}{\lambda}\vec{l_i}. \tag{5.2.3}$$

Interfering the two beams results in

$$\vec{E} = \vec{E_1} + \vec{E_2}, \tag{5.2.4}$$

with a time averaged intensity of

$$\begin{aligned} I = \left|\vec{E_1} + \vec{E_2}\right| = \left(\vec{E_1} + \vec{E_2}\right)\left(\vec{E_1} + \vec{E_2}\right)^* &= \vec{E_1}\vec{E_1}^* + \vec{E_2}\vec{E_2}^* + \vec{E_1}\vec{E_2}^* + \vec{E_2}\vec{E_1}^* \\ &= I_1 + I_2 + \vec{E_1}\vec{E_2}^* + \vec{E_2}\vec{E_1}^*, \end{aligned} \tag{5.2.5}$$

where the first two terms are the intensity of each beam and the last two terms govern the interference pattern. Writing out the interference terms results in

$$\begin{aligned} \vec{E_1}\vec{E_2}^* + \vec{E_2}\vec{E_1}^* &= \hat{l_1}E_{01}e^{i\left(\vec{k_1}\cdot\vec{r}-\omega t+\phi_1\right)}\cdot\hat{l_2}E_{02}e^{-i\left(\vec{k_2}\cdot\vec{r}-\omega t+\phi_2\right)} \\ &\quad + \hat{l_1}E_{01}e^{-i\left(\vec{k_1}\cdot\vec{r}-\omega t+\phi_1\right)}\cdot\hat{l_2}E_{02}e^{i\left(\vec{k_2}\cdot\vec{r}-\omega t+\phi_2\right)} \\ &= \hat{l_1}\cdot\hat{l_2}E_{01}E_{02}\left[e^{i\left(\left(\vec{k_1}-\vec{k_2}\right)\cdot\vec{r}-\omega t+(\phi_1-\phi_2)\right)} + e^{i\left(\left(\vec{k_2}-\vec{k_1}\right)\cdot\vec{r}-\omega t+(\phi_2-\phi_1)\right)}\right] \\ &= 2\hat{l_1}\cdot\hat{l_2}E_{01}E_{02}\cos\left(\left(\vec{k_1}-\vec{k_2}\right)\cdot\vec{r}+(\phi_1-\phi_2)\right). \end{aligned} \tag{5.2.6}$$

Combining the results of these interference terms and Equation 5.2.5 gives

$$I = I_1 + I_2 + 2I_1I_2\cos\left(\left(\vec{k_1}-\vec{k_2}\right)\cdot\vec{r}+(\phi_1-\phi_2)\right) = I_1 + I_2 + 2I_1I_2cos\Phi, \tag{5.2.7}$$

where Φ has replaced the terms $\left(\vec{k_1}-\vec{k_2}\right)\cdot\vec{r}+(\phi_1-\phi_2)$.

For the general case of a VISAR probe illuminating the target at an angle and the collected light being observed by the same probe and by an additional probe at another angle, the rear surface of the target can be illustrated by a diffraction grating, shown in Figure 5.7. In Figure 5.7, the amount the target moves is given by $\vec{\delta_r}$, the first VISAR probe shines and collects light at angle θ_1 and the second probe collects light at θ_2. The vectors $\vec{k_d^+}$, $\vec{k_d^-}$ and $\vec{k_i}$ are the propagation vectors of the two reflected electric fields and the incident field, respectively. The distance traveled by the grating, $\vec{\delta_r}$, can be expressed by

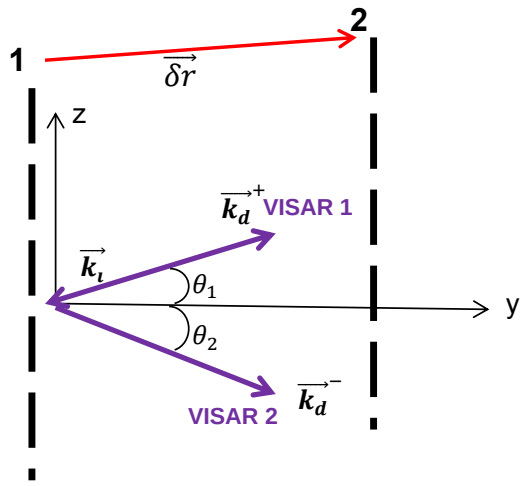

Figure 5.7: Rear surface of a moving target represented by a diffraction grating.

$$\vec{\delta_r} = \delta_y \hat{y} + \delta_z \hat{z} = Y\left(t - \frac{l}{c}\right)\hat{y} + Z\left(t - \frac{l}{c}\right)\hat{z}, \tag{5.2.8}$$

where Y and Z are the amount of movement in the y and z directions. Note that the coordinate system coincides with that given by Chhabildas [17] and represents, in that case, the y-cut quartz reference frame. In Figure 5.7, the propagation vectors can be expressed by the angles of the probes and the wavenumber, which is assumed to be the same for each path of light:

$$\vec{k_i} = -k\cos\theta_1 \hat{y} - k\sin\theta_1 \hat{z} \tag{5.2.9a}$$

$$\vec{k_d^+} = k\cos\theta_1 \hat{y} + k\sin\theta_1 \hat{z} \tag{5.2.9b}$$

and

$$\vec{k_d^-} = k\cos\theta_2 \hat{y} - k\sin\theta_2 \hat{z}. \tag{5.2.9c}$$

Plugging this result into Equation 5.2.7, the light collected at probe 1 is

$$I_{VISAR1} = I_1 + I_2 + 2I_1 I_2 \cos\left(-2k\cos\theta_1 Y\left(t - \frac{l}{c}\right) - 2k\sin\theta_1 Z\left(t - \frac{l}{c}\right) + \phi_0^+\right), \tag{5.2.10}$$

where $\phi_0^+ = \phi_i - \phi_d^+$. The electric field at probe 1 can then be expressed by

$$\vec{E^+} = A_1 A_2 \hat{l} e^{i\left(\vec{k}\cdot\vec{r} - \omega t + \Phi\right)}, \tag{5.2.11}$$

where it's been assumed the field oscillates in direction $\hat{l}$ and the amplitude of the electric field is $A_1 A_2$, a combination of the two original fields. In this equation, $\vec{k}\cdot\vec{r} = k\hat{y}\cdot l\hat{y}$, which means that at some point $l\hat{y}$, the VISAR is collecting the scattered light that propagates in the $k\hat{y}$ direction. Also, Φ is the interference term that arises when $\vec{k_i}$ and $\vec{k_d^+}$ mix, given in Equation 5.2.7. Comparing 5.2.7 with 5.2.10, the interference term can be replaced and Equation 5.2.11 becomes

$$\vec{E^+} = A_1 A_2 \hat{l} e^{i\left(\vec{k}\cdot\vec{r} - \omega t - 2k\left(\cos\theta_1 Y\left(t-\frac{l}{c}\right) + \sin\theta_1 Z\left(t-\frac{l}{c}\right)\right) + \phi_0^+\right)}. \tag{5.2.12}$$

Following a similar process, it can be shown that the light collected at probe 2 has the intensity

$$I_{VISAR2} = I_1 + I_3 + 2I_1 I_3 \cos\left(-k\left(\cos\theta_1 + \cos\theta_2\right) Y\left(t - \frac{l}{c}\right) - k\left(\sin\theta_1 - \sin\theta_2\right) Z\left(t - \frac{l}{c}\right) + \phi_0^+\right), \tag{5.2.13}$$

where $\phi_0^- = \phi_i - \phi_d^-$, which results in the electric field

$$\vec{E^+} = A_1 A_3 \hat{l} e^{i\left(\vec{k}\cdot\vec{r} - \omega t - k\left(\left(\cos\theta_1 + \cos\theta_2\right) Y\left(t-\frac{l}{c}\right) + \left(\sin\theta_1 - \sin\theta_2\right) Z\left(t-\frac{l}{c}\right)\right) + \phi_0^+\right)}. \tag{5.2.14}$$

If each of these Doppler (or phase) shifted signals is combined with itself in the VISAR after some delay time τ, then the signal at probe 1 becomes

$$I_{VISAR1}(t) = \left|\vec{E^+}(t) + \vec{E^+}(t-\tau)\right| = A_1^2 + A_2^2 + 2A_1^2 A_2^2 \cos(\alpha - \beta), \tag{5.2.15}$$

where

$$\begin{aligned}
\alpha - \beta &= [kl - \omega t + \Phi(t)] - [kl - \omega(t-\tau) + \Phi(t-\tau)] = -\omega\tau + \Phi(t) - \Phi(t-\tau) \\
&= -\omega\tau - 2k\left(\cos\theta_1 Y(t) + \sin\theta_1 Z(t)\right) + \phi_0^+ + 2k\left(\cos\theta_1 Y(t-\tau) + \sin\theta_1 Z(t-\tau)\right) - \phi_0^+ \\
&= -\omega\tau + 2k\left(\cos\theta_1\left(Y(t-\tau) - Y(t)\right) + \sin\theta_1\left(Z(t-\tau) - Z(t)\right)\right) \\
&= -\omega\tau + 2k\tau\left(\cos\theta_1 U(t-\tau) + \sin\theta_1 V(t-\tau)\right) \\
&= -\omega\tau + \tau\triangle\omega.
\end{aligned} \tag{5.2.16}$$

The term $\triangle\omega$ corresponds to the change in phase that arises when the two signals are mixed. Note

that, the change in displacement in the y and z directions was replaced by the velocities U and V multiplied by the time delay since the delay time is assumed to be small. The total number of fringes is given by [20]

$$\triangle F\left(t\right)\triangle\lambda = c\tau, \tag{5.2.17}$$

where $\triangle F\left(t\right)$ is the fringe count, $\triangle\lambda$ is the change of the wavelength of light from the doppler shift due to the movement of the target, c is the speed of light, τ is the delay time and $c\tau$ is the etalon length. Rearranging 5.2.17,

$$\triangle F\left(t\right) = \frac{c\tau}{\triangle\lambda} = \frac{c\tau\triangle\nu}{c} = \frac{\tau\triangle\omega}{2\pi}. \tag{5.2.18}$$

Plugging in for $\tau\triangle\omega$ from above into 5.2.16 and rearranging,

$$\frac{\lambda\triangle F\left(t\right)}{2\tau} = \cos\theta_1 U\left(t-\tau\right) + \sin\theta_1 V\left(t-\tau\right), \tag{5.2.19}$$

where the left hand side is what the scope measures and the right hand side can be used to relate the measurement to the particle velocities and angles. For the second VISAR, the approach is similar:

$$I_{VISAR2}\left(t\right) = \left|\vec{E^-}\left(t\right) + \vec{E^-}\left(t-\tau\right)\right| = A_1^2 + A_3^2 + 2A_1^2A_3^2\cos\left(\alpha-\beta\right) \tag{5.2.20}$$

and

$$\begin{aligned}
\alpha-\beta &= \left[kl-\omega t+\Phi\left(t\right)\right] - \left[kl-\omega\left(t-\tau\right)+\Phi\left(t-\tau\right)\right] \\
&= -\omega\tau - k\left(\left(\cos\theta_1+\cos\theta_2\right)Y\left(t\right) + \left(\sin\theta_1-\sin\theta_2\right)Z\left(t\right)\right) + \phi_0^- \\
&+k\left(\left(\cos\theta_1+\cos\theta_2\right)Y\left(t-\tau\right) + \left(\sin\theta_1-\sin\theta_2\right)Z\left(t-\tau\right)\right) - \phi_0^- \\
&= -\omega\tau + k\tau\left(\left(\cos\theta_1+\cos\theta_2\right)U\left(t-\tau\right) + \left(\sin\theta_1-\sin\theta_2\right)V\left(t-\tau\right)\right) \\
&= -\omega\tau + \tau\triangle\omega.
\end{aligned} \tag{5.2.21}$$

Using Equation 5.1.2 and rearranging terms results in

$$\frac{\lambda\triangle F\left(t\right)}{2\tau} = \frac{1}{2}\left(\left(\cos\theta_1+\cos\theta_2\right)U\left(t-\tau\right) + \left(\sin\theta_1-\sin\theta_2\right)V\left(t-\tau\right)\right), \tag{5.2.22}$$

which is what VISAR 2 measures. Hence, the VISAR measurements can be used to find the particle

velocities if the angles are known.

5.2.1.3 Normal Measurements

For a central probe shining light perpendicular onto the back of a target and collecting that light back at $\theta_1 = 0$ without the second probe, Equation 5.2.19 becomes

$$\frac{\lambda \triangle F(t)}{2\tau} = U(t-\tau). \tag{5.2.23}$$

This result matches the velocity to fringe count relation for a VISAR system using a normal incident probe [20]. The interferometry delay time, τ, is a function of the etalon length and its index of refraction and is given by [9]

$$\tau = \frac{2h}{c}\left(n - \frac{1}{n}\right), \tag{5.2.24}$$

where h is the etalon length, n is the index of refraction, and c is the velocity of light in free space.

5.2.1.4 Window Measurements

When using a window to make in-situ measurements in an experiment, a correction must be made to Equation 5.2.23. During an experiment, the light is Doppler shifted causing the index of refraction to change due to its dependence on the wavelength of light passing through the material. This change causes dispersion of the light [10]. The derivation of the correction term is described in [10], the result of which is that Equation 5.2.23 becomes

$$\frac{\lambda \triangle F(t)}{2\tau(1+\delta)\cos\theta_n} = U(t-\tau), \tag{5.2.25}$$

where

$$\delta = 1 - \left(\frac{n_0}{n_0^2 - 1}\right)\lambda_0 \left.\frac{dn}{d\lambda}\right|_{\lambda_0}, \tag{5.2.26}$$

and $\cos\theta_n$ is the correction for the angle of the central probe. Here, n_0 is the initial index of refraction, λ_0 is the initial wavelength and $\lambda_0 \left.\frac{dn}{d\lambda}\right|_{\lambda_0}$ is the derivative of the index of refraction with respect to wavelength evaluated at the initial wavelength. The correction δ has been evaluated for a variety of materials at a range of pressures and is documented in [8]. For angled measurements through a window, the analysis becomes a bit more complicated. Once again the index of refraction

changes, however, it is much more difficult to follow an angled probe path since the light coming in travels a different distance than the light coming out; in most cases, experimenters will use a normal probe to shine light into the window and will collect light with two probes that are off-axis from the normal. Following this approach results in a symmetric problem where the portion of the measured velocity that is dependent on the index of refraction is equivalent for both probes. Since it is difficult to track the change to the index of refraction for these angled measurements, one can subtract one of the angled measurements from the other which cancels out the dependence on the index of refraction and results in the equation

$$V\left(t-\tau\right)=\frac{V^{+\theta}-V^{-\theta}}{\sin\theta_t}=\frac{\frac{F_+(t)\lambda}{2\tau}-\frac{F_-(t)\lambda}{2\tau}}{\sin\theta_t}, \tag{5.2.27}$$

where $V\left(t-\tau\right)$ is the transverse velocity at the target-window interface, $V^{+\theta}$ and $V^{-\theta}$ are the apparent velocities measured at the off-axis probes, and θ_t is the nominal angle between each of the probes and the normal to the window — note that this is the measurement taken outside of the window, not within the window where the beams refract. For this relation to work, the probes must be within half a degree off from one another [29], [31].

5.2.1.5 Push-Pull VISAR

To minimize noise in the data, the push-pull VISAR was invented by Hemsing [45]. The diagram of this modified VISAR is shown in Figure 5.8. As can be seen in this figure, rather than sending part of the light reflected off of the target into a beam intensity monitor, the entire amount is sent into the system. Once again light is sent to two optical path lengths, one with a delay leg, and then recombined in a beam splitter. At this point the two signals are 90 degrees out of phase due to the 1/8 waveplate. This light is split and sent to two polarizing beam splitters which further separate the light into S and P waves. The signals are collected at four channels that measure s_1 and its complement $s_1^{'}$, and s_2 and its complement $s_2^{'}$. Using a similar approach to Equations 5.2.15 and 5.2.16, these signals can be expressed in terms of their interference components, since this is what is used to determine the velocity:

$$s_1=2A_1^2A_2^2\cos\left(-\omega\tau+\triangle\phi\right)=2A_1^2A_2^2\cos\left(2\pi\triangle\nu t+\triangle\phi\right) \tag{5.2.28a}$$

$$s_2=2A_1^2A_2^2\cos\left(2\pi\triangle\nu t+\triangle\phi+\pi/2\right)=2A_1^2A_2^2\sin\left(2\pi\triangle\nu t+\triangle\phi\right) \tag{5.2.28b}$$

$$s_1^{'} = 2A_1^2A_2^2\cos\left(2\pi\triangle\nu t + \triangle\phi + \pi\right) = -s_1 \tag{5.2.28c}$$

$$s_2^{'} = 2A_1^2A_2^2\sin\left(2\pi\triangle\nu t + \triangle\phi + \pi\right) = -s_2. \tag{5.2.28d}$$

The complements of each signal, given by Equations 5.2.28c and 5.2.28d, can be subtracted from the original signals, in Equations 5.2.28a and 5.2.28b, essentially amplifying the signal, and hence canceling incoherent light due to the subtraction, resulting in better resolution.

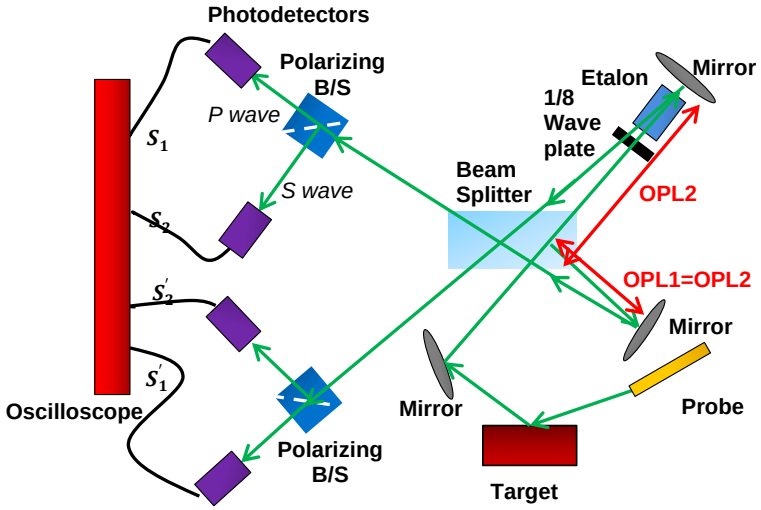

Figure 5.8: Schematic of a Push-Pull VISAR.

5.2.1.6 Caltech VISAR

The VISAR implemented at Caltech is the MiniVISAR system made by National Security Technologies. It is a lens-relayed, air-delay VISAR that has a fixed delay time. An image of the inside of the MiniVISAR is shown in Figure 5.9. Although this is a lens relayed system, it has the same functionality as a push-pull VISAR system. The optical path length difference for this VISAR is 149.57 mm which is equal to $c\tau$ giving a delay time of τ=0.4989 ns. From Equation 5.2.23, $\frac{\lambda\triangle F(t)}{2\tau} = U$. For one fringe this means

$$vpf = 515.63 \text{ m/s/fringe}, \tag{5.2.29}$$

which is the velocity per fringe constant used to reduce data. The laser used for this system is

the Coherent Innova 300C Argon Ion 1 W model at the 514.5 nm wavelength. To monitor the signals, differential amplifiers are used which amplify the signal by 10 and perform the subtraction for the complementary signals. The Agilent Technologies InfiniiVision MSO-X-4104A mixed signal oscilloscope with a 1 GHz bandwidth is used to record the data providing enough resolution for the 1 ns rise time of the photodetectors.

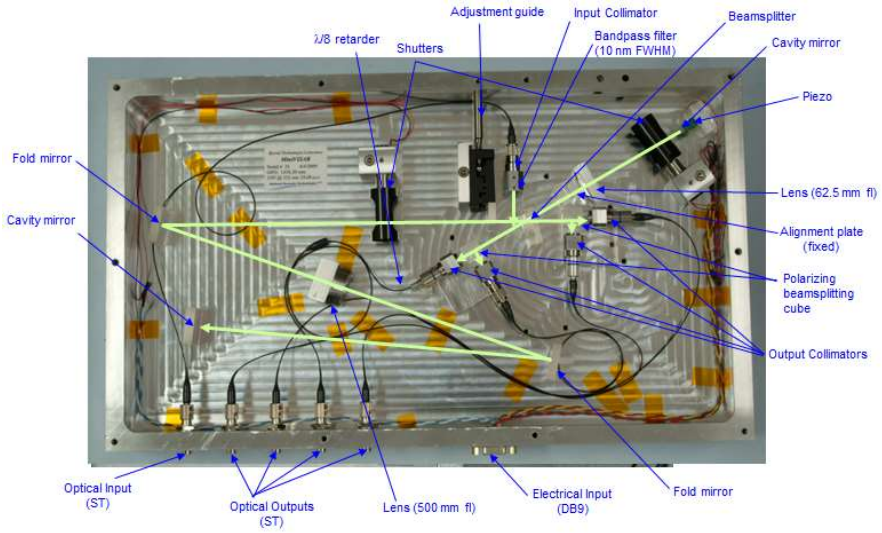

Figure 5.9: Inside of MiniVISAR (Courtesy of National Security Technologies).

5.2.1.7 Sandia VISAR

The VISAR systems at Sandia use a Coherent V-10 diode-pumped solid-state laser at 532 nm that pumps a neodymium-doped YAG crystal [13]. Sandia has a variety of MiniVISAR systems with different velocity per fringe constants depending on the application. They also implement a table top VISAR that has a variable time delay capability. These VISARs are push-pull systems and one can be used in conjunction with another to increase the accuracy of the data. This is known as a dual-delay VISAR. By using two VISARs with vpf's that are not multiples of one another, a unique solution can be obtained even in the presence of fringe jumps which often result in ambiguity in the presence of a shock wave. As described above, each signal is a function of the phase change from the original signal to the signal at the time of recording. Adding 2π to the initial phase results in the same quadrature signal when the inverse tangent is found from the two signals in Equation 5.2.1 [28]. When a signal is not smooth – such as in a shock wave – it is unclear how many revolutions have been added to the phase and thus using two vpf's resolves this ambiguity.

5.2.2 PDV

5.2.2.1 Setup and Theory

Photon Doppler Velocimetry (PDV) is a fiber based technique that uses mainly off-the shelf components to measure the velocity of a moving target [74]. These components are readily available as they are used in part for the telecommunications industry. Unlike the VISAR, the PDV is a displacement interferometer that produces a fringe for each half a wavelength that a surface moves [7]. In this technique, fibers are implemented to send infrared light at 1550 nm in wavelength into a probe that focuses this light onto a surface of interest. Part of this original light is sent to a sensor, while the remaining light endures a Doppler shift when it is reflected off of a moving surface. The reference and reflected light are then recombined at a digitizer. This mixing of two different wavelengths creates a beat frequency that can be related to the velocity of the moving target.

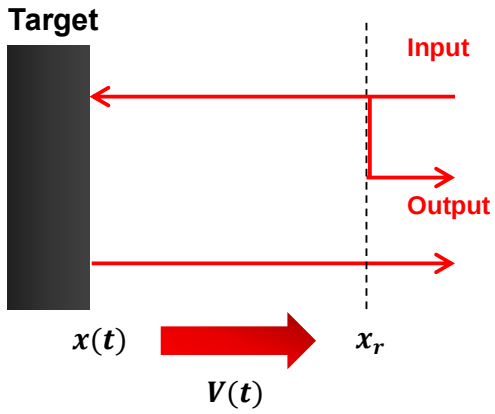

Figure 5.10: Mixing of two wavelengths for PDV.

5.2.2.2 Homodyne System

The basic premise of the PDV can be seen in the Figure 5.10. Light is sent to a beam splitter which collects part of it – called the reference leg – and sends the rest to be reflected at the target surface at some position $x\,(t)$. This light is Doppler shifted and recombined with the reference light at some position, x_r [5]. At the detector, the electric field can be represented as

$$E\,(t) = E_R\,(t)\,cos\,(\Phi_R\,(r)) + E_T\,(t)\,cos\,(\Phi_T\,(r))\,, \tag{5.2.30}$$

where $E_i\,(t)$ is the field amplitude, $\phi_i\,(t)$ is the optical phase of each signal, R is the reference path, and T is the target path. This formula is similar to that used for the VISAR in Equation 5.2.2a. At

the detector, the cycle averaged output intensity can be expressed as

$$I(t) = I_R + I_T + \sqrt{I_R I_T}\cos\Phi(t), \tag{5.2.31}$$

where I_R is the non-doppler shifted intensity from the laser, I_T is the doppler shifted intensity from the moving surface, and $\Phi(t)$ is the optical phase difference – which is given as the interference between the optical phase differences for both the reflected and reference paths, $\Phi_T(t) - \Phi_R(t)$. In Equation 5.2.31, the first two terms on the right hand side are the continuous wave components of the signal, while the last term contains the beat frequency information. If it is assumed that the target undergoes a small change in velocity over some small period of analysis, τ, then the instantaneous position of the target can be expressed as

$$x \approx x(\bar{t}) + \bar{v}(\bar{t})[t - \bar{t}], \tag{5.2.32}$$

where $\bar{v}$ is the average interval velocity and $\bar{t}$ is the center of the time interval. Then the optical phase difference within this interval of time can be approximated as

$$\Phi(t) \approx \Phi(t_1) - \bar{\omega}(\bar{t})[t - \bar{t}], \tag{5.2.33}$$

where $\bar{\omega}(\bar{t}) = \frac{4\pi\bar{v}}{\lambda_0}$ is the radial beat frequency within the signal and contains the velocity information of the target and $\Phi(t_1)$ is the optical phase difference at the previous time interval. Then, much like with the VISAR, the electrical output at the detector can be shown to be a function of this phase difference,

$$s(t) = A\cos\left(\bar{\Phi}(t_1) - \bar{\omega}(\bar{t})[t - \bar{t}]\right). \tag{5.2.34}$$

The frequency in the interval of interest is found using a short-time Fourier transform (STFT), which calculates the electrical power spectrum,

$$S(\omega, \bar{t}) = \int_{-\infty}^{\infty} s(t)\, w(t)\, e^{-i\omega t} dt, \tag{5.2.35}$$

where $w(t)$ is the window function that extracts the beat frequency information from the peak of the power spectrum at each point $\bar{t}$ in the interval τ. The average velocity in this interval is given as a function of the beat frequency $\bar{f}$:

$$\bar{v} = \frac{\lambda_0}{2}\bar{f} = \frac{\lambda_0}{4\pi}\bar{\omega}. \tag{5.2.36}$$

In this equation, λ_0 is the reference wavelength of light.

5.2.2.3 Heterodyne System

Prior to impact, a target is generally stationary and hence there is no Doppler shifted light to be mixed with reference light in order to create a beating frequency. Unfortunately, this means that no velocity can be extracted. While this is not an issue for stationary time periods, this problem arises for low velocities. In this case, signal noise may obscure the beat frequency and makes it difficult to extract any relevant information. This can be seen quantitatively through the uncertainty product which states that $\tau \triangle f \geq \frac{1}{4\pi}$ (see SIRHEN manual for more details [5]). For instance, to achieve velocity precision of $\triangle v = 10$ m/s, the peak width is given as $\triangle f = \frac{2\triangle v}{\lambda_0} = 1.29$ x 10^7/s, which indicates that the time resolution needed in the STFT technique is $\tau \approx 6$ ns. For small velocities on the order of 100 m/s, $\frac{\triangle v}{v} = 10\%$ which means that the velocity precision is quite poor. To mitigate this problem, one could increase the time interval, but this leads to less timing precision. A solution to this issue is frequency conversion.

Frequency conversion, or "upshifting", occurs when the reference light is set to be at a different wavelength than the light at the target. A method to do this is with an Acousto-Optic (AO) frequency modulator. This device adds in a specified wavelength to the path of light sent to the target, while the reference leg remains at the original frequency. Thus, when a target is traveling at a lower velocity, it has a higher beat frequency allowing for a precise velocity measurement. The beat frequency can be expressed as

$$f_{beat} = f_{mod} + \frac{2v}{\lambda_0}, \tag{5.2.37}$$

where f_{mod} is the frequency added by the AO modulator. Figure 5.11 shows a schematic of a heterodyne PDV system used to make angled measurements for transverse velocities.

5.2.2.4 Angled Measurements

A similar analysis to that conducted in Section 5.2.1.2 can be applied to the PDV. The right hand side of Equations 5.2.19 and 5.2.22 can be related to the reduced data from each of the side probes, shown in Figure 5.11, although the left hand side of the equations will not have the same

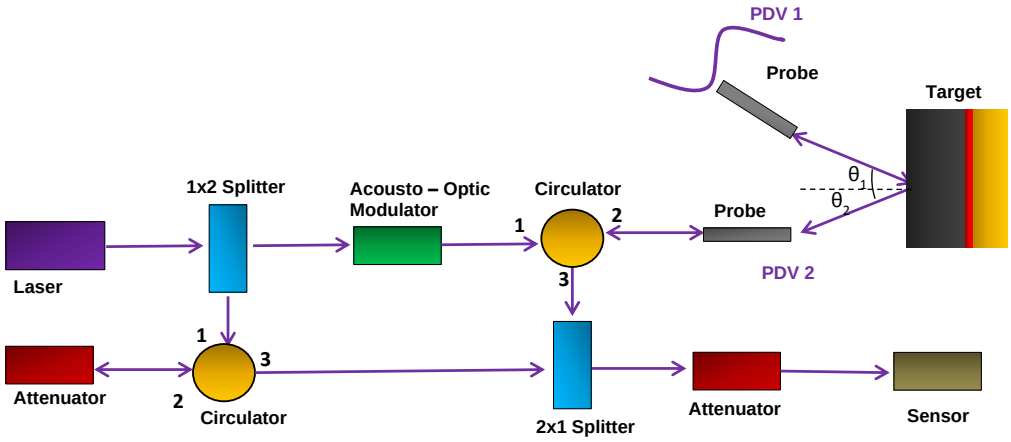

Figure 5.11: Schematic of a Heterodyne PDV System.

terms. Nevertheless, it is not necessary to have the exact description of the left hand terms provided the PDV data can be reduced to find the apparent velocity at each probe.

5.2.2.5 Caltech PDV

The PDV at Caltech uses four channels allowing for four different probes to measure velocities. The modification to Figure 5.11 is that light is sent from the laser into a four-way beam splitter where it can be distributed to four different probes. It is a heterodyne velocimeter, similar to the system shown in Figure 5.11, and is also time multiplexed, which means that channels 2 and 4 are delayed by 4 km of single mode fiber and then mixed back with channels 1 and 3. Channels 1 and 2 are collected at one photosensor and channels 3 and 4 are collected on another sensor. Since the signals are multiplexed, the delay allows for the differentiation between each signal. Another modification made to the system in Figure 5.11 is to use a laser rather than an AO modulator to upshift the signal. An Agilent MSO 9104A 4GHz oscilloscope is used to record the signals. The laser used is an NKT Photonic 2 W booster laser and has a 20 mW seeder laser [66].

5.3 Scattering Experiments

A series of scattering experiments were conducted to deduce what angle of probes are best to use to obtain shear velocity measurements. These experiments were done by machining an aluminum 6061-t6 wedge and placing a PMMA wedge on top of the aluminum. The back surface of aluminum was sand blasted with small micro-beads ranging from 44 μm to 422 μm in diameter. The goal of

sand blasting the surface was to create a diffraction grating effect to scatter the light. As shown in Figure 5.12, light was shined through a probe normal to the surface and was collected at a second probe off-axis from the normal. The results of this study analyzed qualitatively how much light was returned by looking at the lissajous of the two VISAR signals for the side probe. A target alignment system was used consisting of a cylindrical holder that was machined such that the two wedges could be securely placed within the holder and rotated such that the back surface of the PMMA was parallel to the horizontal plane allowing for accurate measurements. Figure 5.13 shows the holder at the top of the image and the aluminum-PMMA assembly at the bottom of the figure. The PMMA window was polished with a series of sand paper and Cerium-Oxide polishing compound made by Buehler. During these experiments, it was found that polishing the PMMA and microbead-blasting the aluminum surface with beads in the range of 44 μm to 89 μm resulted in the most light returned at angles of approximately 5-20 degrees. A similar study was conducted at Sandia without a window and it was found that light shined along the normal and collected with two probes at 17 and 25 degrees works best [3]. A variation between free surface angled measurements and windowed angled measurements is to be expected, however, these results show that the angles found in this study match closely to the findings at Sandia.

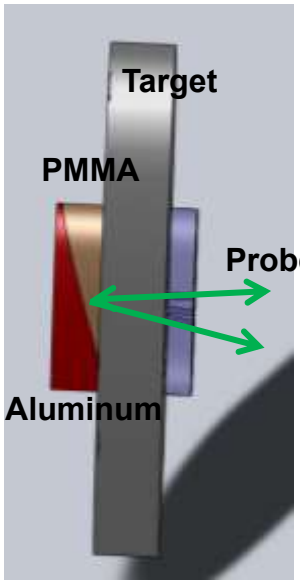

Figure 5.12: Schematic of scattering experiments assembly.

Figure 5.13: Cylindrical alignment holder for aluminum-polymethylmethacrylate wedge configuration.

Chapter 6

Experimental Setup and Results

6.1 Introduction

A variety of experiments were performed at Sandia National Laboratories to explore the novel experimental setups previously discussed. The y-cut quartz validation experiment was conducted at Sandia to show the ability to measure transverse velocities through a window. Oblique wedge experiments were performed at Sandia as well and show the promise of this technique to measure shear particle velocities and hence strength.

6.2 Y-Cut Quartz Validation Experiments

As previously mentioned, y-cut quartz generates a two-wave structure upon impact where both waves contain longitudinal and shear velocity components. Utilizing this well analyzed material, experiments were performed to test the off-axis probe configuration in its ability to measure transverse velocity. An aluminum impactor was used to impact a y-cut quartz sample at 171.1 m/s and a lithium fluoride window was implemented to measure the in-situ velocities. The experiment was conducted at Sandia National Laboratories' STAR facility using the intermediate velocity gas gun, discussed in Section 5.1.3. Figure 6.1 shows the four shorting pins used to find the velocity of the flyer as well as the four pins used to find the tilt, which was calculated to be 0.41 mrad.

6.2.1 Target Preparation

A 0.5021" thick y-cut quartz sample 2.153" in diameter and with a density of 2.6362 g/cm^3 was used in conjunction with a 0.4955" thick lithium fluoride window that was 1.2512" in diameter and had a density of 2.6320 g/cm^3. The window was plated with a 2500 angstrom thick aluminum spot

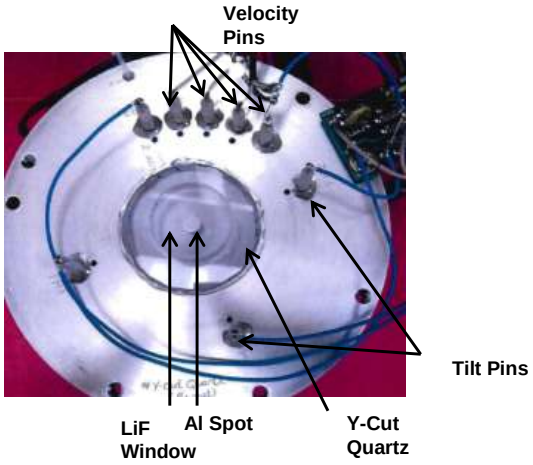

Figure 6.1: Y-cut quartz validation experiment with a lithium fluoride window bonded into a target holder at Sandia National Laboratories' STAR facility.

that was diffused with micro-glass beads in order to diffract light and the two materials were bonded with an epoxy applied between the materials with a -0.0005" thick glue bond. The negative sign of the glue bond indicates that it was thinner than the smallest measurement that could be made precisely. Figure 6.1 shows the target setup.

6.2.2 Probes

Three probes were used to measure the velocity, with one probe normal to the window rear surface and the other two off-axis from the window. The central probe was used to focus light onto the aluminum spot, where it was reflected and also scattered such that it could be collected back at the focusing probe and also at the two side probes. Equation 5.2.27 was used to find the transverse velocity from the two side measurements, and 5.2.25 was used to find the normal velocity from the central probe. Three MiniVISARs were used for each of the probes with vpfs of 70.69 m/s/fringe for the normal probe, 61.50 m/s/fringe for one of the side probes and 26.60 m/s/fringe for the other. The window correction $1 + \delta$ in Equation 5.2.25 was 1.29 for the LiF window. Note that it did not need to be used on the side probe measurements as previously explained for Equation 5.2.27. Figure 6.2a shows an image of the probe holder used to mount the probes onto the target. A cylindrical shell fits around the LiF window on top of which rests a polycarbonate holder with two ball-and-socket holders for the side probes, allowing for maneuverability, and a central hole for the focusing probe.

Once light return was checked on each probe, the angles of each of the probes were measured. Figure 6.3 shows a schematic of the measurements made. Light from a low powered green light laser

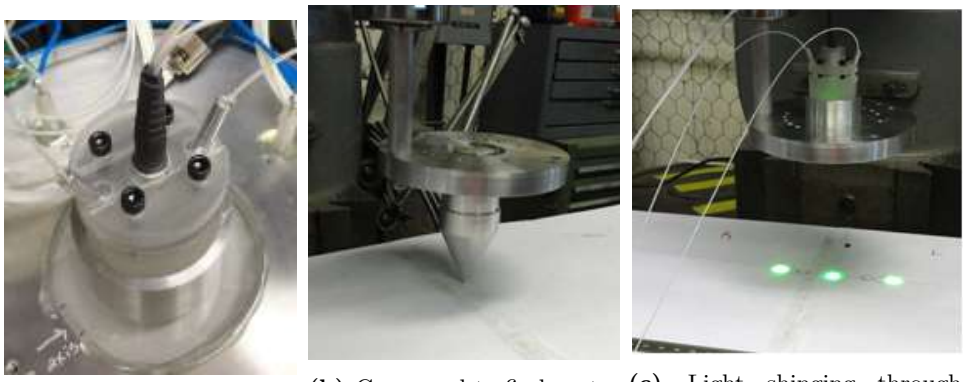

(a) Probe holder assembly.

(b) Cone used to find center of target holder.

(c) Light shinging through probes traced onto paper.

Figure 6.2: Probe holder for central and two off-axis probes for the y-cut quartz validation experiment.

was split to shine light into each of the three probes – only the two side probes are shown in Figure 6.3a, but the approach is the same for the central probe. An assembly using a mill held the probe holder with the probes and was moved in known increments vertically from the table. A sharp cone, shown in Figure 6.2b, was used to find the center of the target projected onto a piece of paper below the probes. The light shining into the probes moves further out from the center as the assembly is moved away from the table and by recording the distance of the center of the light circles and correlating it to the height the probes were moved from the table, the angles were found. An image of these circles of light is shown in Figure 6.3a. The equation fitting the height to the distance from the center as a function of angle is given by the linear relationship

$$h = md + b, \tag{6.2.1}$$

where

$$\tan\theta = \frac{d}{h}. \tag{6.2.2}$$

To solve for θ, one can look at the triangle formed in Figure 6.3b from d and h and see that, when the assembly is at some distance d from the table, where at height $h = 0$, $d = -b/m$, and at distance $d = 0$ from the center, the variable $h = b$, plugging in for d and h into 6.2.2 results in

$$\theta = \tan^{-1}\left(-\frac{1}{m}\right). \tag{6.2.3}$$

The angles for the two side probes were 19.5451 degrees and 19.9508 degrees, which average out

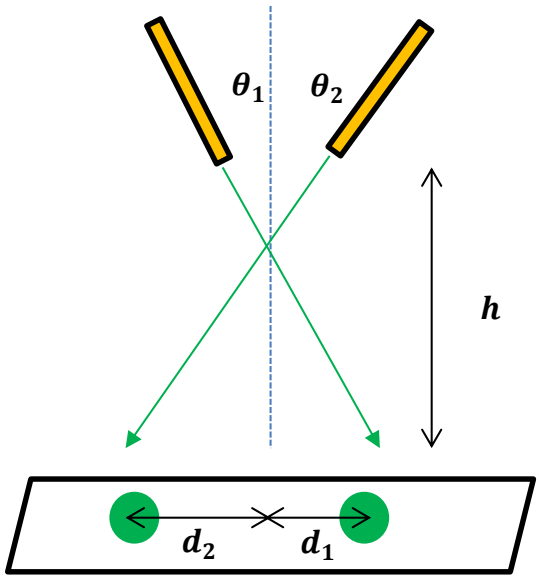

(a) Light shining from probes.

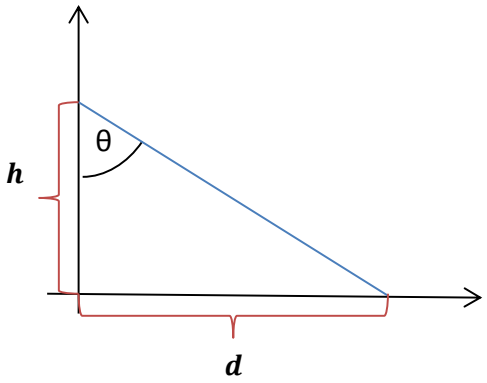

(b) Triangle formed by light.

Figure 6.3: Schematic of the methodology used to measure probe angles in y-cut quartz validation experiment.

to 19.7480 degrees for the VISAR analysis. The angle for the central probe was 1.5 degrees off from the center normal. Equations 5.2.25 and 5.2.27 can be used to find the velocities at the target-window interface. Note that for this experiment, the normal measurement was actually affected by a reflection off of the rear surface of the window which means that it must be divided in half to obtain the in-situ velocity, or

$$U\left(t-\tau\right)=\frac{\frac{F(t)\lambda}{2\tau(1+\delta)}}{2\cos\theta_c}. \tag{6.2.4}$$

Both probes were manufactured by Oz Optics for 532 nm wavelength light with a spot size of 200 μm for the focusing probe and a 28 mm focal length. The side collimating probe also had a spot size of 200 μm which was used to collect the scattered light. Although light refracts as it enters the lithium fluoride window, the angles with respect to the normal at the window rear surface were used.

6.2.3 Results and Discussion

The results of the y-cut quartz validation experiment are shown in Figure 6.4. The experimental velocities are the in-situ velocities at the target-window interface. Simulation velocities were found using Laslo. As previously mentioned in Section 3.6.10, lithium fluoride is very well matched to aluminum, which is also fairly well matched to y-cut quartz, thus the results show that the velocities measured in the LiF window are actually close to the simulation, which calculates the particle velocities in the quartz. In Figure 6.4a, it is clear that there are some odd reflections in the velocity profile which could be due to the measurement taking place at the rear surface of the LiF rather than in-situ. This anomaly was detected due to the fact that the normal velocity profile occurred later in time than the profiles from the side probes. Nevertheless, the ultimate value of the velocity is similar to the simulation. Furthermore, measurement of normal velocities through a window is a well-known technique that has been proven to work. The real concern that this experiment analyzed was the transverse velocity profile. This is shown in Figure 6.4b. As can be seen here, the magnitude is quite similar to the simulation value and the only discrepancy is the drop in the velocity at about 2.6 μsec resulting in a slightly shorter pulse. This could be due to reflections within the target. However, despite this small variation, it is clear that the measured shear velocity with the windowed approach is representative of the actual velocity in the experiment and thus it can be assumed that using a window with two side probes is a valid technique to finding the shear velocity at the target-window interface.

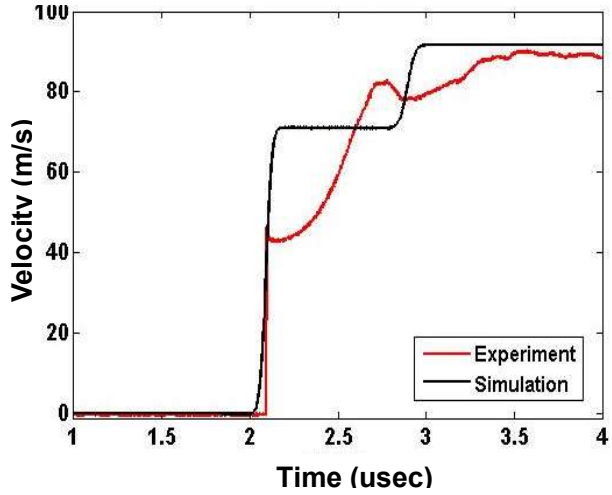

(a) Longitudinal particle velocity.

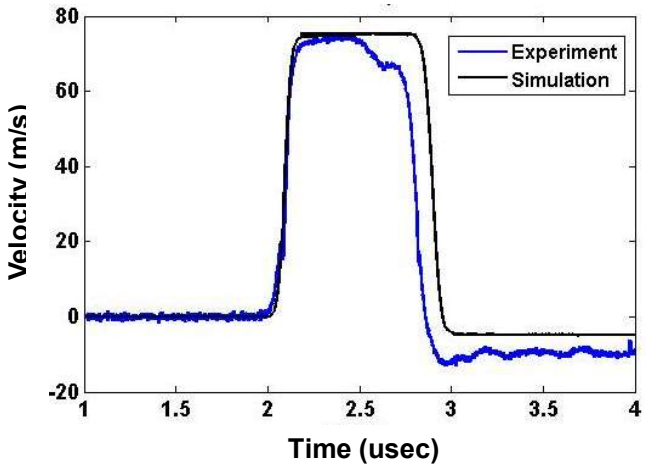

(b) Shear particle velocity.

Figure 6.4: Experiment velocities vs. simulation velocities for y-cut quartz validation experiment with an impact at 171.1 m/s.

6.3 Oblique Wedge Experiments

Once the use of off-axis probes was proven to be valid for the measurement of transverse velocity in the y-cut quartz validation experiment, this technique could be used to find the in-situ velocities in the novel oblique wedge configuration. In these experiments, a copper impactor propelled at nominally 1000 m/s was used to impact the composite target configuration consisting of a polymethylmethacrylate driver, aluminum 6061-t6 target and a lithium fluoride window. This is analogous to the configuration discussed in Section 3.6 where the incident shock angle was 10 degrees and the transmitted shock angle was 5.33 degrees as shown in Table 3.4. These experiments were conducted at Sandia National Laboratories' STAR facility using the powder gun discussed in Section 5.1.2. The target plates used to hold the target implement the same design as shown in Figure 6.1.

6.3.1 Target Preparation

The targets of interest were machined out of 6061-t6 aluminum and a polymethylmethacrylate (PMMA) sleeve was made with a separate PMMA wedge into which the aluminum wedge could fit. This was deemed to be the best approach for such a complex configuration. The composite target was assembled by first placing the wedge into the PMMA sleeve, shown in Figure 6.5a, and then placing the aluminum wedge on top of the PMMA and spinning these pieces until the rear surface of the aluminum was parallel to the PMMA sleeve back surface, which was machined such that the rear surface was angled to be parallel to the aluminum target. The aluminum alignment sleeve shown in Figure 6.5a was used so that the PMMA-aluminum assembly could be placed in it and it was machined such that the bottom and top of the piece was angled at the same angle as the rear surface of the aluminum specimen. The reason for this angle on both sides was such that, when the PMMA-aluminum assembly was placed inside the cylinder and spun around to be parallel to the back surface, the configuration would sit flat on a horizontal surface and a weight could be placed on the back surface as the epoxy between the PMMA wedge and sleeve and the aluminum wedge and PMMA wedge cured. After the epoxy cured, a drop sized amount of epoxy was placed on the aluminum onto which the LiF window – with the same design as that used for the y-cut quartz validation experiment – was placed. A weight was also placed on this setup to ensure the epoxy spread out and dried evenly.

Originally, the window for this experiment was intended to be angled, but it was decided that it was much simpler to use a window parallel to the rear surface of the aluminum such that the index

(a) Aluminum alignment cylinder with PMMA wedge and sleeve and aluminum wedge (from left to right).

(b) Assembled target configuration with PMMA and aluminum.

(c) Placement of window onto target assembly.

Figure 6.5: Assembly procedure of oblique wedge target.

of refraction dependent portions of the optical path lengths of the side probes through the window canceled out and Equation 5.2.27 could be used. The thickness of the window was chosen so that the measurement was made before the transmitted shock in the LiF hit the rear surface, at which point the window could separate from the target.

To measure the density of the aluminum wedge, a measurement of each of the three sides was taken, as shown in Figure 6.6a in the cross-sectional view. To find the volume of the wedge, each of the sides of the wedge target can be thought of as being inscribed in a cylinder whose total volume is

$$\pi \left(\frac{h}{2}\right)^2 d = A + B + C. \tag{6.3.1}$$

This is the sum of the three volumes shown in Figure 6.6b, where C is the volume of the wedge. These volumes can be written as

$$A = \frac{1}{2}\pi \left(\frac{h}{2}\right)^2 d_1 \tag{6.3.2}$$

and

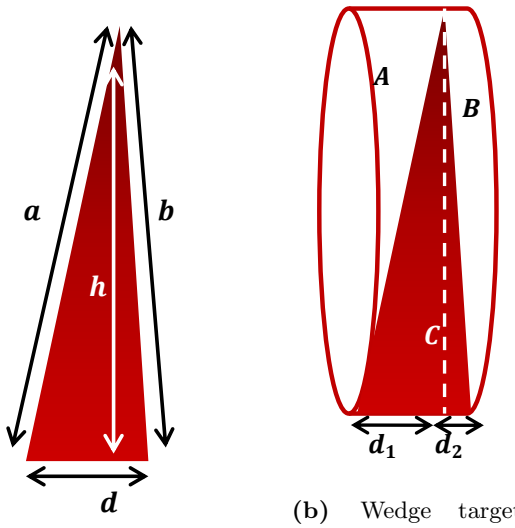

(a) Cross-section of wedge target.

(b) Wedge target volume inscribed in cylinder.

Figure 6.6: Diagrams for measurement of density in wedge target.

$$B = \frac{1}{2}\pi\left(\frac{h}{2}\right)^2 d_2. \tag{6.3.3}$$

Then,

$$C = \pi\left(\frac{h}{2}\right)^2 d - A - B = \pi\left(\frac{h}{2}\right)^2 d - \pi\left(\frac{h}{2}\right)^2 (d_1 + d_2) = \frac{1}{2}\pi\left(\frac{h}{2}\right)^2 d. \tag{6.3.4}$$

The height h can be found by the relations

$$d_1 = \sqrt{a^2 - h^2} \tag{6.3.5a}$$

and

$$d_2 = d - d_1 = \sqrt{b^2 - h^2}. \tag{6.3.5b}$$

Combining 6.3.5a and 6.3.5b results in the relation

$$\sqrt{a^2 - h^2} + \sqrt{b^2 - h^2} - d = 0. \tag{6.3.6}$$

From here, h can be solved for and then used to find the volume of the wedge, which is then divided by its mass to obtain the density.

6.3.2 Setup

The oblique wedge experiment was assembled into a target plate similar to that shown in Figure 6.1. To measure the arrival of the incident shock wave at the PMMA-aluminum interface – such that the wave velocities could be found based on time and distance traveled in the aluminum specimen – a separate PMMA sample was tested simultaneously. This configuration is shown in the schematic in Figure 6.7. Here, the front and back surfaces of the PMMA sample were coated with diffused aluminum such that two probes could be used to measure the velocity at the front and the back of the target. Although the Hugoniot of PMMA is known and the arrival time at the front of the aluminum target could be found using impedance matching, it was concluded that it would be more accurate to test this in real time by calculating the velocity of the shock through the PMMA for the experiment. Prior to the experiment, the impact of the PMMA with the copper flyer was analyzed to see if the PMMA was overdriven, which means that the shock velocity is greater than the elastic wave velocity. For this case, it turned out that the shock velocity was in fact greater which meant that a window would not need to be used since there were no wave interactions. Thus, only the free surface velocity needed to be measured. The probes used for the oblique wedge target in this experiment were the same ones described for the y-cut quartz validation experiments. Bare fiber probes were used for the PMMA sample.

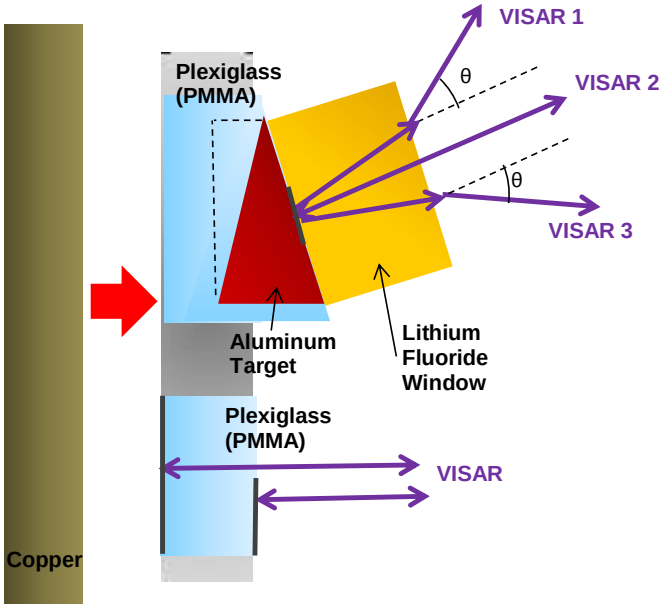

Figure 6.7: Oblique wedge and PMMA sample configuration schematic.

6.3.3 Results and Discussion

Table 6.1 shows the calculated results of the two main experiments and Figures 6.8 and 6.9 show the particle velocity profiles. In Table 6.1, "vpf Normal" refers to the velocity per fringe constant used for the central probe on the oblique wedge target, "vpf Left" and "vpf Right" are for the two off center probes, and "vpf PMMA" front and rear are for the PMMA sample. Note that for experiment 2, the normal probe had a dual-delay system and hence had two different values. The angles θ Normal, Left and Right are the measured angles for the normal, left and right probes. The incident shock velocity corresponds to the shock velocity in the PMMA sample which in turn allows for the shock arrival time to be solved for at the front of the aluminum wedge target – given by "shock arrival target front" — by using the thickness of the PMMA sleeve and the PMMA wedge, taken halfway up the wedge specimen. The thickness of the PMMA wedge is also measured midway up, where the bottom thickness of the triangular wedge was divided in half to find the thickness in the middle. C_L and C_S refer to the longitudinal and shear wave velocities in the target, respectively.

Here it should be noted that finding the shock arrival time at the front of the aluminum wedge is not only crucial to determining wave velocity, but it is also rather tricky. For experiment 1, the arrival time was found to be 8.3468e-7 sec, based on the incident shock velocity of 4.1567 km/s and the combined PMMA wedge and sleeve thickness of 2.4695 mm. However, this is assuming that the impact at the front of the oblique wedge target at the driver front surface occurred at time zero, which it did not. In reality, the time of impact at the center of the target holder was at 61.5 ns. The average amount that the aluminum wedge was offset from the target holder was by -0.004 mm which means that the corrected time of incident shock wave arrival at the front of the aluminum wedge was 8.3468e-7 sec + 61.5 ns + 0.004 mm/1.0206 km/s = 9.0010e-7 sec, where the last term is just the aluminum offset divided by the impactor velocity. The same approach was repeated to find the arrival time in the second experiment. Looking at the calculation in Table 6.1, it appears that the measured incident shock wave velocity is very close to the simulation, however, the longitudinal and shear wave speeds are quite a bit off. The variation in the shear wave velocity between the two experiments could be due to the difficulty in determining when this wave arrives since its onset is gradual, unlike the shock wave.

As can be seen in Figures 6.8 and 6.9, the velocity profiles match very well to the simulation indicating that the techniques used to measure the velocity profiles are accurate. It is interesting to point out that at the beginning of both of the transverse velocity profiles, there are what look like dips in the data. Originally, these were sudden jumps in between two data points that were

	Experiment 1	**Experiment 2**	**Simulation**
Window Thickness (mm)	12.9328	12.9346	12.0
Window Diameter (mm)	25.4747	25.4337	25.0
Window Density $\left(g/cm^3\right)$	2.6338	2.6295	2.638
PMMA Sample Thickness (mm)	1.9050	2.2657	N/A
PMMA Sample Diameter (mm)	29.9390	50.9270	N/A
PMMA Sample Density $\left(g/cm^3\right)$	1.1819	1.1760	N/A
PMMA Sleeve Thickness (mm)	1.1220	1.1164	2
PMMA Wedge Thickness (mm)	2.2495	2.2913	2.293
Target Density $\left(g/cm^3\right)$	2.7228	2.7447	2.703
Target Rear Angle (deg)	5.0239	5.1979	5.3286
Target Thickness (mm)	3.5199	3.5351	3.504
Impactor Thickness (mm)	7.9207	12.6944	8.0
Impactor Diameter (mm)	87.4268	87.4928	34
Impactor Density $\left(g/cm^3\right)$	8.3808	8.1681	8.930
Impactor Velocity (km/s)	1.0206	1.0335	1.0
Target Tilt ($mrad$)	1.52	2.73	N/A
vpf Normal Probe ($m/s/f$)	223.1	125.35, 291.95	N/A
vpf Left Probe ($m/s/f$)	223.1	61.5	N/A
vpf Right Probe ($m/s/f$)	223.1	70.69	N/A
vpf PMMA Front ($m/s/f$)	58.66	125.35	N/A
vpf PMMA Back ($m/s/f$)	58.66	291.95	N/A
θ Normal (deg)	0.9023	0.8980	N/A
θ Left (deg)	19.7433	20.2120	N/A
θ Right (deg)	19.7194	20.6960	N/A
Incident Shock Velocity (km/s)	4.1567	4.0044	4.0121
Shock Arrival Target Front (sec)	9.0010e-7	9.6009e-7	1.07e-7
Shock Arrival Target Rear (sec)	1.725e-6	1.741e-6	1.663e-6
Shear Arrival Target Rear (sec)	2.138e-6	2.064e-6	2.049e-6
C_L (km/s)	4.2671	4.5267	5.9089
C_S (km/s)	2.8434	1.7831	3.5792

Table 6.1: Experiment parameters, calculations and results for oblique wedge experiments. "vpf Normal" refers to the velocity per fringe constant used for the center probe on the oblique wedge target, "vpf Left" and "vpf Right" are for the two off center probes, and "vpf PMMA" front and rear are for the PMMA sample. θ Normal, Left and Right are the measured angles for the normal, left and right probes. "Incident shock velocity" corresponds to the shock velocity in the PMMA sample. "Shock arrival target front" is the arrival time of the shock at the front of the aluminum target, while "shock arrival target rear is the arrival of the shock at the rear surface of the aluminum". "Shear arrival target rear" is the time the shear wave arrives at the rear surface of the aluminum target. C_L and C_S refer to the longitudinal and shear wave velocities in the target, respectively.

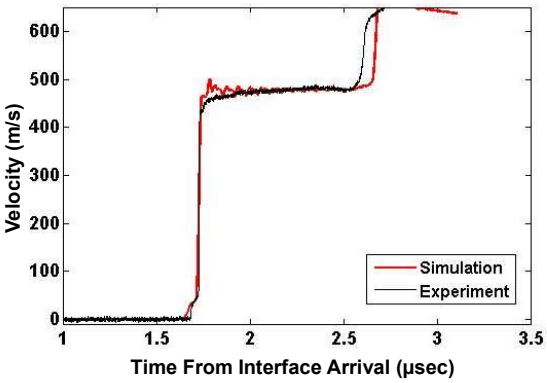

(a) a) Longitudinal Particle Velocity.

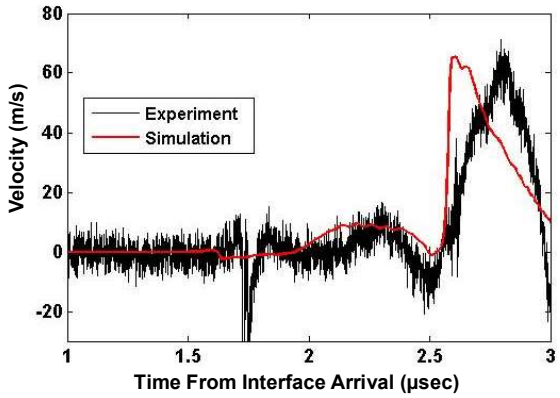

(b) b) Transverse Particle Velocity.

Figure 6.8: Longitudinal and transverse particle velocities for experiment 1 measured at the aluminum-lithium fluoride interface. Experimental data shifted such that shock wave arrival at the interface in the experiment coincides with timing of the simulation.

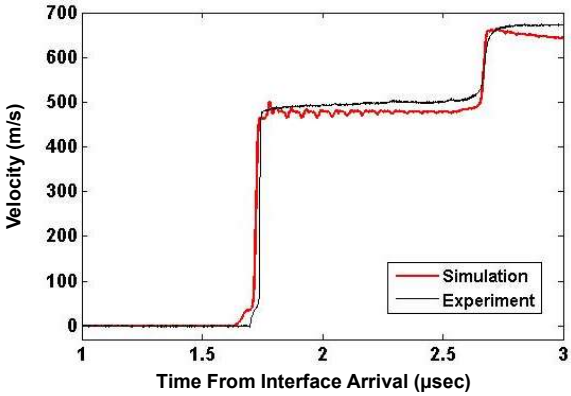

(a) a) Longitudinal Particle Velocity.

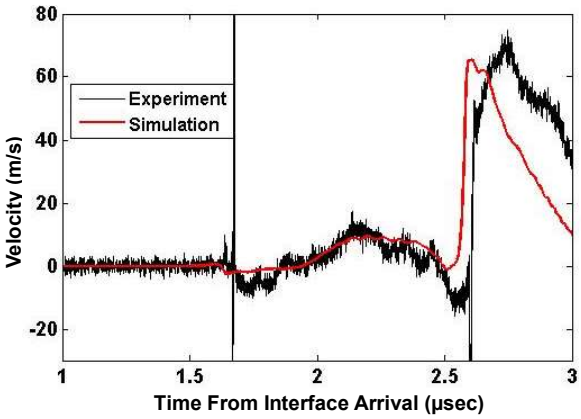

(b) b) Transverse Particle Velocity.

Figure 6.9: Longitudinal and Transverse particle velocities for experiment 2 measured at the aluminum-lithium fluoride interface. Experimental data shifted such that shock wave arrival at the interface in the experiment coincides with timing of the simulation.

corrected for. There could be several reasons why these could have occurred. For one, there could be a slight difference in the left and right probes during the elastic foot portion of the profiles which could be from a slower rise in one curve due to a VISAR delay or slower detectors. Another reason could be that one probe has more fringes than the other (i.e. 9 for the left and 7 for the right for the second experiment). Thus, a small error in the vpf could lead to a large error in the velocity especially where the shock wave arrives prior to shear arrival. This would affect the calculated shear wave velocity since the two side probes measure components from the longitudinal velocity as well. These issues indicate how sensitive the result is to any variations from the two probes and illustrates how difficult the setup of this experiment is. Nonetheless, since it does not make sense that data would jump suddenly from one point to the next in the shear wave, it was corrected for to find the underlying gradually ascending velocity curve.

Despite the blip at the beginning of the shear wave, the profiles still match exceptionally well and would continue to improve as the experiment became more routine rather than an exploration of a new diagnostic. Since the particle velocities match, the discrepancies in the wave velocities could be issues with timing or target measurements. For instance, if the thicknesses of the wedged samples were measured even slightly off, this could alter the apparent velocity of the two waves. As an example, if the measured longitudinal wavespeed in the first experiment was actually 5.9089 km/s, as in the simulation, then the thickness of the aluminum wedge should have been 4.87 mm as opposed to the 3.5199 mm measured value. This is only a difference of 1.3501 mm and could have resulted from estimating the thickness of the target halfway up to be half of the base measurement. Furthermore, since the front of the oblique wedge target was not completely planar, as indicated by the offset from the target holder, it is difficult to accurately say when the time of impact occurred at the center of the target and hence calculating shock wave arrival at the front of the aluminum target becomes difficult. Despite these concerns, this experiment shows that an oblique wedge configuration can be used to transmit and measure the transverse particle velocity from a shear wave. Specifically, experiment 2, where the probe holder assembly was switched to a single bar in which holes were drilled for specific angles, matches quite well with the simulation. The reason this approach could have worked better is that the probes were less likely to move when forced to stay in a drilled angled hole rather than in a ball-and-socket type joint that could move. Furthermore, the vpfs used were much smaller than in experiment 1, which would have allowed for more velocity resolution at the lower velocity range for the transverse measurement. In future experiments, if the windowed approach is used and hence the wavespeeds need to be used to find the longitudinal and

shear stresses, careful measurement techniques should be implemented on the PMMA and aluminum wedges. Timing issues also need to be resolved – perhaps there were some discrepancies between what time zero was thought to be and when it really occurred with respect to the center of the target. Finally, as mentioned in Section 3.6.11, using an anvil backing could potentially eliminate the need to know the shear and shock wave velocities in the wedge since the elastic velocities in the anvil backing material would be known, the elastic shear wavespeed in the wedge target could be used as an estimate, and the shock wave velocity in the wedge could be found using shock polar analysis.

Chapter 7

Summary and Future Work

7.1 Summary

The focus of this dissertation has been to study material response to shear at high pressures and strain-rates. In order to do this, two novel configurations were introduced that implement transverse waves to study the shear response and strength of materials. The first experimental setup was the oblique wedge configuration, which implements an angled target to generate shear waves. Upon impact, a shock wave is generated in the driver material which is reflected and transmitted at the driver-target interface. Due to the angle of obliquity with respect to the target, a shock is transmitted into the specimen followed by a shear wave. The second configuration was the y-cut quartz sandwich experiment, which uses the anisotropic properties of y-cut quartz for shear generation. Two waves are generated upon impact that both contain longitudinal and shear components of velocity. As these waves propagate into the other materials in the target, a pressure and shear wave is generated for each wave and the sample of interest is subjected to shear. Both configurations are novel in their approach in using a normal impact experiment in testing shear response.

To understand what occurs in these experiments, wave propagation through solids was discussed in Chapter 2. The conservation equations of mass and momentum were introduced in order to derive expressions for the jumps in velocities and tractions across an oblique elastic plane wave incident on an interface. This example was simplified to the one dimensional case of a plane wave travelling parallel to an interface, at which point the hydrostatic, one dimensional stress and one dimensional strain assumptions were discussed in order to introduce the concept of material strength. Material response past the yielding point was discussed as well to show that, as velocity increases with increasing pressure, a shock wave will form. Using the conservation of mass, momentum and energy, the Rankine-Hugoniot jump conditions that govern the properties across a shock wave were

then introduced. Using these jump conditions and a linear relationship between the shock velocity, U_S, and the particle velocity, u_p, the state across an oblique shock wave incident on an interface was analyzed using shock polar analysis. This technique allowed for the determination of the transmitted shock wave angle in the oblique wedge configuration, a property necessary for the design of the target.

Using shock polar analysis, a variety of parameters in the oblique wedge design were considered in Chapter 3. The longitudinal stress in the wedged target was found and analyzed in relation to the angle of obliquity of the incident wave in the driver material of the oblique wedge experiment. The transmitted shear wave angle in the target was then studied with respect to the transmitted shock wave angle as well as the angle of obliquity. It was found that the impact velocity, driver material, and angle of obliquity could be controlled depending on the longitudinal stress and shear response desired in the target. Numerical simulations were then performed using CTH hydrocode to determine the shear response a particular target would exhibit. From these simulations it was found that, while all of the targets yielded, not all of them were in a state of pure shear, which is needed to determine the strength of a material. The cause of yielding was further elucidated by using a stress path analysis on the yield surface of each configuration. It was found that certain configurations can in fact measure strength. The oblique wedge design has limitations, which can be mitigated by implementing an anvil in place of a window at the rear surface of the target in order to measure in-situ velocities. Overall, it was found that this design is promising in finding the strength of materials.

The next technique proposed was the y-cut quartz sandwich configuration in Chapter 4. This design combines the oblique gun setup of experiments with the implementation of y-cut quartz for shear generation from previous works. Simulations were performed using the Laslo code on two designs. The first setup used y-cut quartz and a tungsten carbide driver followed by a thin sample and a tungsten carbide backing plate, while the second eliminated the tungsten carbide driver. By using plates surrounding a thin sample, the sample could remain in a state of pure shear at a high strain-rate, much like the oblique gun experiments previously performed. Both configurations were designed such that shear response could be found prior to the arrival of edge waves at the rear surface of the composite target and while the sample was still in compression. Performing a stress path analysis against the yield surface, it was found that both designs can be used to test the strength of materials.

To perform these two types of experiments, loading systems must be implemented. These were discussed in Chapter 5. An overview of the single stage powder guns at Caltech and Sandia National

Laboratories was given, along with a description of the intermediate velocity gas gun at Sandia. The methods used to measure impact velocity and tilt were also discussed. Laser interferometry was then introduced as a means by which to measure particle velocities at the rear surface of each target. The Velocity Interferometer System for any Reflector (VISAR), which allows for a diffuse surface to be monitored at 1-2% accuracies, was described along with the configurations of monitoring probes required to measure transverse velocities both through a window and at a sample surface. This technique implements the Doppler shift in frequency of light reflected off of a moving target to measure the velocity. The other particle velocity measurement technique mentioned was Photon Doppler Velocimetry (PDV), which also uses the Doppler shift to find velocity.

Two types of experiments were performed in the course of this investigation. The first was the y-cut quartz validation experiment, which tested the ability of a three-probe configuration to measure shear velocities. Using the known response of y-cut-quartz, the experiment was conducted using a window to measure the in-situ longitudinal and shear velocities using three probes and VISAR systems. An aluminum spot was diffused onto the lithium fluoride window to scatter incoming laser light such that it could be collected at the three probes. It was found that the measured velocities matched well with the simulation for this setup. Since this method was proven to work on a well-known material, it was used to measure the velocities in the oblique wedge configuration. A copper impactor was propelled at 1000m/s into a composite target consisting of a polymethylmethacrylate (PMMA) driver, an aluminum 6061-t6 target and a lithium fluoride window. A second PMMA target was secured into the same target holder such that the shock velocity of the incident wave in the driver could be found in order to calculate the shock arrival time at the front of the aluminum target in the oblique wedge configuration. The results showed that the particle velocities at the aluminum-lithium fluoride interface matched quite well with the simulations, which indicates that this experiment can be used to study the shear response of a variety of materials.

7.2 Future Work

Though it has been shown that the oblique wedge configuration with a window can be used to study the shear response of an aluminum target, for the purposes of studying a wide range of materials, an anvil can be used instead. Section 3.6.11 outlines the elastic wave analysis that can be used on the rear surface velocities measured in such an experiment to find the in-situ velocities in the target. These can then be used to calculate the shear stress in the material and, for some configurations, the strength as well. Once these experiments would be performed, they could be

compared to simulations in CTH to see if the current models reflect the material strength exhibited for a range of pressures and strain-rates the targets were tested at. Higher impact velocities could also be used to extend the experiments to higher strain-rates.

For the y-cut quartz sandwich configuration, the theoretical background was described and a model to design the targets was proposed. It appears that, in theory, both the one driver and two driver setups would work. Nevertheless, these experiments could be performed as well to validate the theory. A schematic for the y-cut quartz sandwich configuration experiment is shown in Figure 7.1a. Upon impact, y-cut quartz generates two waves, which both have longitudinal and transverse components of velocity. The latter component causes the sample to be subjected to shear. Using a high strength backing material that remains elastic, the shear stress at the sample-backing interface can be found. The two driver and one driver configurations for this setup are shown in 7.1b and 7.1c. Shorting pins can be used to measure the tilt of the target, with two probes in conjunction with a PDV to measure the longitudinal and shear rear surface velocities. The PDV is described in detail in Section 5.2.2, but it has the ability to measure low velocities and hence could be implemented for this configuration.

To actually obtain the transverse measurements off the rear surface of the tungsten carbide, the surface would have to be diffused. It is quite difficult to polish and roughen this surface due to the hardness of the material, but preliminary tests have been conducted in which light was scattered to the angled probe. In these experiments, an Electrical Discharge Machine (EDM) was used to cut the WC, which was polished using 400 grit sandpaper. A focusing probe normal to the WC was implemented and light was collected both at this probe and a collimating probe placed at an angle from the normal. In an experiment, these probes could be used in conjunction with an isolator for the collimating probe such that it does not shine light onto the target, but only collects the diffracted light from the central probe. The probes here were aligned using a patch cord that allowed a green light laser to be connected to the fiber optic probes intended for 1550 nm light in a manner similar to the alignment process used for the y-cut quartz validation and oblique wedge experiments discussed in Section 6.2.2.

In order for shear to be transmitted throughout the entirety of the target, it is proposed that the quartz and tungsten carbide be polished, as it has been shown to produce better shear transmission. It is thought that if a surface is too rough, it may produce a rubble like layer that can act much like ball bearings and cause the material to slip. In past experiments using y-cut quartz as a shear generator [18], epoxy was mixed with diamond particles and deposited in between the quartz and the

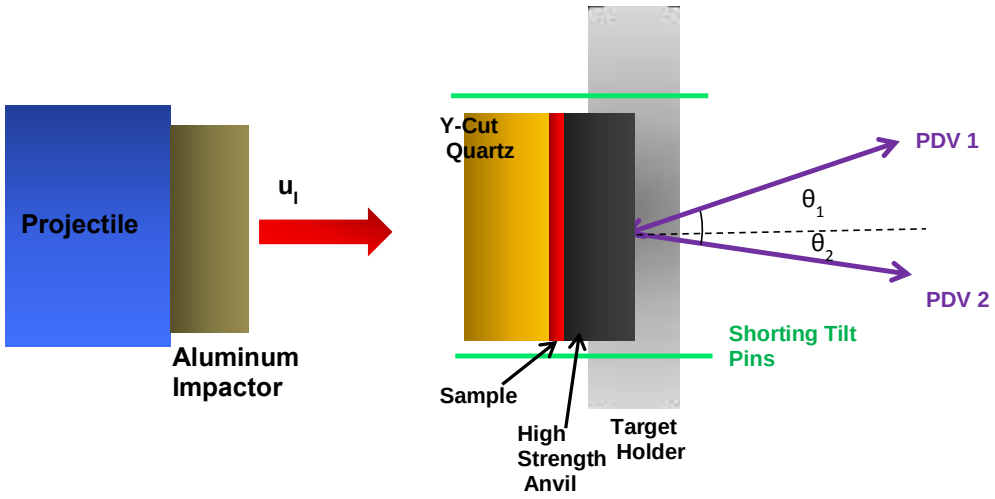

(a) Y-cut quartz sandwich configuration experiment schematic.

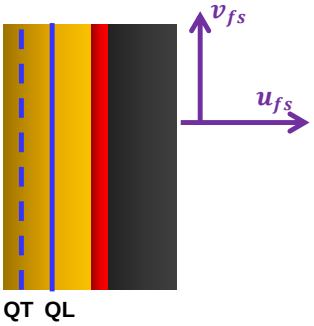

(b) Wave state in one driver target.

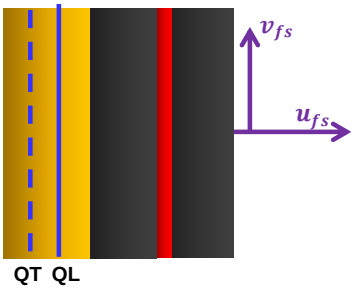

(c) Wave state in two driver target.

Figure 7.1: Schematic for the y-cut quartz sandwich configuration experiment. Upon impact, y-cut quartz generates two waves, which both have longitudinal and transverse components of velocity. The latter component causes the sample to be subjected to shear. Using a high strength backing material that remains elastic, the shear stress at the sample-backing interface can be found. Shorting pin are used to measure the tilt of the target and two probes are used in conjunction with a PDV to measure the longitudinal and shear rear surface velocities. The two configurations for this setup are shown in 7.1b and 7.1c

target. This mixture seemed to only transmit shear up to a certain point and thus it is proposed that epoxy be deposited on the outer edges of each interface in the y-cut quartz sandwich configuration instead such that the compression of the longitudinal wave allows for shear transmission, rather than the epoxy. These experiments could be performed and compared to the simulations shown in this study. More complex strength models could be used as well to compare the measured strength to that given by the model. The final suggestion for the direction this work could take would be to extend the experiments to higher strain-rates by using a thinner sample.

References

[1] A.S. Abou-Sayed and R.J. Clifton. Pressure Waves in Fused Silica. *Journal of Applied Physics*, 47(5):1762–1770, 1976.

[2] A.S. Abou-Sayed, R.J. Clifton, and L. Hermann. The Oblique-Plate Impact Experiment. *Experimental Mechanics*, 16(4):127–132, 1976.

[3] C.S. Alexander, J.R. Asay, and T.A. Hall. Magnetically Applied Pressure-Shear: A New Method for Direct Measurement of Strength at High Pressure. *Journal of Applied Physics*, 108(12):126101–126103, 2010.

[4] M. Altenaiji, G.K. Schleyer, and Y.Y. Zhao. Ch. 19: Characterisation of Aluminum Matrix Syntactic Foams Under Static and Dynamic Loading. In *Composites and their Properties*. 2012.

[5] T. Ao and D.H. Dolan. SIRHEN: A Data Reduction Program for Photonic Doppler Velocimetry Measurements. Technical Report SAND2010-3628, Sandia National Laboratories, 2010.

[6] J.R. Asay. The Sandia National Laboratories Shock Thermodynamics Applied Research (STAR) Facility. Technical Report SAND81-1901, Sandia National Laboratories, 1981.

[7] L.M. Barker. VISAR vs. PDV. Technical report, Valyn International.

[8] L.M. Barker and R.E. Hollenbach. Shock-Wave Studies of PMMA, Fused Silica, and Sapphire. *Journal of Applied Physics*, 41(10):4208–4226, 1970.

[9] L.M. Barker and R.E. Hollenbach. Laser Interferometer for Measuring High Velocities of Any Reflecting Surface. *Journal of Applied Physics*, 43:4669–4675, 1972.

[10] L.M. Barker and K.W. Schuler. Correction to the Velocity-Per-Fringe Relationship for the VISAR Interferometer. *Journal of Applied Physics*, 45(8):3692–3693, 1974.

[11] D.J. Benson. Computational Methods in Lagrangian and Eulerian Hydrocodes. *Computational Methods in Applied Mechanics and Engineering*, 99(2-3):235–394, 1992.

[12] A.F. Bower. *Applied Mechanics of Solids*, chapter 3.2. CRC Press, 2009.

[13] J.L. Brown. *High Pressure Hugoniot Measurements in Solids Using Mach Reflections*. PhD thesis, Caltech University, 2011.

[14] J.L Brown, G. Ravichandran, and W.D. Reinhart. High Pressure Hugoniot Measurements Using Converging Shocks. *Journal of Applied Physics*, 109(9):093520–093530, 2011.

[15] E.J. Caramana, M.J. Shashkov, and P.P. Whalen. Formulations of Artificial Viscosity for Multi-Dimensional Shock Wave Computations. *Journal of Computational Physics*, 144:70–97, 1998.

[16] L.C. Chhabildas and M.E. Kipp. Pressure-Shear Loading of PBX-9404. In *Proceedings of the Eighth Symposium (International) on Detonation*. 1985.

[17] L.C. Chhabildas, H.J. Sutherland, and J.R. Asay. A Velocity Interferometer Technique to Determine Shear-Wave Particle Velocity in Shock-Loaded Solids. *Journal of Applied Physics*, 50(8):5196–5201, 1979.

[18] L.C. Chhabildas and J.W. Swegle. Dynamic Pressure-Shear Loading of Materials Using Anisotropic Crystals. *Journal of Applied Physics*, 51(9):4799–4807, 1980.

[19] L.C. Chhabildas and J.W. Swegle. On the Dynamical Response of Particulate-Loaded Materials. I. Pressure-Shear Loading of Alumina Particles in an Epoxy Matrix. *Journal of Applied Physics*, 53(2):954–956, 1982.

[20] R.J. Clifton. Analysis of Laser Velocity Interferometer. *Journal of Applied Physics*, 41(13):5335–5337, 1970.

[21] R.J. Clifton. Pressure-Shear Impact and Dynamic Plastic Response of Metals. In *Shock Waves in Condensed Matter 1983: Proceedings of the American Physical Society Topical Conference Held in Santa Fe, New Mexico, July 19-21, 1983*. Elsevier Science-Publishers B.V., 1984.

[22] R.J. Clifton. Linear Elastic Waves Notes. Unpublished, 2013.

[23] CoorsTek. Durable Tungsten Carbide for Extreme Service Applications, 2006.

[24] L. Davison. *Fundamentals of Shock Wave Propagation in Solids . Shock Wave and High Pressure*. Springer-Verlag, 2008.

[25] L. Davison and R.A. Graham. Shock Compression of Solids. *Physics Reports*, 55(4):255–379, 1979.

[26] T. de Rességuier, P. Berterretche, and M. Hallouin. Evidence of Anisotropic Wave Propagation in Laser Shock-Loaded Quartz. In *2005: Proceedings of the Conference of the American Physical Society Topical Group on Shock Compression of Condensed Matter. AIP Conference Proceedings*, volume 845, pages 611–614. 2006.

[27] M. Dietenberger, M. Buyuk, and C. Kan. Development of a High Strain-Rate Dependent Vehicle Model. Technical report, DYNAmore, 2010.

[28] D. Dolan. Foundations of VISAR Analysis. Technical Report SAND2006-1950, Sandia National Laboratories, 2006.

[29] D. Dolan. Window Corrections for Off Axis Velocimetry Measurements. Sandia National Laboratories, 2008.

[30] K.E. Duprey and R.J. Clifton. Pressue-Shear Response of Thin Tantalum Foils. *AIP Conference Proceedings*, 505:447–450, 2000.

[31] H.D. Espinosa. Dynamic Compression-Shear Loading with in-Material Interferometric Measurements. *Review of Scientific Instruments*, 67(11):3931–3939, 1996.

[32] H.D. Espinosa, M. Mello, and Y. Xu. A Variable Sensitivity Displacement Interferometer with Application to Wave Propagation Experiments. *Journal of Applied Mechanics*, 64:123–131, 1997.

[33] J.E. Field, S.M. Walley, W.G. Proud, H.T. Goldrein, and C.R. Siviour. Review of Experimental Techniques for High Rate Deformation and Shock Studies. *International Journal of Impact Engineering*, 30:725–775, 2004.

[34] J. N. Florando, T. Jiao, S. E. Grunschel, R. J. Clifton, D. H. Lassila, L. Ferranti, R. C. Becker, R. W. Minich, and G. Bazan. High Rate Plasticity Under Pressure Using Windowed Pressure Shear Impact Experiment. *AIP Conference Proceedinsg*, 1195:723–726, 2009.

[35] G.R. Fowles. Shock Wave Compression of Hardened and Annealed 2024 Aluminum. *Journal of Applied Physics*, 32(8):1475–1487, 1961.

[36] R. Fowles. Dynamic Compression of Quartz. *Journal of Geophysical Research*, 72(22):57295742, 1967.

[37] R.J. Frutschy, K.J.and Clifton. High-Temperature Pressure-Shear Plate Impact Experiments Using Pure Tungsten Carbide Impactors. *Experimental Mechanics*, 38(2):116–125, 1998.

[38] S.R. Goldman, C.W. Barnes, S.E. Caldwell, D.C. Wilson, S.H. Bartha, J.W. Grove, M.L. Gittings, W.W. Hsing, R.J. Kares, K.A. Klare, G.A. Kyrala, R.W. Margevicius, R.P. Weaver, M.D. Wilke, A.M. Dunne, M.J. Edwards, P. Graham, and B.R. Thomas. 10. Production of Enhanced Pressure Regions Due to Inhomogeneities in Inertial Confinement Fusion Targets. *Physics of Plasmas*, 7(5):2007–2013, 1999.

[39] V.T. Golovchan. Elastic Moduli of a Tungsten Monocarbide Crystal. *International Applied Mechanics*, 34(8):755–757, 1998.

[40] D.E. Grady. Analysis of Shock and High-Rate Data for Ceramics: Equation of State Properties and Fragmentation in Ballistic Environment. Technical report, Applied Research Associates, Inc., 2009.

[41] K. Graff. *Wave Motion in Elastic Solids*. Courier Dover Publications, 1975.

[42] S.E. Grunschel. *Pressure-Shear Plate Impact Experiments on High-Purity Aluminum at Temperatures Approaching Melt*. PhD thesis, Brown University, 2009.

[43] Y.M. Gupta. Shear Measurements in Shock-Loaded Solids. *Applied Physics Letters*, 29(11):694–697, 1976.

[44] A.M.S. Hamouda. *High Strain-Rate Constitutive Equation for Metallic Materials*. PhD thesis, Dublin City University, 1991.

[45] W. Hemsing. Velocity Sensing Interferometer (VISAR) Modification. *Review of Scientific Instruments*, 50(1):73–78, 1979.

[46] E. S. Hertel Jr., R. L. Bell, M. G. Elrick, A. V. Farnsworth, G. I. Kerley, J. M. McGlaun, S. V. Petney, S. A. Silling, P. A. Taylor, and L. Yarrington. CTH: A Software Family for Multi-Dimensional Shock Physics Analysis. In *Shock Waves @ Marseille I, Part 4*, pages 377–382. 1995.

[47] J.N. Johnson. Shock Propagation Produced by Planar Impact in Linearly Elastic Anisotropic Media. *Journal of Applied Physics*, 42(13):55225560, 1971.

[48] J.N. Johnson. Calculation of Plane-Wave Propagation in Anisotropic Elastic-Plastic Solids. *Journal of Applied Physics*, 43(5):20742082, 1972.

[49] J.N. Johnson and R. Cheret. Shock Waves in Solids: an Evolutionary Perpective. *Shock Waves*, 9(3):193–200, 1999.

[50] G.I. Kerley. The Linear Us-up Relation in Shock-Wave Physics. Technical report, Kerley Technical Services, 2006.

[51] G.I. Kerley. Calculation of Release Adiabats and Shock Impedance Matching. Technical report, Kerley Technical Services, 2008.

[52] K. Kim, R.J. Clifton, and P. Kumar. A Combined Normal- and Ttranserve-Displacement Interferometer with an Application to Impact of Y-Cut Quartz. *Journal of Applied Physics*, 487(10):4132–4139, 1977.

[53] R.J. Kim, K.S.and Clifton. Pressure-Shear Impact of 6061-T6 Aluminum. *Journal of Applied Mechanics*, 47(1):11–16, 1980.

[54] M.E. Kipp, L.C. Chhabildas, W.D. Reinhart, and M.K. Wong. Polyurethane Foam Impact Experiments and Simulations. *AIP Conference Proceedings*, 505:313–316, 2000.

[55] B.J. Kohn. Compilation of Hugoniot Equations of State. Technical Report AFWL-TR-69-38, Air Force Weapons Laboratory, 1969.

[56] C.H. Konrad and R.L. Moody. Rear Surface Pin Triggering Technique. Technical Report SAND86-0791, Sandia National Laboratories, 1986.

[57] W.M. Lai, D. Rubin, and E. Krempl. *Introduction to Continuum Mechanics, 4th Edition.* Elsevier Ltd., 2010.

[58] C.H. Li. *A Pressure-Shear Experiment for Studying the Dynamic Plastic Response of Materials at Shear Strain Rates of* $10^5/s$. PhD thesis, Brown University, 1982.

[59] K.D. Litasov, A. Shatskiy, Y. Fei, A. Suzuki, E. Ohtani, and K. Funakoshi. Pressure-Volume-Temperature Equation of State of Tungsten Carbide to 32GPa and 1673 Kelvin. *Journal of Applied Physics*, 108(5):053513–053519, 0210.

[60] S.P. Marsh. *LASL Shock Hugoniot Data.* University of California Press, 1980.

[61] M. Mello. Interferometry: Ae104 Experimental Methods Supplemental Lecture Notes. Caltech, 2008.

[62] H.W. Meyer Jr. and D.S. Kleponis. An Analysis of Parameters for a Johnson-Cook Strength Model for a 2-in-Thick Rolled Homogeneous Armor. Technical report, Weapons and Materials Research Directorate, ARL, 2001.

[63] M.A. Meyers. *Dynamic Behavior of Materials*. John Wiley and Sons, Inc., 1994.

[64] T. Neal. Second Hugoniot Relationship for Solids. *Journal of Physical Chemistry of Solids*, 38:225–231, 1977.

[65] K.T. Ramesh. High Strain Rate Impact Experiments. In *Springer handbook of experimental solid mechanics.*, pages 929–960. Springer US, 2008.

[66] M. Rauls. Photonic Doppler Velocimeter (PDV) User Guide. Caltech, 2013.

[67] G. Ravichandran. Plasticity Notes. Unpublished, 2010.

[68] G. Ravichandran. Shock Notes. Unpublished, 2010.

[69] M.H. Rice, R.G. McQueen, and J.M. Walsh. Compression of Solids by Strong Shock Waves. In *Solid State Physics, Volume 6*, pages 1–63. Academic Press Inc (London) LTD, 1958.

[70] J. Robbins. Laslo Code. Sandia National Laboratories, 2013.

[71] M.D. Salas. The Curious Events Leading to the Theory of Shock Waves. *Shock Waves*, 16(6):477–487, 2007.

[72] S. Sarva, A.D. Mulliken, and M.C. Boyce. Mechanics of Taylor Impact Testing of Polycarbonate. *International Journal of Solids and Structures*, 44(7-8):2381–2400, 2007.

[73] D.J. Steinberg. Equation of State and Strength Properties of Selected Materials. Technical Report UCRL-MA-106439, Lawrence Livermore National Laboratory, 1996.

[74] O.T. Strand, D.R. Goosman, C. Martinez, T.L. Whitworth, and W.W. Kuhlow. Compact System for High-Speed Velocimetry Using Heterodyne Techniques. *Review of Scientific Instruments*, 77:083108–083115, 2006.

[75] J.W. Swegle and L.C. Chhabildas. A Technique for the Generation of Pressure-Shear Loading Using Anisotropic Crystals. In *Shock waves and high-strain-rate phenomena in metals*. Springer US, 1981.

[76] W. Tong and R.J. Clifton. Pressure-Shear Impact Investigation of Strain Rate History Effects in Oxygen-Free High-Conductivity Copper. *Journal of Mechanics and Physics of Solids*, 40(6):1251–1294, 1992.

[77] J. Wackerle. Shock-Wave Compression of Quartz. *Journal of Applied Physics*, 33(3):922–937, 1962.

[78] S. Zhuang. *Shock Wave Propagation in Periodically Layered Composites*. PhD thesis, Caltech University, 2002.